Università degli Studi di Padova
Dipartimento di Fisica ed Astronomia "G. Galilei"
Tesi di Laurea Magistrale in Physics

Control of the emission properties of quantum emitters by coupling with phase-change nanomaterials

Laureando:
Alessandro Lovo

Relatore:
Prof. Tiziana Cesca
Correlatore:
Prof. Giovanni Mattei

Anno Accademico 2020/2021

Abstract

In this work, the effect of the coupling between a thin film of the phase changing material vanadium dioxide (VO_2) and a layer of Er^{3+} quantum emitters embedded in a silica matrix is investigated. Several characterization techniques of the VO_2 thin films are carried out, revealing a direct correlation between the crystallite grain size and the width of the hysteresis loops. After a synthesis recipe by magnetron sputtering co-deposition and subsequent annealing which yields the finest grains is found, it is then used to fabricate samples with both a VO_2 thin film and an Er:SiO_2 emitting layer. Subsequently, the effects of the Metal-Insulator Transition of VO_2 on the emission properties of the Er^{3+} ions are studied both experimentally and with the use of numerical simulations, showing an amplification of the radiative lifetime of the emitters by a factor of 7 for the insulating phase of VO_2 and 14 for the metallic one and allowing the measurement of a full and detailed hysteresis cycle of the photoluminescent emission of the Er^{3+} ions.

Contents

Chapter 1

Introduction

With the advent of quantum communications and photonics, the demand for single photon sources has risen, sparking a plethora of different approaches [1]. Among them, the use of Er^{3+} ions is of particular interest as, owing to the ${}^4I_{13/2} \rightarrow {}^4I_{15/2}$ photoluminescent transition (fig. 1.1 left), they emit photons in the Near Infrared (NIR) at 1540 nm, right in the range of minimum absorption of commercial silica optical fibers (fig. 1.1 right). This means that it would be possible to perform quantum communications using the already present network of optical fibers, simply changing the devices at the receiving and transmitting ends.

However, the characteristic ${}^4I_{13/2} \rightarrow {}^4I_{15/2}$ emission lifetime of Er^{3+} ions is around 10 ms [5], which hinders the possibility of high bit rates. Fortunately, there is a way of reducing the lifetime of these quantum emitters. According to Fermi's golden rule for spontaneous emission, the transition rate between two quantum levels is proportional to the matrix element connecting the two levels and to the Local Density of Optical States (LDOS) [6]. In his pioneering work [7], Purcell discovered that it is possible to manipulate the LDOS and hence the characteristic lifetime of the transition. One of the simplest ways to achieve LDOS engineering is by putting the emitters in close proximity to planar interfaces and the effect was first observed experimentally by Drexhage [8], showing an enhancement of the decay rate as the distance between the emitters and the interface got smaller. The advantage of using planar interfaces is not only the relative simplicity of device fabrication, but also the fact that the modification of the lifetime can be described using the classical model first proposed by Chance, Prock and Silbey (CPS model) [9], where the emitter is assumed to be a dipole oscillator forced by the electromagnetic field reflected by the interface. In the last years many works have been carried out on multilayer geometries [10, 11, 5], showing amplification of the decay rate up to a factor of 20 [12] and in general a very good agreement between the experimental results and the predictions of the CPS model.

The next step in the realization of our desired photonic device is achieving active control on the emission properties of the Er^{3+} ions, in order to control the emission rate on-demand: this is where vanadium dioxide (VO_2) comes into play.

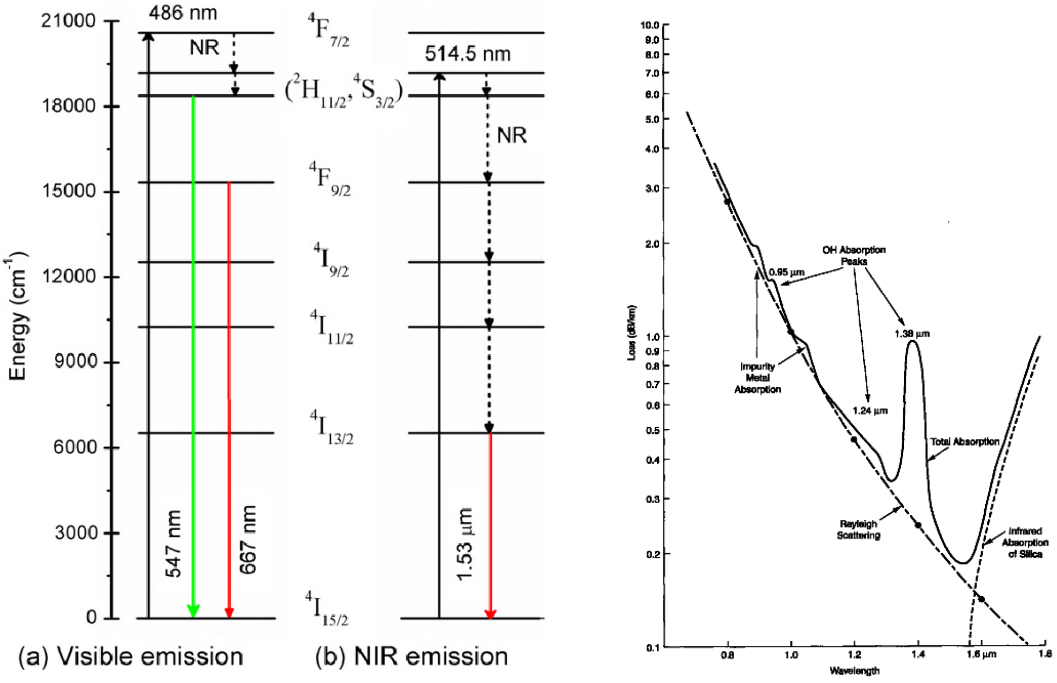

Figure 1.1: (Left): quantum levels of the Er^{3+} ions in a lead borate titanate aluminum fluoride glass matrix and their photoluminescent emissions [2] in the visible range (left) and in the NIR (right). The black dotted arrows represent non-radiative decays. In a silica matrix, the transitions are shifted to slightly higher wavelengths, in particular the ${}^4I_{13/2} \rightarrow {}^4I_{15/2}$ transition is at 1540 nm and the ${}^2H_{11/2} \rightarrow {}^4I_{15/2}$ one is at 522 nm [3]. (Right): absorption spectrum of silica optical fibers [4], which displays a minimum at 1550 nm

VO_2 has three main phases: two insulating ones with a monoclinic structure (M1 and M2) and a metallic rutile one (R), which exhibit different crystalline and electronic structures. As can be seen from the phase diagram in fig. 1.2, when no stress is applied there is a phase transition between the M1 and R configurations at 68 °C (for monocrystalline VO_2), which is fairly close to room temperature. Moreover, it is possible to tune the transition temperature on VO_2 thin films [13] and furthermore the transition can be triggered not only thermally, but also with a mechanical, electrical, magnetical or optical stimulus [14, 15]. This presents many opportunities for the realization of devices ranging from smart windows [16, 17] to actuators [18] to nanostructured electrochemical switches [19]. Recently, VO_2 is also starting to be used in conjunction with quantum emitters like erbium, europium or ytterbium for the fabrication of photonic devices [20, 21]. By exploiting the fact that the dielectric function of VO_2 in the NIR range changes drastically upon the Metal-Insulator Transition (MIT), it is possible to control the properties of the emission, as the decay rate of the emitters will be amplified differently according to the phase of VO_2.

This thesis is aimed at providing a proof of concept of the active control of the room temperature emission properties of Er^{3+} ions in silica, namely using the magnetron sputtering co-deposition technique to realize multilayered samples which successfully feature the coupling between the emitters and a VO_2 thin film. Also, for simplicity, we will work

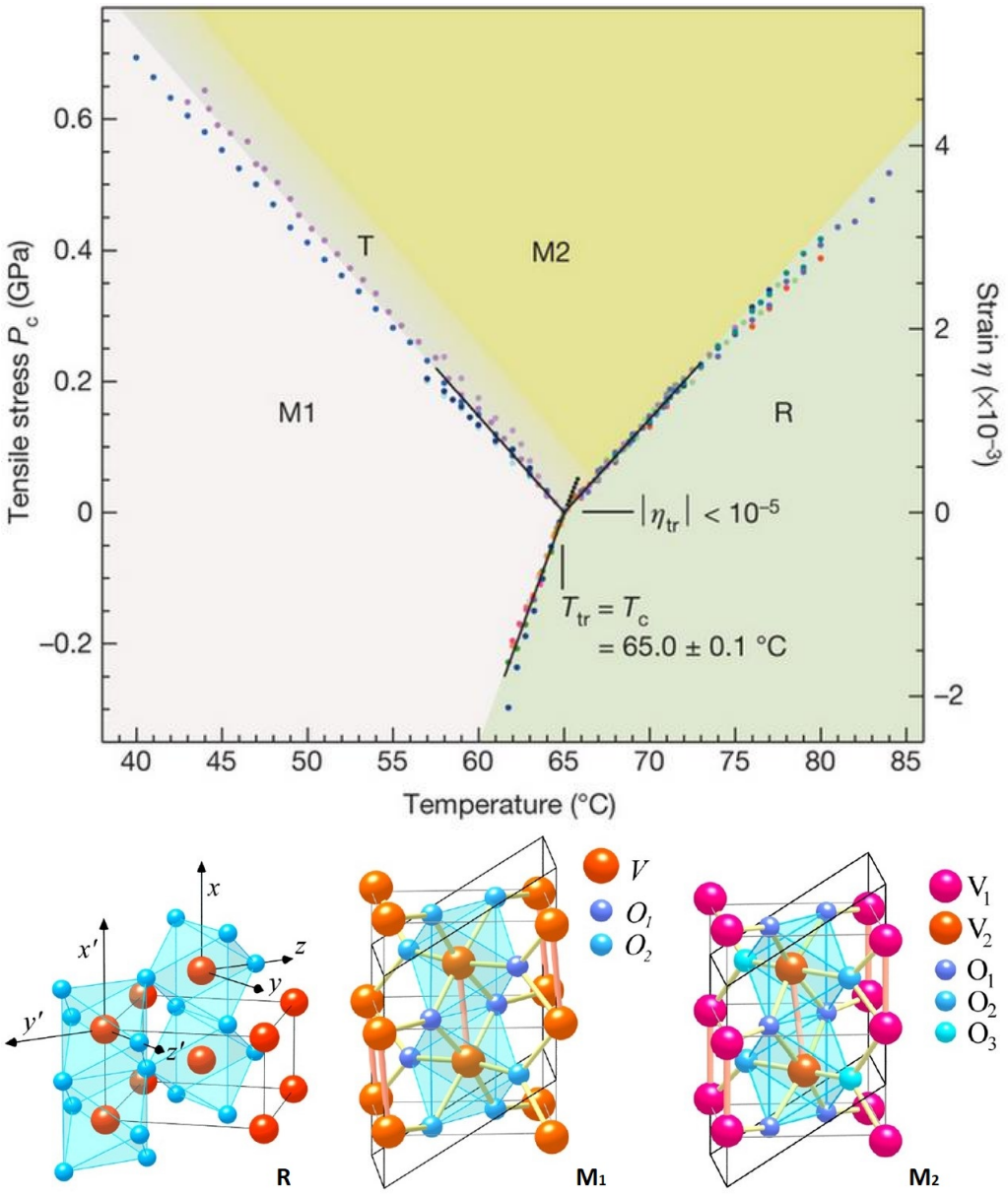

Figure 1.2: (Top): phase diagram of VO_2 [22] with its two monoclinic phases (M1 and M2), the intermediate triclinic phase (T) and the metallic rutile phase (R). (Bottom) Structure of the R, M1 and M2 phases [23].

in the many photons regime and the phase transition of VO_2 will be triggered thermally.

In this work I will start by performing some simulations with the CPS model (chapter 2) in order to plan a proper structure for the samples. Then will follow the description of the several experimental techniques involved in the synthesis and characterization of both VO_2 thin films and of the Er:SiO_2 emitting layer (chapter 3). In particular the VO_2 thin films will undergo morphological (using an Atomic Force Microscope and a Scanning Electron Microscope), optical (through ellipsometry and the study of the transmittance) and structural characterization (via Grazing Incidence X-Ray Diffraction), while the emitters will be studied through their photoluminescence. Then in chapter 4 I will discuss about the results on the study of the properties of the VO_2 thin films and their dependence on the synthesis condition, with particular focus on the post-deposition annealing process. This will allow us to find the best synthesis recipe, which will then be used to finally fabricate samples with both an emitting layer and a film of vanadia. The results of the study on these samples will be discussed in chapter 5.

Chapter 2

Simulations

In order to decide which geometry of the samples is the most promising, simulations are a powerful tool. In particular, in the case of multilayers with simple parallel planar interfaces (i.e. without nanostructures), one can use the model developed by Chance, Prock and Silbey in 1978 (henceforth referred as CPS model) [9]. This model has the advantage of being analytical, and has proven very successful in predicting the effect of interfaces on emitters [11, 12, 20, 10].

2.1 The CPS model

The CPS model treats the emitter embedded in a matrix as a classical forced damped harmonic dipole oscillator, described by the following equation [24]

$$\frac{d^2p}{dt^2} + \Gamma_0 \frac{dp}{dt} + \omega_0^2 p = \frac{e^2}{m} E_r \tag{2.1}$$

where p is the momentum of the oscillator, e is the fundamental charge and m the effective mass. Γ_0 and ω_0 are respectively the decay rate (inverse lifetime) and angular frequency of the emitter in the absence of interfaces, namely in the bulk matrix, while E_r is the reflected electric field which acts as a forcing term. In the presence of interfaces, the dipole oscillates with frequency ω and has a decay rate Γ. The expressions for ω and Γ depend on the particular geometry considered, but in most cases $|\omega - \omega_0| \ll \omega, \omega_0$ [24], so we will focus only on Γ.

At this point we can consider that, in the absence of interfaces, the emitter has a radiative decay rate $\Gamma_{0,r}$ and a non-radiative one $\Gamma_{0,nr}$. The total decay rate, which is the one experimentally measurable, is simply the sum of the two, while the fraction of decays that produce a photon is the quantum efficiency q

$$\Gamma_0 = \Gamma_{0,r} + \Gamma_{0,nr} \qquad q = \frac{\Gamma_{0,r}}{\Gamma_0} \tag{2.2}$$

Since the non-radiative decay process is due to interactions between the emitter and defects in the matrix close to it, it is reasonable to assume that it is not modified by the presence

of interfaces [11], which will affect only the radiative contribution. Thus, in the presence of interfaces the total decay rate is:

$$\Gamma = \Gamma_r + \Gamma_{nr} = \Gamma_r + \Gamma_{0,nr} \tag{2.3}$$

By putting into a function g all the information about the specific geometry considered, the radiative decay rate of a single emitter can be expressed as

$$\Gamma_r(z) = \Gamma_{0,r}\left(1 + \int_0^\infty g(u,z)\,du\right) \tag{2.4}$$

where z is the distance between the emitter and the first interface and $u = \frac{k_\parallel}{k}$: $k_\parallel$ is the projection of the wave vector on the direction parallel to the interface and k is the modulus of the far field wave vector. Thus $u \in [0,1]$ represents radiation that actually reaches the far field, while $u > 1$ refers to coupling of near field radiation with surface plasmon polaritons and lossy surface waves [25] traveling on the interfaces. Since these processes can be converted back to photons by coupling with a grating [26, 27], they are still considered a contribution to the 'radiative' decay rate; however, for this work there is no grating and so they act as effective non-radiative decay routes. Considering this, one can define the contribution to the decay rate that comes from photons that reach the far field by simply limiting the integral domain to $[0,1]$. More generally if the photons are collected using a lens with numerical aperture NA_{lens} and the sample is held with the interfaces perpendicular to the optical axis, the effective numerical aperture seen by the emitter is simply $NA = NA_{lens}/n_1$, where n_1 is the refractive index of the matrix into which the emitters are embedded. Hence the decay rate associated to the photons that are collected by the lens and thus measured comes from the integral over the $[0, NA]$ interval.

To better understand the nomenclature used, let us unwrap the different contributions to the total decay rate:

$$\begin{aligned}
\Gamma &= \Gamma_r + \Gamma_{nr} \\
&= \Gamma_{0,r}\left(1 + \int_0^\infty g\,du\right) + \Gamma_{0,nr} \\
&= \Gamma_0\left(q\left(1 + \int_0^\infty g\,du\right) + (1-q)\right) = \Gamma_0\left(1 + q\int_0^\infty g\,du\right) \\
&= \Gamma_0\left(q\left(NA + \int_0^{NA} g\,du\right) + q\left(1 - NA + \int_{NA}^1 g\,du\right) + q\int_1^\infty g\,du + (1-q)\right)
\end{aligned} \tag{2.5}$$

Referring to the last row of eq. (2.5): the first term (that we can call Γ_c) is the contribution given by photons that are collectible by the experimental apparatus, the second term is the contribution from photons that reach the far field but are not collected, the third term is the contribution of surface plasmons and lossy surface waves whilst the last term is due to intrinsic non-radiative processes. If we call $\Gamma_{r,FF}$ the sum of the first two terms, we can define the apparent quantum yield or far field efficiency

$$q_a = \frac{\Gamma_{r,FF}}{\Gamma} = \frac{1 + \int_0^1 g\,du}{\frac{1}{q} + \int_0^\infty g\,du} \tag{2.6}$$

The radiative decay rate can be split into two contributions according to the orientation of the dipole: either parallel ($\parallel$) or perpendicular ($\perp$) to the interface. Assuming an isotropic distribution of dipoles one can write

$$\Gamma_r^{iso} = \frac{1}{3}\left(2\Gamma_r^{\parallel} + \Gamma_r^{\perp}\right) \tag{2.7}$$

Another important distinction is whether the transition the emitter performs is of Electric (ED) or Magnetic (MD) Dipole nature, but for now let us focus on the ED transition.

In the following subsections I will the explain the g functions for four different geometries, increasing the complexity of the system. The focus will be on the final formulas rather than on their derivation, as a detailed description of the derivation of the following formulas can be found in [9, 28, 24]

2.1.1 Single Interface (SI)

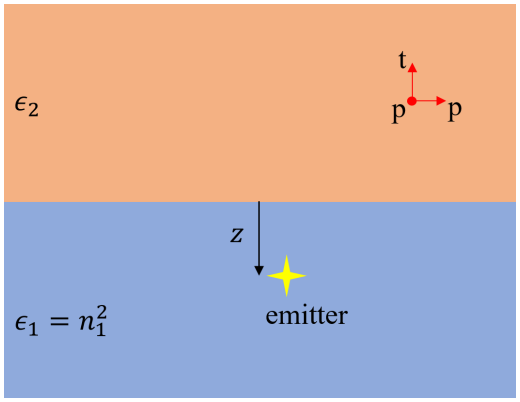

Figure 2.1: Schematics of the SI geometry. On the top right are the two possible orientations for the dipoles: parallel (p) or perpendicular (t) to the interfaces.

The simplest configuration is the one with a single emitter embedded in a non absorbing matrix with refractive index n_1 at a distance z from the interface with a second material with dielectric function ϵ_2, possibly absorbing (fig. 2.1). In this case the relation $\epsilon_2 = n_2^2$ will still be valid but both ϵ_2 and n_2 will be complex numbers. In order to consider only a single interface both the matrix and the second medium are assumed semi-infinite. In practice this translates to the requirement of being optically thick, i.e. their thickness has to be at least several times $\frac{1}{\alpha}$, where α is the absorption coefficient of the material.

Let us define the two Fresnel coefficients

$$r^{\parallel} = \frac{\epsilon_1 a_2 - \epsilon_2 a_1}{\epsilon_1 a_2 + \epsilon_2 a_1} \qquad r^{\perp} = \frac{a_1 - a_2}{a_1 + a_2} \tag{2.8}$$

where

$$a_1 = -i\sqrt{1-u^2} \qquad a_2 = -i\sqrt{\frac{\epsilon_2}{\epsilon_1} - u^2} \tag{2.9}$$

If we also define $\kappa = \frac{4\pi n_1 a_1}{\lambda}$, the two g functions can then be expressed as

$$g^{\parallel} = \frac{3}{4}\,\mathrm{Im}\left(\left((1-u^2)r^{\parallel} + r^{\perp}\right)\frac{u}{a_1}e^{-\kappa z}\right) \tag{2.10}$$

$$g^{\perp} = -\frac{3}{2}\,\mathrm{Im}\left(r^{\parallel}\frac{u^3}{a_1}e^{-\kappa z}\right) \tag{2.11}$$

Despite its simplicity this model is very powerful, and has already been successfully used to describe the modification of the lifetime of Erbium ions in silica [5, 11].

2.1.2 Finite Thickness (FT)

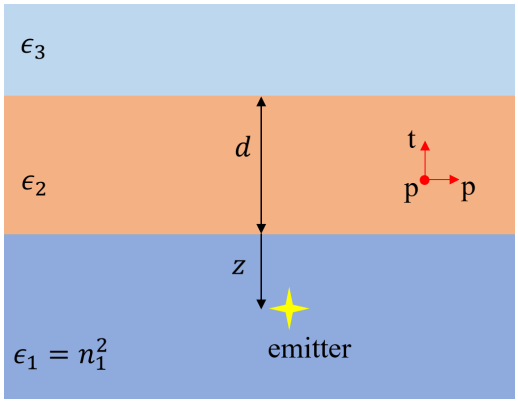

Figure 2.2: Shematics of the FT geometry.

If we now assume that the matrix is still semi-infinite but medium 2 has a finite thickness d (fig. 2.2), the formulas get a little bit more complicated. We start by introducing

$$a_j = -i\sqrt{\frac{\epsilon_j}{\epsilon_1} - u^2}$$

$$h_j = i\frac{2\pi n_1}{\lambda}a_j = i\frac{\kappa}{2a_1}a_j$$

and $q_2 = \tan(h_2 d)$. Then we define

$$R = \frac{h_2 - ih_3 q_2}{h_3 - ih_2 q_2} \tag{2.12}$$

$$S = \frac{h_2\epsilon_3 - ih_3\epsilon_2 q_2}{h_3\epsilon_2 - ih_2\epsilon_3 q_2} \tag{2.13}$$

which allow us to write

$$r_{eff}^{\perp} = \frac{h_1 R - h_2}{h_1 R + h_2} \qquad r_{eff}^{\parallel} = -\frac{h_1 S\epsilon_2 - h_2\epsilon_1}{h_1 S\epsilon_2 + h_2\epsilon_1} \tag{2.14}$$

and finally

$$g^{\parallel} = \frac{3}{4}\,\mathrm{Im}\left(\left((1-u^2)r_{eff}^{\parallel} + r_{eff}^{\perp}\right)\frac{u}{a_1}e^{-\kappa z}\right) \tag{2.15}$$

$$g^{\perp} = -\frac{3}{2}\,\mathrm{Im}\left(r_{eff}^{\parallel}\frac{u^3}{a_1}e^{-\kappa z}\right) \tag{2.16}$$

which have the same form of the previous configuration.

2.1.3 Double Interface (DI)

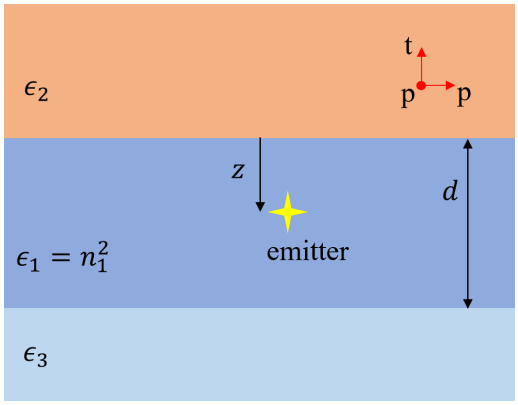

Figure 2.3: Schematics of the DI geometry.

This time we consider the matrix to have a finite thickness d, thus being sandwiched between medium 2 and medium 3, which are assumed to be semi-infinite (fig. 2.3). With the same definition of a_j used previously we write the Fresnel coefficients in the same way as for the single interface problem (eq. (2.8)):

$$r_{12}^{\parallel} = \frac{\epsilon_1 a_2 - \epsilon_2 a_1}{\epsilon_1 a_2 + \epsilon_2 a_1} \qquad r_{12}^{\perp} = \frac{a_1 - a_2}{a_1 + a_2}$$

$$r_{13}^{\parallel} = \frac{\epsilon_1 a_3 - \epsilon_3 a_1}{\epsilon_1 a_3 + \epsilon_3 a_1} \qquad r_{13}^{\perp} = \frac{a_1 - a_3}{a_1 + a_3}$$

If we then define the function $F(x,y) = 1 + ye^{-\kappa x}$, we can express the two g functions as

$$g^{\parallel} = \frac{3}{4}\,\mathrm{Im}\left(\left((1-u^2)(f_+^{\parallel} - 1) + f^{\perp} - 1\right)\frac{u}{a_1}\right) \tag{2.17}$$

$$g^{\perp} = -\frac{3}{2}\,\mathrm{Im}\left((1 - f_-^{\parallel})\frac{u^3}{a_1}\right) \tag{2.18}$$

where

$$f^{\perp} = \frac{F(z, r_{12}^{\perp})F(d-z, r_{13}^{\perp})}{F(d, -r_{12}^{\perp} r_{13}^{\perp})} \tag{2.19}$$

$$f_{+}^{\parallel} = \frac{F(z, r_{12}^{\parallel})F(d-z, r_{13}^{\parallel})}{F(d, -r_{12}^{\parallel} r_{13}^{\parallel})} \tag{2.20}$$

$$f_{-}^{\parallel} = \frac{F(z, -r_{12}^{\parallel})F(d-z, -r_{13}^{\parallel})}{F(d, -r_{12}^{\parallel} r_{13}^{\parallel})} \tag{2.21}$$

2.1.4 Double Interface with Finite Thickness (DIFT)

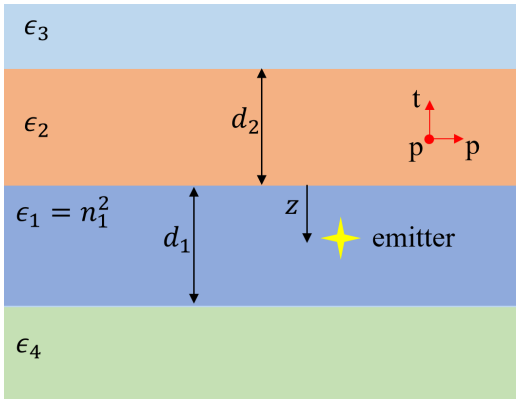

Figure 2.4: Schematics of the DIFT geometry.

The only thing left to do is combining the last two results modeling a finite thickness both for the matrix and for medium 2 (fig. 2.4). First we start by computing the effective medium of 2 and 3, using the same formulas of the FT model for R and S (eqs. (2.12) and (2.13) respectively), and $r_{eff}^{\perp}$ and $r_{eff}^{\parallel}$ (eq. (2.14)) with the only adjustment of $q_2 = \tan(h_2 d_2)$: Then we proceed similarly to what was done for the DI model:

$$r_{14}^{\parallel} = \frac{\epsilon_1 a_4 - \epsilon_4 a_1}{\epsilon_1 a_4 + \epsilon_4 a_1} \tag{2.22}$$

$$r_{14}^{\perp} = \frac{a_1 - a_4}{a_1 + a_4} \tag{2.23}$$

and finally we do the substitution

$$r_{eff} \mapsto r_{12} \qquad r_{14} \mapsto r_{13} \qquad d_1 \mapsto d$$

in eqs. (2.19) to (2.21).

2.1.5 Magnetic Dipole

All the results shown above are computed for the Electric Dipole (ED) transition. To obtain the ones for the Magnetic Dipole (MD), one simply needs to apply the following substitution [9].

$$r^{\parallel} \mapsto -r^{\perp} \qquad r^{\perp} \mapsto -r^{\parallel}$$

2.1.6 Distribution of emitters

Until now we have considered a single emitter, or, more realistically, a layer of emitters with negligible thickness, all at a distance z from the first interface. This was the situation of the pioneering experiments of Drexhage [8] where he used a mono-layer of emitters. However a more realistic situation is the one where the probability distribution $f(z)$ of

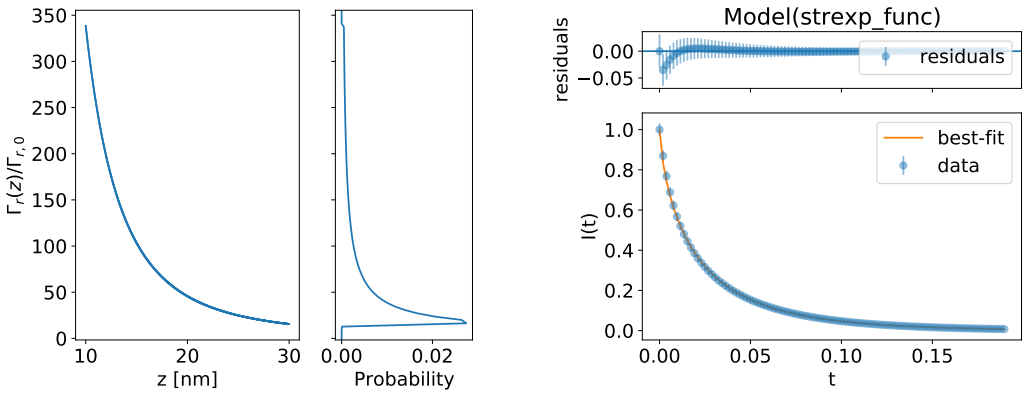

Figure 2.5: (Left): Example of a typical trend of the radiative decay rate as a function of the distance from the interface z with on the side the histogram corresponding to the probability distribution $f(\Gamma_r)$. (Right): Stretched exponential fit of $I(t)$. These data come from simulations of a SI model with 20 nm of Er:SiO_2 spaced by 10 nm of SiO_2 from the interface with rutile VO_2.

finding an emitter at a distance between z and $z + dz$ from the first interface is not a Dirac's δ. The fact that $f(z)$ is a probability distribution means that

$$f(z) \geq 0 \ \forall z \qquad \int_0^\infty f(z)dz = 1 \tag{2.24}$$

For this work, the samples are fabricated by magnetron sputtering co-deposition (section 3.1.2), and it is reasonable to assume that the deposition rate is constant with time. Hence $f(z)$ can be assumed to be a box distribution [11], namely

$$f(z) = \begin{cases} \frac{1}{z_2 - z_1} & \text{if } z_1 < z < z_2 \\ 0 & \text{otherwise} \end{cases} \tag{2.25}$$

As can be seen from the left panel of fig. 2.5, the dependence of the radiative decay rate on z (left plot) translates the distribution over z $f(z)$ to a distribution over Γ_r $f(\Gamma_r)$ (right plot), according to

$$f(\Gamma_r(z)) \propto f(z)/\frac{d\Gamma_r}{dz} \tag{2.26}$$

At this point one has to extract an average value from $f(\Gamma_r)$, however taking simply the mean of the distribution would give a biased result, so the best way is instead to compute the time-dependent trend of the number of emitters in their excited state as

$$N(t) = N_0 \int_0^\infty dz f(z) e^{-\Gamma(z)t} \tag{2.27}$$

and then fit $N(t)/N_0$ with a stretched exponential function, obtaining something similar to what shown in the right panel of fig. 2.5:

$$d_s(t; \tau, \beta) = e^{-(t/\tau)^\beta} \tag{2.28}$$

where $\beta \in [0, 1]$ is the stretching factor. If we denote Euler's gamma function as $\Gamma_E(\cdot)$, the effective decay time can be computed as

$$\tau_{eff} = \frac{\Gamma_E(1/\beta)}{\beta}\tau = \int_0^\infty d_s(t)dt \tag{2.29}$$

and hence the effective total decay rate is obtained as $\Gamma^{eff} = 1/\tau_{eff}$. This approach has already been used to obtain an effective decay rate ([29, 30]) and its purpose is to be as close as possible to the way the experimental decay rates are estimated, in order to be able to easily compare the two values.

It needs to be said that in the experimental practice we actually do not measure the number of excited emitters $N(t)$ directly, but rather the number of detected photons $\phi(t)$. In the case where the emitting layer has a negligible thickness, $\phi(t)$ can be written as

$$\phi(t) = \eta\Gamma_c N(t) = \eta\Gamma_c e^{-\Gamma t} \tag{2.30}$$

where Γ_c is the decay rate related to the collected photons (first term in the last row of eq. (2.5)) and η is a factor that accounts for the efficiency of the experimental setup. Then, when dealing with a distribution of emitters the trend of the intensity can be obtained by performing the integral over z

$$\phi(t) = \eta \int_0^\infty dz f(z)\Gamma_c(z)e^{-\Gamma(z)t} \tag{2.31}$$

and if both $\Gamma_c(z)$ and $\Gamma(z)$ vary a lot this could have an effective decay rate that is different from the one of $N(t)$. Fortunately, as it will be shown later, if the numerical aperture of the collecting lens is small enough, $\Gamma_c(z)$ has a very weak dependence on z and hence can be assumed to be constant. With this assumption $\phi(t) \propto N(t)$ and fitting the one or the other is the same.

At this point to estimate the effective decay rate we have to simulate $N(t)$ and hence the total decay rate $\Gamma(z)$ as a function of the distance from the interface, which can be written as

$$\Gamma(z) = \Gamma_r(z) + \Gamma_{0,nr} = \Gamma_{0,r}P(z) + \Gamma_{0,nr} \tag{2.32}$$

where $P(z) = \Gamma_r(z)/\Gamma_{0,r}$ is the Purcell factor and $\Gamma_{0,nr}$ is the non-radiative decay rate. Since $\Gamma_{0,nr}$ is due to defects in the emitting layer and is specific of the sample used, it would be nice to exclude it from the simulations and add it back at the end. This can be done by calculating

$$N^*(t) = \int_0^\infty dz f(z)e^{-\Gamma_r(z)t} \tag{2.33}$$

fitting it with a stretched exponential and then obtaining the effective radiative decay rate Γ_r^{eff}, as described before for $N(t)$. Then we can approximate the total decay rate as $\Gamma^{eff} \approx \Gamma_r^{eff} + \Gamma_{0,nr}$, and this is a good approximation if $\Gamma_{0,nr}$ is quite small or $N^*(t)$ doesn't exhibit a very stretched behavior, which is the case if the emitters are sufficiently far from the interface.

Finally, without any further approximations, we can also remove $\Gamma_{0,r}$ from the simulation by rescaling the time coordinate and hence defining

$$I(t) = N^*(t/\Gamma_{0,r}) = \int_0^\infty dz f(z) e^{-P(z)t} \tag{2.34}$$

which is the one displayed in the right panel of fig. 2.5 and allows us to directly compute the effective Purcell factor P^{eff}. This way the results we will obtain are dependent only on the geometry of the sample and not on the properties of the emitters.

Technical details Obtaining an estimate of the effective decay rate requires to fit a function $I(t)$ that itself requires to compute an integral at every point t, which contains the function $\Gamma_r(z)$ that per se is an integral over u (eq. (2.4)). It is clear that without caution the computational cost of these nested operation can increase dramatically, hindering the possibility to explore many different sample geometries. So, to overcome these issues I coded in such a way that $\Gamma_r(z)$ is computed in the fewest amount of point that give the maximum information about it and then it is interpolated with a cubic spline. Since (as it can be seen in fig. 2.5 left) $\Gamma_r(z)$ is pretty smooth, the error of the interpolation is very small. At this point this interpolating function is used in place of the real $\Gamma_r(z)$ when computing $I(t)$.

Another aspect that requires some care is how to fit $I(t)$. In practice the function $I(t)$ is evaluated at points evenly spaced between 0 and t_{max}, but, as can be seen from fig. 2.5 right, there is a non-chaotic trend in the residuals, which means that in principle the result of the fit depends on the choice of t_{max}, which is arbitrary. After some experimenting I found that adding a fake Poissonian error on the computed intensities $\sigma(I) \propto \sqrt{I}$ stabilizes the fit, almost eliminating the dependence on t_{max}. For this reason this is the way I decided to go for.

2.2 Results

In order to familiarize with the model, let us first take a look at what is the behavior of the Purcell factor P as a function of the distance from the interface in a simple Single Interface (see fig. 2.1) model consisting of a silica matrix with an overlayer of optically thick rutile vanadia on top of it. The wavelength of the transition of the Er^{3+} ions is $\lambda = 1540\,\text{nm}$ and at this wavelength the refractive index of SiO_2 is $n_1 = 1.444$ while for the value of the dielectric function of rutile (R) VO_2 we can use the one from [31]: $\epsilon_2^R = -8.1 + i11.9$. On the left panel of fig. 2.6 we can see the different contributions to the ED transition that come from the two possible orientations of the emitting dipoles, namely parallel or perpendicular to the interface. The case of an isotropic distribution of emitters can be computed as

$$P_{iso} = \frac{1}{3}\left(2P_\parallel + P_\perp\right) \tag{2.35}$$

which is the same of eq. (2.7). In the right panel instead we report the Purcell factors P^{ED} and P^{MD} of the Electric Dipole (ED) and Magnetic Dipole (MD) transitions respectively.

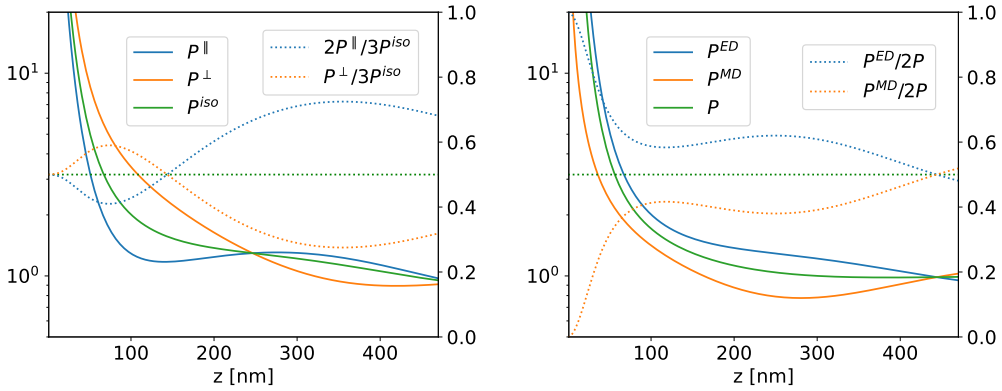

Figure 2.6: (Left): absolute (solid lines, left-hand scale) and relative (dotted lines, right-hand scale) contributions to the ED Purcell factor from the two possible orientation of the emitters. (Right): absolute (solid lines, left-hand scale) and relative (dotted lines, right-hand scale) contributions to the total Purcell factor P from the ED and MD transitions with isotropic emitter orientation.

Since the transition of the Er^{3+} ions at 1540 nm has an equal contribution from the ED and MD transition [32], the average value can be computed as the mean of the two:

$$P = \frac{1}{2}\left(P^{ED} + P^{MD}\right) \tag{2.36}$$

From the plots we can see that the various contributions to P have an oscillating behavior with a value of roughly 1 when the emitter is quite far from the interface ($z > 150\,\text{nm}$), while on the other hand at smaller distances they increase dramatically, diverging as $z \to 0$. The dotted lines in the two plots in fig. 2.6 show the relative contributions to the Purcell factor, and we can see that as $z \to 0$ the contributions from the different orientations become equal (left plot), while the contribution of the MD transition becomes negligible with respect to the ED one. Since we are interested in amplifying the decay rate of the Er^{3+} ions and most importantly obtain a significant contrast in decay rate when the VO_2 changes phase, let us focus on the range $z < 100\,\text{nm}$.

In fig. 2.7 we can see the behavior of the total Purcell factor (in green) and its components (in blue the ED one and in orange the MD one) as a function of the complex dielectric function of the overlayer, where are highlighted the values of for VO_2 in its rutile (R) and monoclinic (M1) phases, where in the latter case $\epsilon_2^{M1} = 10.8 + i2.0$ [31]. As we can see both for the ED and MD components the Purcell factor diverges at

$$\epsilon_2 = -\epsilon_1 = -n_1^2 = -2.09 + 0i \tag{2.37}$$

and also the behavior of the two components is quite different. Since, as we saw earlier, the Electric Dipole component is the one that gets more amplified, the contour lines of P and P^{ED} are quite similar.

If we now plot the the behavior of the Purcell factor as a function of z for the two VO_2 phases in bi-logarithmic scale (fig. 2.8 left) we can see that as the distance z tends to zero

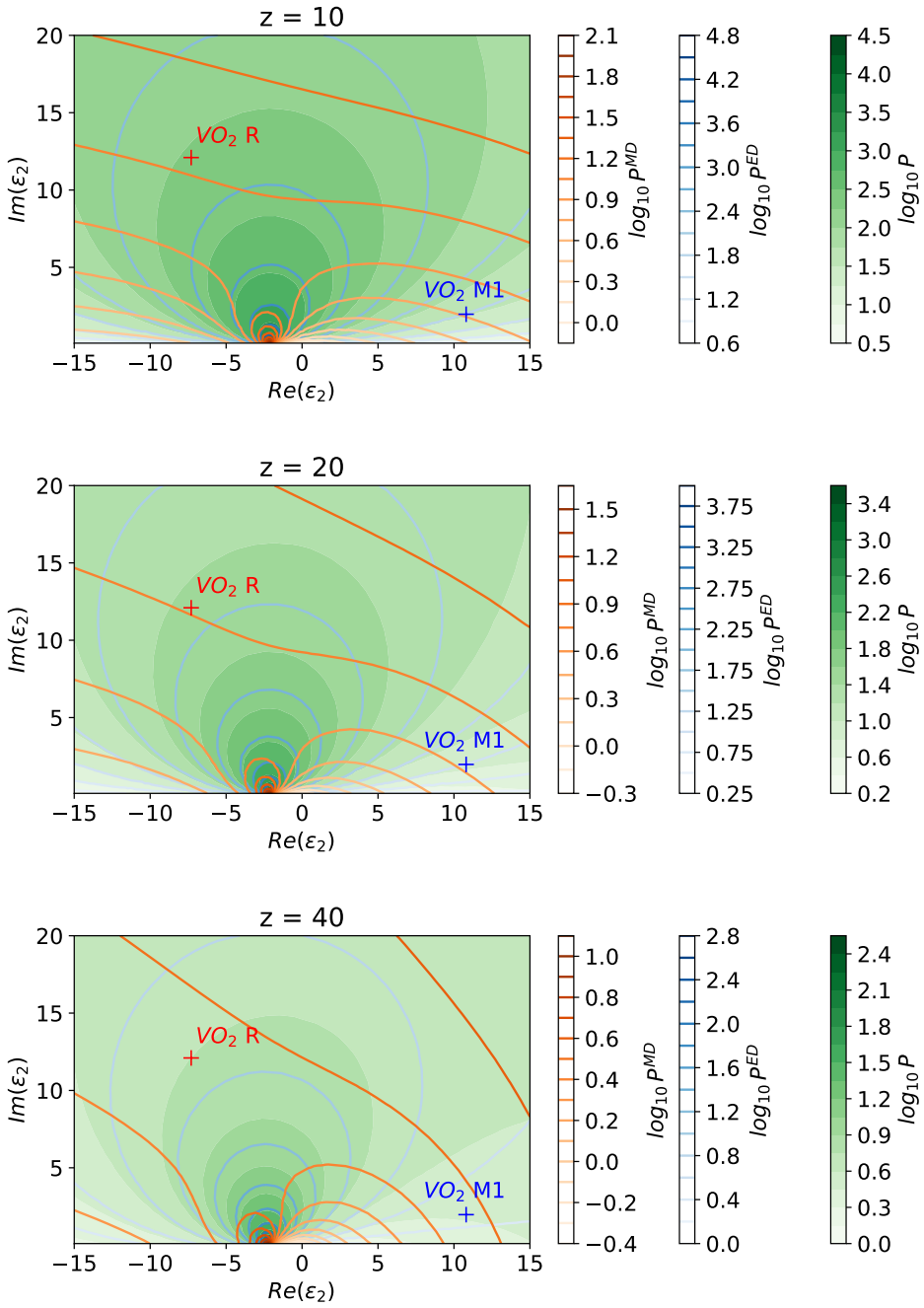

Figure 2.7: Behavior of the Purcell factor as a function of the complex dielectric function of the overlayer at three different distances from the interface ($z = 10$, 20, 40 nm). In green it is reported the total Purcell factor, while in blue and orange are the ED and MD components, respectively.

P diverges as a power-law $P \propto z^{-\alpha}$, and, by performing a linear fit in the bi-logarithmic plot, we can estimate the exponent α. What we find is that $\alpha \to 3$ for the ED (dashed line) and total (solid line) decay rates of both phases while for the MD components (dotted line) $\alpha \to 1$. This fact explains why the Electric Dipole component gets much more amplified than the Magnetic Dipole one. We can then define the switching factor

$$S = \frac{P_R}{P_{M1}} = \frac{\Gamma_{r,R}}{\Gamma_{r,M1}} \tag{2.38}$$

which is important because it quantifies the amount of the active control that the VO_2 phase transition has on the emission properties of the Er^{3+} ions. Since α tends to the same value for the rutile and monoclinic phases, S saturates to a maximum value, which is around 5.8 (right panel of fig. 2.8).

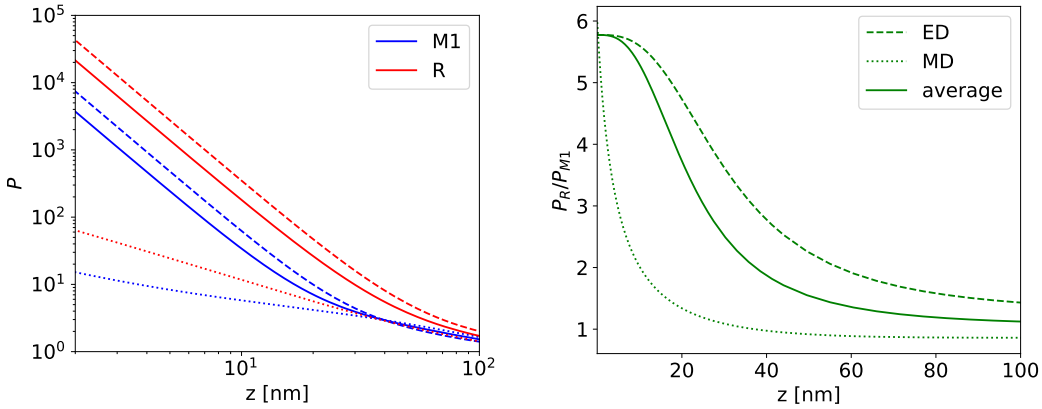

Figure 2.8: Behavior of the Purcell factor as a function of z for monoclinic (blue) and rutile (red) VO_2 (left) and their ratio (right). The dashed lines represent the ED component, the dotted lines the MD one and the solid lines represent the average.

Let us also take a look at the behavior of the normalized decay rate related to the collected photons $\Gamma_c/\Gamma_{0,r}$ as a function of z computed at different numerical apertures. In fig. 2.9 its trend is reported when the overlayer is monoclinic (blue) and rutile (red) VO_2 or air (green) ($\epsilon_2^{air} = 1 + i0$). We can see that for air the ED (dashed line) Γ_c has a higher value with respect to the MD one (dotted line), while for VO_2 the opposite happens. Moreover as the numerical aperture (NA) of the collecting lens is reduced, the differences between the two components become less pronounced. In particular at $NA = 0.26$, which is the numerical aperture of the lens used in our experiments, Γ_c^{ED} and Γ_c^{MD} vary less than 2% over a typical thickness of 20 nm of the emitting layer and so can be assumed to be constant over that range, as said in section 2.1.6. Also, the difference in Γ_c between the monoclinic and rutile phases of VO_2 is below 6% at this numerical aperture, so we can assume them to be the same.

Another important fact that we can observe from fig. 2.9 is that the average Γ_c (solid line) becomes basically independent with respect to the dieletric function of the overlayer and the distance from the interface when $NA < 0.6$. Moreover, even when $NA = 1$ (i.e. we

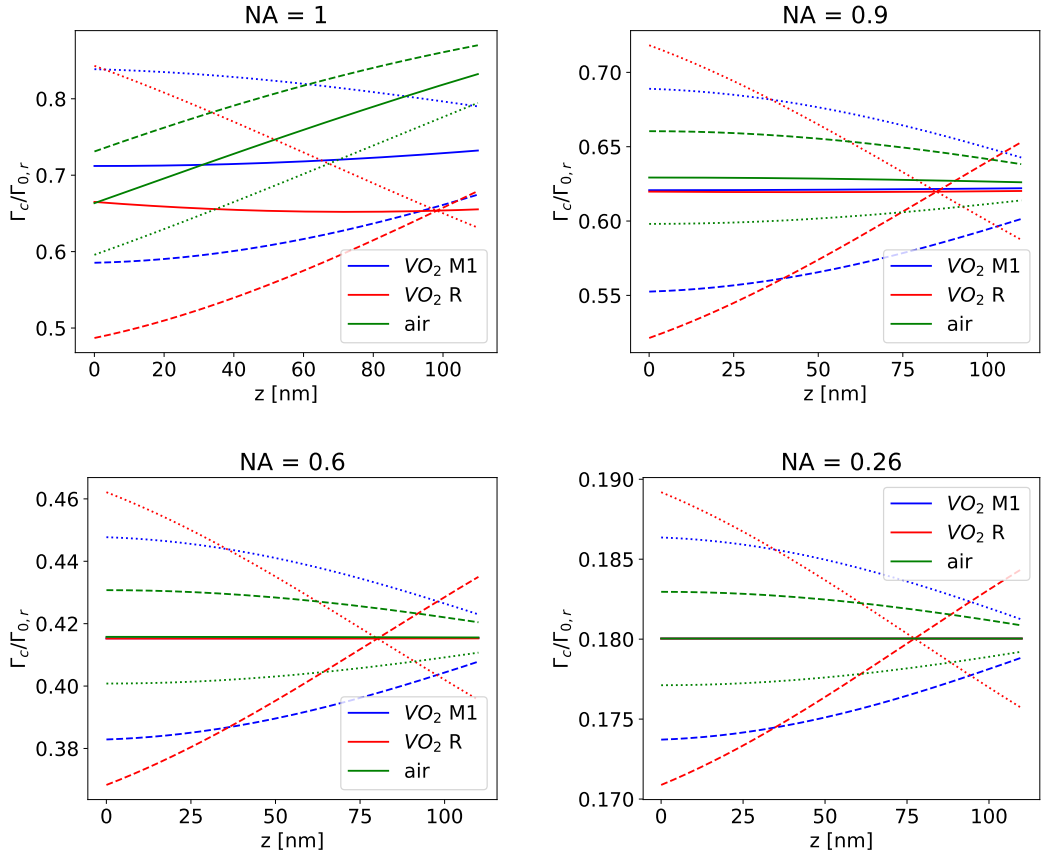

Figure 2.9: Behavior of the normalized collected decay rate $\Gamma_c/\Gamma_{0,r}$ as a function of z at different numerical apertures ($NA = 1, 0.9, 0.6, 0.26$). Similarly to fig. 2.8, the dashed lines represent the ED component, the dotted lines the MD one and the solid lines represent the average.

assume to collect all the photons that reach the far field, so $\Gamma_c = \Gamma_{r,FF}$) we can observe that there is no divergence as $z \to 0$, which indicates that all the amplification of the total decay rate comes from effective non radiative decay routes, namely surface plasmon polaritons and lossy surface waves. The fact that the total decay rate diverges as $z \to 0$ but the far field one $\Gamma_{r,FF}$ doesn't means that the far field efficiency q_a tends to 0 with z and actually, since there is no strong dependence of $\Gamma_{r,FF}$ with respect to z,

$$q_a(z) = \frac{\Gamma_{r,FF}(z)}{\Gamma(z)} \approx \frac{\Gamma_{r,FF}}{\Gamma(z)} \propto \frac{1}{P(z)} \tag{2.39}$$

2.2.1 Optimization of the sample geometry

Now that we understood the basics of the CPS model, we can use it to properly design the geometry of our sample. The typical structure of a sample is the one displayed on the left side of fig. 2.10, consisting of a series of thin films deposited on top of each other. Starting from the bottom we have a substrate of bulk SiO_2, then the emitting layer Er:SiO_2, then a SiO_2 spacer and finally the VO_2 film. In particular we would like to have:

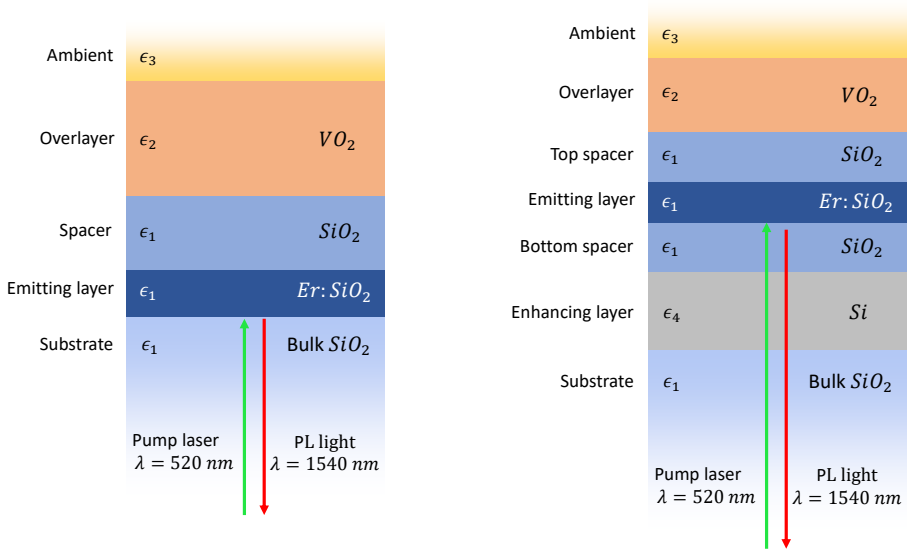

Figure 2.10: Schematics of the basic structure of a sample (left), and a more complex one with an enhancing layer (right). The sample is excited with a pump laser beam at 520 nm (green arrow) and the photoluminescent emission at 1540 nm (red arrow) is collected from the same side.

1. A sufficiently high intensity of the emitted light.
2. A high switching factor S.
3. Sufficiently high far field efficiencies q_a both for the monoclinic and the rutile phases in order to be able to measure the decay rate in the two cases.
4. A not too strong dependence of the results on the thicknesses of the various thin films that compose the sample, otherwise it will be difficult to compare the prediction of the model with the results of the simulations.

The first point can be satisfied increasing the number of Er^{3+} ions in the sample, which can be achieved by having a thicker emitting layer[1]. However its thickness needs to be small enough that there isn't too much variation of the lifetime across the emitting layer, so we decided to settle on a thickness of 20 nm.

If we look at the right panel of fig. 2.8 we can see that a high switching factor can be achieved by having the emitters as close to the interface with VO_2 as possible. However if we place them too close to the interface we will have a very low far field efficiency and in this case, also, tiny errors on the thickness of the spacer would propagate into massive variations of the predicted decay rate. Thus, a compromise needs to be found. Lastly there is still one more parameter that we can play with, and it is the thickness of the VO_2 layer. However, in order to investigate it we need to move from the simple Single

[1]Another possibility would be increasing the concentration of the Er^{3+} ions in the emitting layer. However, this would also increase the non-radiative decay rate due to concentration quenching phenomena [33, 34]. For this reason we decided to keep the atomic concentration of Er^{3+} ions at 0.5%.

Interface (SI) model (section 2.1.1) to the slightly more complex Finite Thickness (FT) one (section 2.1.2).

Thicknesses of the SiO_2 spacer and the VO_2 overlayer By having fixed the thickness of the emitting layer and assuming that the ambient above the VO_2 overlayer is air ($\epsilon_3 = 1 + i0$), the structure of the sample has only two free parameters: the thickness of the spacer layer (t_{spacer}) and the one of the VO_2 film (t_{VO_2}). To study the effect of these two parameters on the properties of the sample (P_{M1}, P_R, S, q_a^{M1}, q_a^R...) we need to evaluate them at may values of t_{spacer} and t_{VO2}. However, since the emitting layer has a finite thickness, we need to perform all the computations described in section 2.1.6, which are quite time consuming. So, instead of choosing a priori a grid of values for t_{spacer} and t_{VO2}, I used the python package *adaptive* [35], which iteratively creates an adaptive grid adding new points were the monitored function changes the most, ensuring the maximum detail with the least number of points.

If we look at the first plot of fig. 2.11, we can see the familiar result that putting the emitters closer to the interface (i.e. small values for t_{spacer}) yields higher Purcell factors (blue and red lines) and also a higher switching factor S (green shades). However a new feature emerges, which wasn't visible when assuming $t_{VO_2} \to \infty$, that is high values of S at considerably large spacer thicknesses when the VO_2 film is very thin. Moreover, this region seems also promising because it has higher far field efficiencies, as can be seen in the second plot of fig. 2.11. Unfortunately, if we look at the last plot in fig. 2.11, where the ambient is silicon instead of air, we can see that these desirable features are lost. This means that in order to observe them we need the VO_2 to be exposed to air, and this is not possible with our experimental setup (section 3.2.8) because we need to thermally activate the phase transition of VO_2. In practice, since the back side of the sample needs to be left exposed for the pump laser and the collection of the photoluminescence (PL) light (see fig. 2.10), the VO_2 side will be glued to a silicon wafer and then to the copper tip of a heater. Moreover, even if we managed to solve these experimental issues, working at small thicknesses of the VO_2 overlayer poses the further complication of the fact that the top surface of the VO_2 film is rugged due to the presence of crystalline grains (fig. 4.1), which means that the interface with the ambient isn't smooth and so we are potentially out of the hypotheses of the CPS model. So, even if studying samples with very thin films of VO_2 will be interesting for future works, for this thesis we decided to stay on the safer terrain of

$$t_{VO_2} > 120\,\text{nm}$$

where the film of vanadia can be assumed optically thick and thus the emitters won't feel the roughness of the surface and the medium above it. This can be seen observing that in the top and bottom plots of fig. 2.11 the contour lines are nearly vertical for $t_{VO_2} > 120\,\text{nm}$, which means that there is no more dependence on the thickness of the VO_2 film.

Having said so, we also decided to keep the far field efficiency of the rutile phase q_a^R,

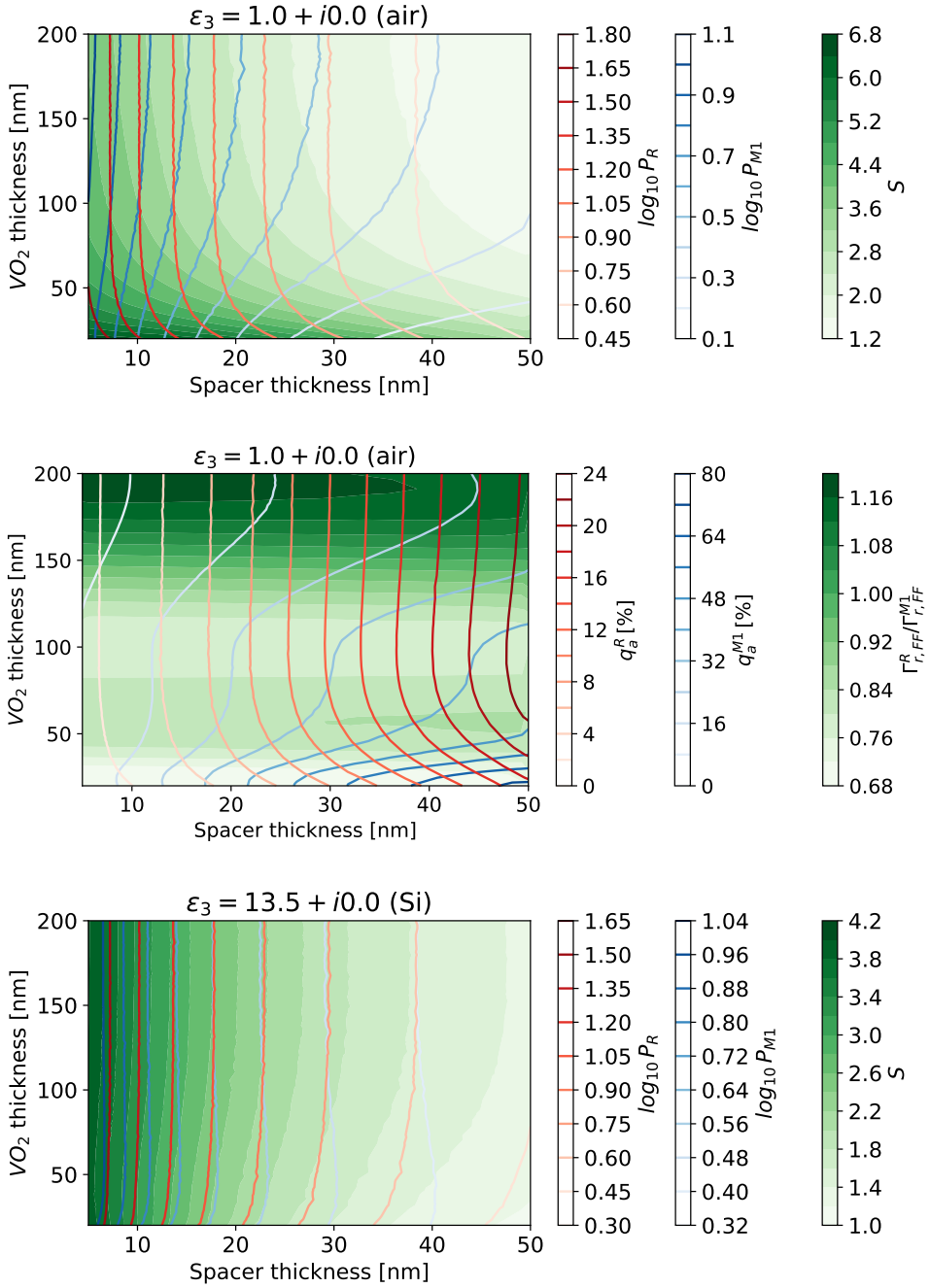

Figure 2.11: Behavior of the properties of the sample as a function of t_{spacer} and t_{VO2}. On the top and bottom plot S is in green, P_{M1} in blue and P_R in red; in the middle plot in green is the ratio between the far field decay rates $\Gamma^R_{r,FF}/\Gamma^{M1}_{r,FF}$, in blue q_a^{M1} and in red q_a^R. In the first two plots the ambient is air, while in the last one is silicon.

which is always lower than its monoclinic counterpart, above 5%, which means

$$t_{spacer} > 15\,\text{nm}$$

With these constraints, the maximum Purcell factor achievable is around 5 for the monoclinic phase and 14 for the rutile one, yielding a switching factor of $S \approx 2.8$.

Si enhancing layer The intrinsic radiative decay rate for Er^{3+} ions in a silica matrix is $\Gamma_{0,r} \approx 100\,\text{s}^{-1}$ ([12, 32]) and, if we consider a non-radiative decay rate of $\Gamma_{0,nr} \approx 20\,\text{s}^{-1}$ ([11]), we can compute the expected emission lifetimes for the two phases of VO_2:

$$\tau_{M1} = \frac{1}{\Gamma_{0,r}P_{M1} + \Gamma_{0,nr}} \approx 2\,\text{ms} \qquad \tau_R = \frac{1}{\Gamma_{0,r}P_R + \Gamma_{0,nr}} \approx 0.7\,\text{ms} \tag{2.40}$$

It would be interesting to further reduce these lifetimes, and a possible way of achieving it is by having a silicon layer of thickness t_{Si} below the emitter layer, which adds another interface to the system and hence can be used to further enhance the Purcell factors [12]. The choice to use Si is motivated by the fact that it is transparent at 1540 nm, so it doesn't absorb the PL light, but it has a high refractive index $n_{Si} = 3.08$, yielding a high contrast with respect to the one of silica ($n_{SiO_2} = 1.44$). Moreover, it has a quite low absorption coefficient at the wavelength of the pump laser (a 200 nm thick Si with SiO_2 on both sides has a transmittance of roughly 50% at 520 nm), which still allows to excite the Er^{3+} ions.

The structure of a sample of this kind is the one displayed on the right of fig. 2.10, where, starting from the bottom, we have a silica substrate, then the silicon enhancing layer, a bottom SiO_2 spacer of thickness t_{bs}, and finally the same layers of a sample without the enhancing layer. If we assume to have an optically thick vanadia film, we can describe our sample using the Double Interface with Finite Thickness (DIFT) model (section 2.1.4). In particular, referring to fig. 2.4, medium 1 and 3 are silica, medium 2 is Si and medium 4 VO_2; also d_1 is the sum of the thickness of the two SiO_2 spacers and of the Er:SiO_2 emitting layer, while $d_2 = t_{Si}$.

If we fix the thickness of the top spacer to 15 nm, we can investigate the effects of t_{bs} and t_{Si}. As we can see from fig. 2.12 all properties of the sample have an oscillating behavior with respect to t_{Si}, due to the alternating constructive and destructive interference between the emitted field and the one reflected by the interface between the Si layer and the SiO_2 substrate. We can also observe that the oscillations of the Purcell factors (blue and red lines in the top plots) are almost in phase opposition with respect to the ones of the far field efficiencies (blue and red lines in the bottom plot), and this is once again due to the fact that $\Gamma_{r,FF}$ doesn't vary much and so P and q_a are almost inversely proportional. However a good compromise can be found at

$$t_{bs} = 10\,\text{nm} \quad t_{Si} = 335\,\text{nm} \tag{2.41}$$

and if we compare the results for this geometry (second row of table 2.1) to the ones of the previous geometry without the enhancing layer (first row), we can see that we amplified

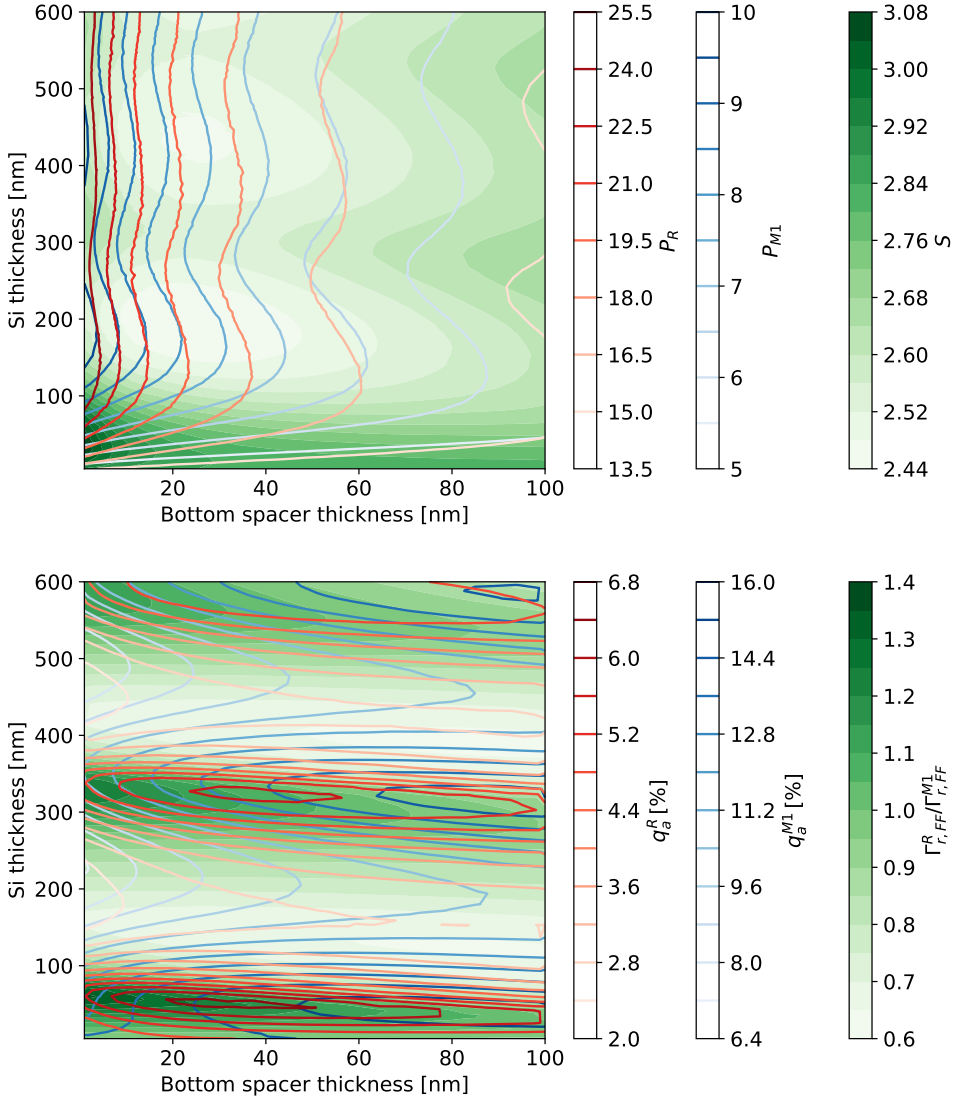

Figure 2.12: Behavior of the properties of a sample with a Si enhancing layer as a function of the t_{bs} and t_{Si}. Similarly to fig. 2.11, on the top plot S is in green, P_{M1} in blue and P_R in red, while in the bottom one in green is the ratio between the far field decay rates $\Gamma^R_{r,FF}/\Gamma^{M1}_{r,FF}$, in blue q_a^{M1} and in red q_a^R.

Si layer	t_{spacer} [nm]	t_{bs} [nm]	t_{Si} [nm]	P_{M1}	P_R	q_a^{M1}[%]	q_a^R[%]	S
no	15	–	–	5.0	14.0	14	4.7	2.84
yes	15	10	335	8.4	21.7	11	5.3	2.58
no	10.5	–	–	6.5	21.6	11	3.0	3.30

Table 2.1: Comparison of the sample properties with different geometries, both with and without the Si enhancing layer.

the Purcell factors by roughly 60% and increased q_a for the rutile phase while reducing the switching factor only by 10%. For comparison, enhancing the Purcell factors by simply reducing the thickness of the top spacer (third row of table 2.1) would instead decrease the quantum efficiencies making the experimental measurements more difficult.

In the end the use of a silicon enhancing layer is certainly an interesting possibility to explore in future works, however, in this thesis, unfortunately, there wasn't enough time to study samples of this kind also from an experimental point of view.

Chapter 3

Methods

3.1 Synthesis

All the samples of this thesis are produced by Magnetron Sputtering co-depositions (hence simply sputtering), which yield an amorphous structure of the deposited thin films. To obtain a crystalline structure, the samples are then annealed in different conditions.

3.1.1 Cleaning

As will be explained in more detail in the next chapter, the cleaning of the substrates proved to be a crucial factor in the quality of the samples. In particular the SiO_2 (HSQ100 by Heraeus [36]) and Si substrates were cleaned for 1 hour in acid piranha solution (3:1 - concentrated H_2SO_4 : 30% H_2O_2) at 70 °C, then rinsed in ultra pure water (resistivity of 18.2 MΩ cm) and dried with compressed air. This type of cleaning is performed also between the Er:SiO_2 and VO_2 depositions, but cannot be applied after the deposition of the VO_2 layer as it would damage it. In those cases, less aggressive solvents can be used, namely acetone or toluene, to remove any organic residuals on the samples. To help the cleaning process the samples can be 'sonicated', by putting them in a beaker with the solvent and then applying ultrasounds to the beaker, which helps literally shaking off residuals from the sample surface.

3.1.2 Magnetron Sputtering deposition

Deposition by sputtering works by ejecting atoms from one or more (in this case the process is called sputtering co-deposition) targets by means of ion bombardment. The ejected atoms then possibly interact with the controlled atmosphere in the vacuum chamber (reactive sputtering) and finally condense on the substrates, forming a thin film. The thickness of the film can be tuned simply through the sputtering time, after a proper calibration. Before starting the deposition, a high vacuum ($\sim 10^{-6}$ mbar) is achieved by means of a rotary and a turbomolecular pump, to properly clean the walls of chamber letting them degas adsorbed molecules. Then a controlled flow of Ar gas is pumped into the chamber, bringing the pressure to around $5 \cdot 10^{-3}$ mbar. As can be seen from fig. 3.1

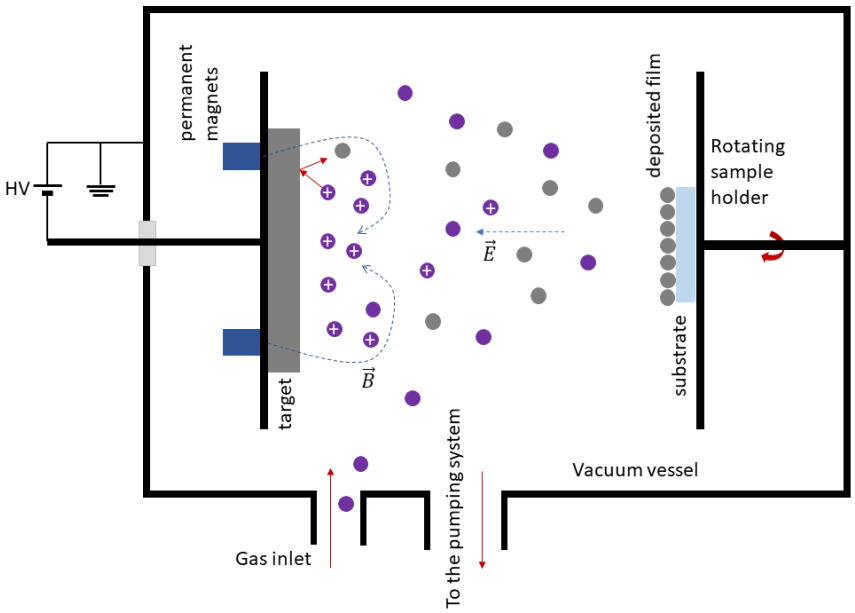

Figure 3.1: Scheme of a magnetron sputtering device. In the situation here depicted there is no interaction between the sputtered ions and the atmosphere of the chamber and the plasma is achieved in DC.

the vacuum chamber is at ground potential and the target is kept at a negative potential in order to accelerate the Ar^+ ions towards it and thus realize the sputtering process. A magnetic field produced by a ring of permanent magnets behind the target helps to confine the plasma close to the target itself, in order to make the erosion process more efficient. On the opposite side of the chamber lies the sample holder on which the substrates are mounted, and, to ensure a more uniform deposition, the sample holder is kept rotating during the deposition. The setup depicted in fig. 3.1 shows a direct current (DC) torch, which is suitable for conductive targets; on the other hand for insulating targets a radiofrequency (RF) torch is used. In both cases the power provided to the torches is kept constant during the deposition.

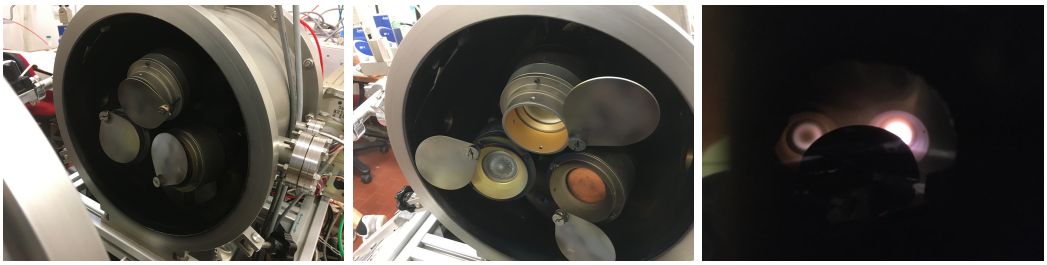

Figure 3.2: Photos of the three torches of the apparatus used for this thesis: with their shutters closed (left) and open (middle). The bottom left torch is a DC one (with an Er target), while the other are RF (the top one has an Al_2O_3 target and the bottom right one a SiO_2 one). The rightmost picture shows the glow of the plasma on the Er torch on the left and the SiO_2 one on the right during the deposition of an Er:SiO_2 layer.

An important remark is that initially the targets are covered by a thin layer of oxide, which could compromise the quality of the deposited films. For this reason every torch is provided with a motorized shutter (fig. 3.2) that, when closed, prevents sputtered particles to reach the sample holder. So, when the torch is initially lit, the shutter is kept close for a 'pre-sputtering' time of a few minutes, allowing to erode away the oxidized layer without the risk of contaminating the samples. Another important feature of the shutter is that it allows to precisely control the deposition time (and hence the thickness of the deposited film), as the torches take a few minutes to be turned on and off.

To deposit oxides, a controlled small amount of oxygen is pumped into the chamber together with the Ar gas. This is crucial for the production of VO_2 since the target is metallic vanadium, but it also helps to keep the right stoichiometry of silica and allumina. In the following table 3.1 are the main deposition conditions for the various layers, and in the last column it is reported the deposition yield ($\mathcal{D}$) in nanometers of material deposited per minute of shutter open. In particular the deposition yield of vanadium is dependent on the potential of the target, which, during the deposition process, oscillates between -450 and $-490\,\mathrm{V}$. Also, when depositing an Er:SiO_2 layer, the ratio of the powers of the erbium torch and the SiO_2 one allows to control the concentration of the Er^{3+} ions. In particulr, with the settings reported in the third row of table 3.1, we obtained an atomic concentration of roughly 0.5%.

Film	Target	Torch	Power [W]	Φ_{Ar} [sccm]	Φ_{O_2} [sccm]	$\mathcal{D}$ [nm/min]
VO_2	V	DC	130	12	$1.2 - 1.3$	$12 - 14$
SiO_2	SiO_2	RF	100	8.6	0	2.5
Er:SiO_2	Er + SiO_2	DC + RF	$3 + 300$	16	0.3	5.3
Al_2O_3	Al_2O_3	RF	75	16	0.3	0.5
Si	Si	DC	100	8.6	0	6.0

Table 3.1: Deposition conditions for the various film materials. Φ_{Ar} and Φ_{O_2} are the fluxes of oxygen and argon injected into the vacuum chamber.

3.1.3 Annealing techniques

As said before, the layers deposited via magnetron sputtering are in an amorphous phase, which is an issue for vanadium dioxide, since we want to observe the transition between two crystalline phases (monoclinic and tetragonal). Moreover, using the Rutherford Backscattering technique (section 3.2.4) we measured that the as-deposited VO_2 is actually VO_x with x ranging between 1.7 and 1.9. Thus the annealing process is also needed to provide the missing oxygen to the layer. The post-deposition annealing could be avoided by having a heated sample holder (at 400 °C in [37] and at 200 °C in [38]) in the sputtering chamber, but our apparatus does not support this option.

Another reason why the post-deposition annealing is needed is that, in order to observe the photoluminescence of erbium, the Er^{3+} ions need to be in ordered octahedral coordina-

tion with the oxygen atoms of the silica matrix, and this can be achieved by bringing the samples at 850 °C. Moreover, the Er^{3+} emission is strongly affected by adsorption of OH^- molecules into the silica layer, which act as quenchers of the photoluminescence. For this reason every time we deposited an Er:SiO_2 layer, we covered it with a few nanometers of allumina, which is impermeable to OH^- molecules and thus protects the layers underneath.

In our labs, we have two main ways to perform the annealing: either in the oven, or with a special component of the X-ray diffractometer, which allows to monitor the evolution of the crystalline structure of the sample during the annealing.

Oven The oven we use is a *GERO D-75242 Neuhausen* that allows to heat samples up to 1300 °C either in vacuum or by injecting a controlled amount of Ar, O_2, N_2 or H_2 gasses. The annealing cycle for activating the Er^{3+} ions is well established and consists of an annealing in vacuum ($\sim 10^{-5}$ mbar) at 850 °C for 2 hours. On the other hand for this thesis it was necessary to find the proper annealing conditions for the VO_2 layers, so we tried both in vacuum and under nitrogen flux, at various temperatures and for different times.

Diffractometer Our X-ray diffractometer has an *Anton Paar DHS900 (AP)* device that consists of a small chamber, into which nitrogen gas is fluxed, which allows to set the sample temperature up to 800 °C, all whilst acquiring diffraction spectra. The obvious advantage of this device is that it allows to monitor the crystalline structure of the sample, but on the other hand the sample is kept in place by two harmonic steel clips (fig. 3.3 middle), which can induce stress on the deposited film. or leave dirt on its surface. Moreover, there is no sophisticated control of the atmosphere inside the annealing chamber. For these reasons the samples annealed in this way usually display some stains around the contact points with the clips (fig. 3.3 right). This is not an issue for the annealing in the oven, where the samples lay horizontal on a silicon wafer inside a quartz slot (fig. 3.3 left).

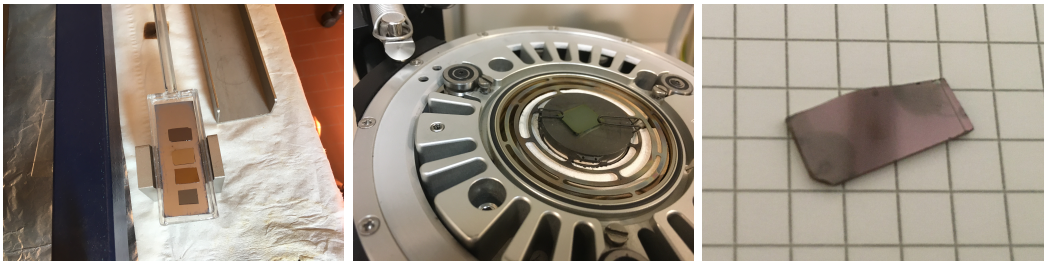

Figure 3.3: Photos of some samples on the quartz slot of the oven (left), of a sample held in place by the clips of the diffractometer (middle), and of the stains left by the before mentioned clips on a sample surface (right).

3.2 Characterization

Let us now move to describing the instruments and techniques for characterizing the samples.

3.2.1 Profilometer

The first property we want to know about the deposited thin film is its thickness. For this reason when doing a deposition we put, together with the other substrates, a reference sample, which is a small piece of silicon wafer over which we draw a line with a permanent marker. After the deposition the reference sample is then sonicated or gently rubbed with ethanol, that dissolves the marker ink, removing also the material that was deposited above it. This way we basically dug a trench on top of the sample that is as deep as the deposited film is thick, which allows us to easily measure the film thickness. One should notice that with this method, if the deposition consisted of multiple layers (e.g. SiO_2 + VO_2), the measured thickness will be the total one. Thus, another approach is to make a scratch on the sample surface with titanium tweezers after the deposition: as titanium is softer than the deposited silica, only the top VO_2 layer will be removed, allowing to measure its thickness alone.

The easiest way to measure a thickness is by using a profilometer, which essentially drags a stylus on top of the sample applying a set force (usually $1 - 5$ mg equivalent) by means of a torque spring. To keep the force constant the system moves the stylus vertically and the displacement is a measure of the height of the sample in that point. The difference in height between the outside and the inside of the trench is an estimate of the film thickness. The profilometer we used is a *KLA Tencor P-17* which has a numerical precision of 1 Å, but an effective one of a few nanometers.

3.2.2 Atomic Force Microscope

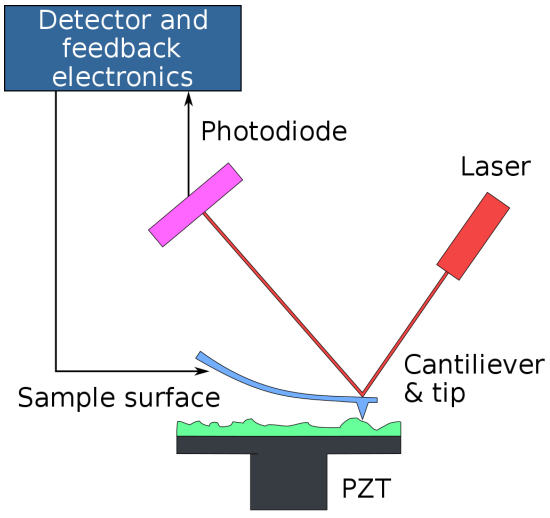

Figure 3.4: Schematics of an AFM [39].

A more sophisticated and precise way to measure film thicknesses is by means of an Atomic Force Microscope (AFM), which consists of a nanometric metallic tip at the end of a cantiliever that is kept vibrating at a resonance frequency around 150 kHz by a piezoelectric actuator, which also measures the amplitude of the oscillation. A laser is shone on the back of the tip and the reflection is collected by four photodiodes and, comparing the intensity reaching each one of them, the system is able to tell the position of the reflected beam and hence deduce the deformation of the cantiliever (fig. 3.4). For this thesis, our AFM (an *NT-MDT Solver Pro AFM*) is operated in semi-contact mode, namely the tip is brought in close proximity of the sample surface but without touching it. There, Van der Waals forces between the tip and the sample alter the resonance of the tip, reducing its oscillation am-

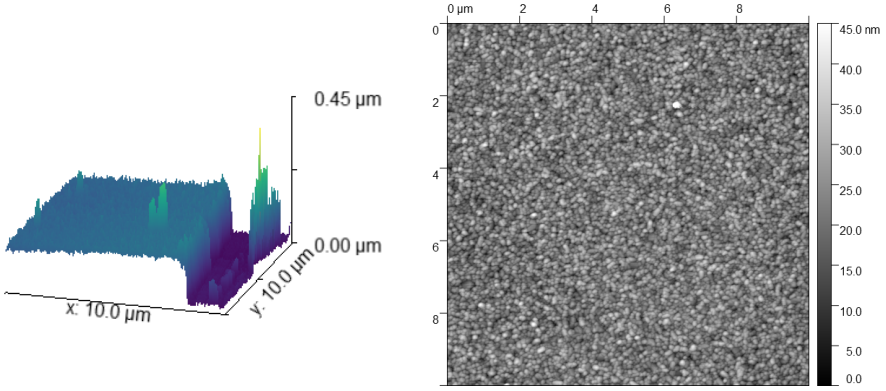

Figure 3.5: 3D visualization of AFM measurements on the edge of a trench for thickness measurements (left) and example of surface roughness of VO_2 grains (right).

plitude. As the tip moves on top of the sample an electronic feedback system moves the sample holder along the vertical axis in order to keep the oscillation amplitude at a given setpoint and the reflected laser beam in the center of the photodiodes. Similarly to the profilometer, this vertical displacement is a measure of the height of the sample in that particular point.

The advantage of using an AFM over a profilometer, besides the higher precision, is that the AFM can perform 2D scans pretty quickly and with high resolution, which allows not only to measure the thickness by scanning around the edge of a trench (fig. 3.5 left), but also to quantify the roughness of the sample surface (fig. 3.5 right). Amongst the many ways to quantify surface roughness, in this thesis I will use only the mean square deviation from the mean plane (R_{ms}), which is easily computable analyzing the images with the *Gwyddion* software [40].

3.2.3 Scanning Electron Microscope

The AFM allows to measure the surface roughness of a sample, but the horizontal resolution is around 10 nm, which results in the topographic images looking quite blurry. To overcome this barrier and obtain a high resolution morphological image that allows to clearly see the single crystalline grains, one has to resort to more sophisticated apparati, like a Scanning Electron Microscope (SEM).

The SEM used for this work (a *Zeiss Sigma HD field-emission microscope*, fig. 3.6) uses a field effect electron gun and a condensor to produce a high energy electron beam inside a high vacuum ($\sim 10^{-9}$ mbar) chamber. The electrons are then decelerated (usually down to $1-10$ keV for this thesis) and focused on the sample surface, where they interact in different ways (elastic and anelastic collisions, generations of X-rays...). What we are particularly interested in are the elastically backscattered electrons and the secondary electrons: since the impinging beam was decelerating before reaching the sample, this means that those electrons are accelerated back into the microscope objective and reach the *InLens* detector, where the collected current gives informations about the morphology

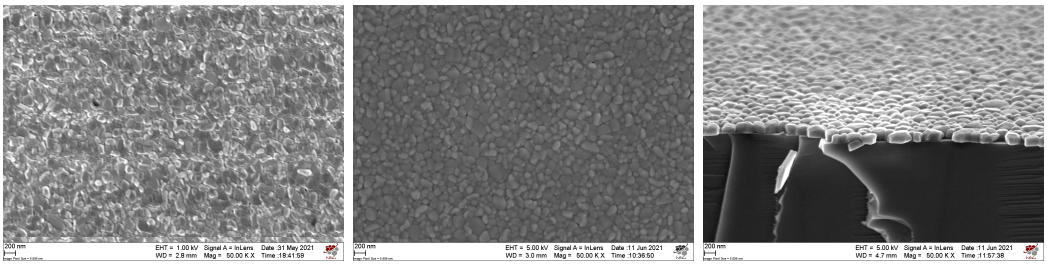

Figure 3.7: SEM images at 50000 magnifications of VO_2 grains. Left and center images are the same sample (SiO_2 substrate) viewed respectively without and with the carbon tape. On the right a cross section view of the grains on top of a Si substrate.

of the sample (secondary electrons) and its chemical composition (backscattered electrons). Towards the tip of the microscope objective are the scanning coils, which allow to steer the beam on the surface of the sample and thus create a 2D image.

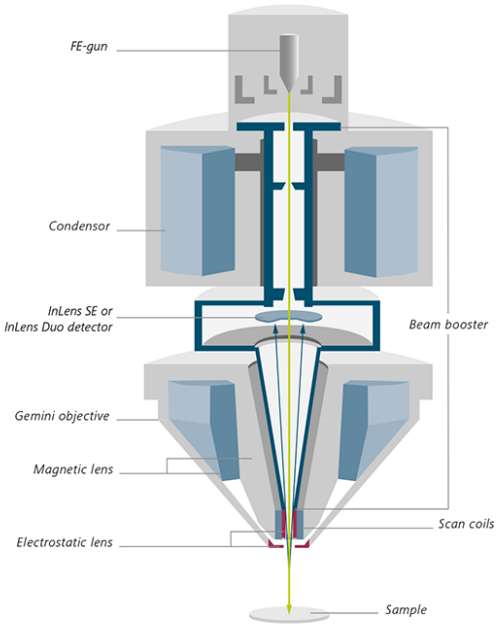

Figure 3.6: Schematics of the *Gemini Column* of the SEM used in this thesis [41].

The energy of the incident beam is an important parameter as higher values yield a better resolution on the image, but can also give rise to charging effects, namely electrons get trapped on the sample surface under the beam spot, and the build up in charge affects the newcoming electrons. The consequence is that, since this is a dynamic process, the image drifts or goes out of focus. To avoid this unpleasant phenomenon it is important to quickly drain the excess electrons from the sample, which is not a problem if the substrate is conductive (e.g. silicon). On silica substrates, on the other hand, a nice trick is to attach a small piece of conductive carbon tape to the surface of the sample and connect the other end of the tape to the metallic sample holder (fig. 3.7 left and center).

With a SEM one can not only image the surface of the sample, but also view it in cross section (fig. 3.7 right). This is achieved by breaking a piece of the sample and looking at the fracture under the electron beam, with the surface forming an angle of roughly 15 degrees with respect to the beam. This allows to better understand the shape of the crystalline grains, their adhesion to the layers below and can also be used as an alternative (but quite imprecise) way of measuring the film thickness.

A more quantitative analysis of the SEM images can be performed with the *ImageJ* software [42] and in particular the *MorphoLibJ* plugin [43] which allows to perform a mor-

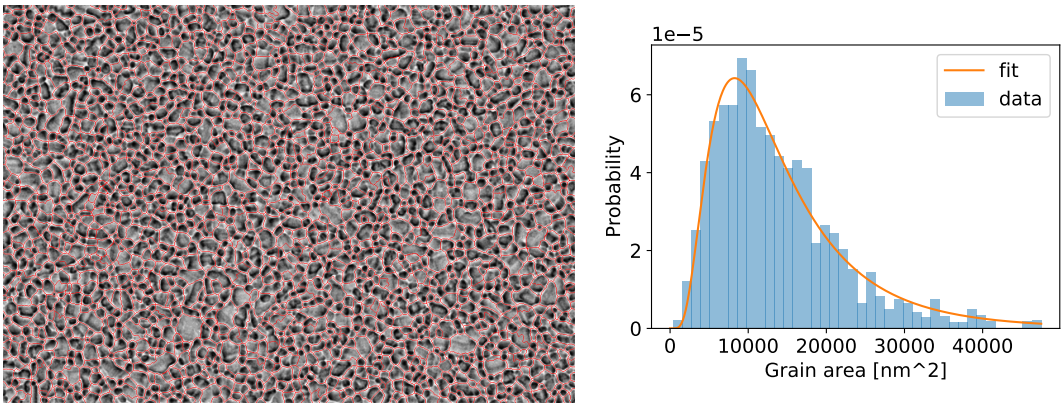

Figure 3.8: SEM image of a VO_2 thin film with overlayed grain borders computed by *MorphoLibJ* and lognormal fit of the histogram of the grain area

phological segmentation of the images highlighting the grain boundaries and thus allowing to gather statistics of the grain size (fig. 3.8). In particular, the output of the analysis of the images will be a list of grain areas $\{A_i\}_{i=1}^N$. One could then build a simple normalized histogram where the probability of the grain area being between A and $A + dA$ is simply

$$\mathcal{P}(A) = \frac{1}{N}\sum_{i=1}^{N} \chi_{[A,A+dA]}(A_i) \quad \chi_{[A,A+dA]}(x) = \begin{cases} 1 & \text{if } x \in [A, A+dA] \\ 0 & \text{otherwise} \end{cases} \tag{3.1}$$

Where χ is the indicatrix function and dA the bin width of the histogram. However this result would be biased towards the smaller grains, since they are far more common. On the other hand we are interested in the probability of being in a grain of area between A and $A + dA$ when picking a random point on the sample surface, which can be estimated as

$$\mathcal{P}(A) = \frac{\sum_{i=1}^{N} A_i \chi_{[A,A+dA]}(A_i)}{\sum_{i=1}^{N} A_i} \tag{3.2}$$

This histogram can then be fitted by a lognormal distribution.

$$\mathcal{L}(x;\mu,\sigma) = \frac{1}{\sigma\sqrt{2\pi}x}\exp\left(\frac{(\ln x - \mu)^2}{2\sigma^2}\right) \tag{3.3}$$

At this point if a is a random variable with mean μ and standard deviation σ (which represents the logarithm of the grain area), we can define the effective diameter of the grains as

$$\phi_{eff} = 2\sqrt{\frac{e^a}{\pi}} \tag{3.4}$$

3.2.4 Rutherford Backscattering

Rutherford Backscattering (RBS) is an experimental technique that allows to measure the chemical composition of a sample as a function of depth from its surface. It works by accelerating light ions (α particles in our case) at high energy towards the sample surface and then collect the backscattered ions and measure their energy [44]. The energy of the

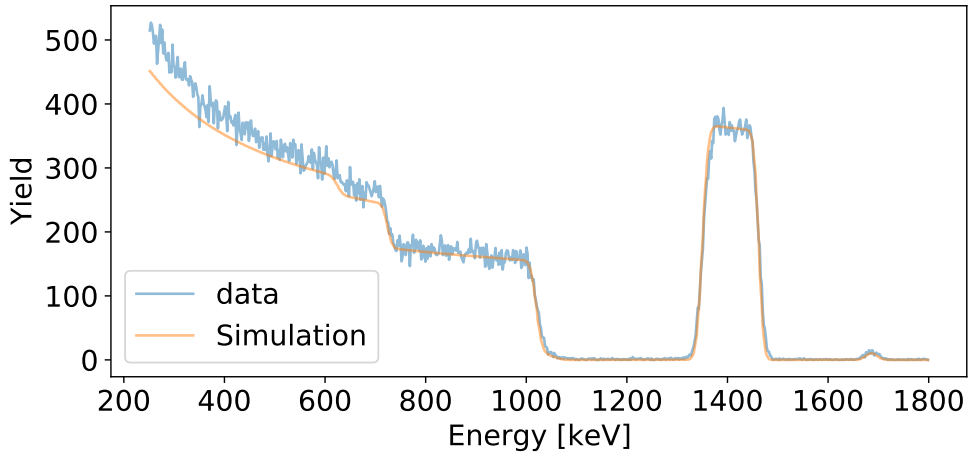

Figure 3.9: Example of data and simulation of an RBS spectrum on a sample with a VO_2 layer on top of an Er:SiO_2 layer on top of bulk SiO_2. From right to left it is possible to see the small peak due to Er ions, then the box-like peak of V and at lower energy the O bump on the Si background.

collected ions depends on which atom they performed backscattering with (the lower the target atom mass the lower the energy of the backscattered ion) and also on how deep in the sample the scattering event happened: the deeper the event the lower the collected energy, since the ion has to pass through a larger amount of material and hence loses more energy. One then creates a model of the multilayered sample and uses tabulated stopping powers for the elements in it to simulate an energy spectrum that will be compared with the experimental one (fig. 3.9). The apparatus used for this thesis is the Van de Graaf accelerator AN2000 at *Laboratori Nazionali di Legnaro*, which produces a continuous beam of α particles at 2.2 MeV and the software used for simulating the RBS spectra is *WinRobot*, which was developed by our department.

As can be seen from fig. 3.9, the simulation is not completely able to fit the data, and, in particular, to better fit the vanadium peak the stoichiometry needed for the VO_x layer is with $x \sim 1.5$, while if one focuses on the oxygen peak, this time $x \sim 2$. This is a problem that we encountered in every sample, and severely hindered the reliability of measurements of this kind. A possible way to solve this issue is calibrating the apparatus on certified stoichiometric VO_2, which will be done, but not in time for this thesis.

3.2.5 Grazing Incidence X-Ray Diffraction

The easiest and most effective technique for characterizing a crystalline phase is the use of X-ray diffraction, and in particular, to focus only on the surface of the sample (i.e. the thin films deposited on the substrate), one can use Grazing Incidence X-Ray Diffraction (GIXRD). In this geometry (fig. 3.10) the X-ray beam impinges on the sample surface with a small incidence angle $\omega = 0.5°$ and interacts with the crystallographic planes, according

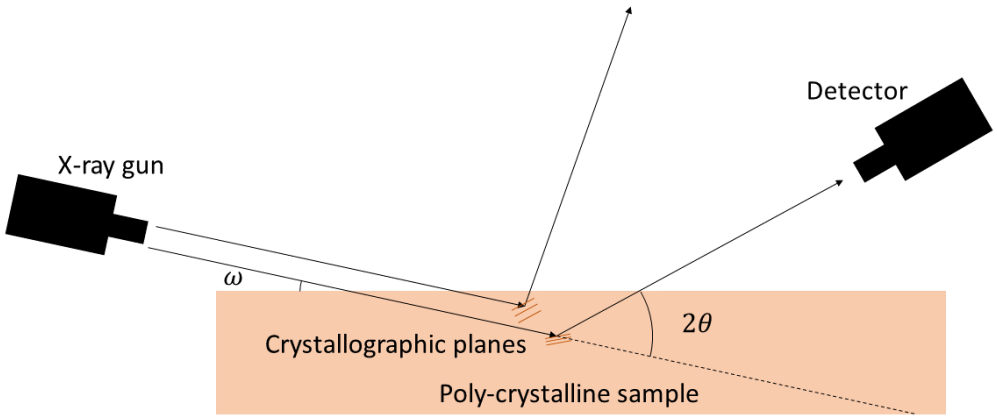

Figure 3.10: Schematics of the GIXRD geometry.

to the Bragg law, generating diffraction peaks at deflection angles 2θ such as

$$2d_{hkl}\sin\theta = n\lambda \tag{3.5}$$

where d_{hkl} is the distance between the crystallographic planes with Miller indices hkl, λ is the wavelength of the X-rays and n is an integer. From the positions of the peaks it is then possible to identify the crystal.

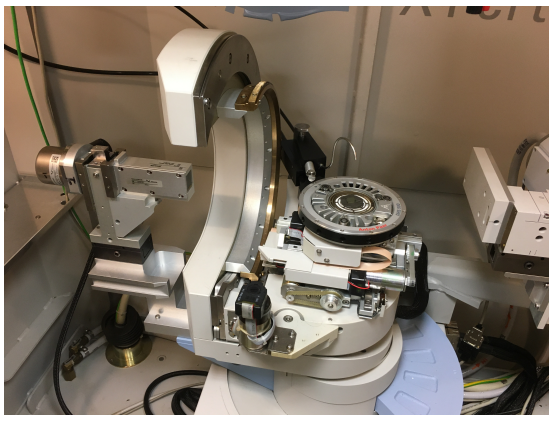

Figure 3.11: The diffractometer used in this thesis: from right to left we can see the X-ray source, the 6 degrees of freedom sample holder and the detector.

With this geometry it is possible to see all the peaks only under the assumption of the sample being polycrystalline, namely composed of relatively small crystalline grains with random orientation, which means that for every theoretical θ that should produce a diffraction peak, there are some grains that have their crystallographic planes forming an angle θ with the incident X-ray beam in the plane containing also the detector.

Another important effect of the sample being polycrystalline is the size broadening of the peaks. The Full Width at Half Maximum (FWHM) β of a peak in a 2θ spectrum expressed in radians is given by the Debye-Scherrer formula:

$$\beta = \beta_{inst} + K\frac{\lambda}{D\cos\theta} \tag{3.6}$$

where β_{inst} is the instrumental broadening, K is an adimensional constant dependent on

the shape of the crystallites (in the assumption of spherical shape $K = 0.89$) and D is the diameter of the crystallites. Thanks to eq. (3.6) it is then possible to estimate the size of the grains from the diffraction spectra.

The instrument used in this thesis is a *Panalytical X'Pert Pro* diffractometer (fig. 3.11) that uses the X-rays of the copper K-α emission line ($\lambda = 0.15406\,\text{nm}$) and has an instrumental broadening $\beta_{inst} = 0.27°$. This instrument can use either a sample holder that allows to take measurements on multiple samples but only at room temperature or the already mentioned *Anton Paar DHS900* which allows to perform measurements on a single sample but varying the temperature, which is monitored by means of a thermocouple.

3.2.6 Spectrophotometry

An instrument used intensively in this thesis is the *JASCO V-670 UV-Vis-NIR* spectrophotometer, which allows to collect transmittance spectra of a sample. It works by having a series of lamps and gratings that allow to select a specific wavelength of light (I worked in the range 400-2000 nm). The beam is then split and one of the beams travels through the sample, while the other goes through a reference channel (air for this thesis). The transmittance is then computed by comparing the collected intensity of the two beams, which allows to compensate for possible fluctuations in the intensity of the light source. One of the possible sample holders is a heated cell (fig. 3.12) connected to a temperature

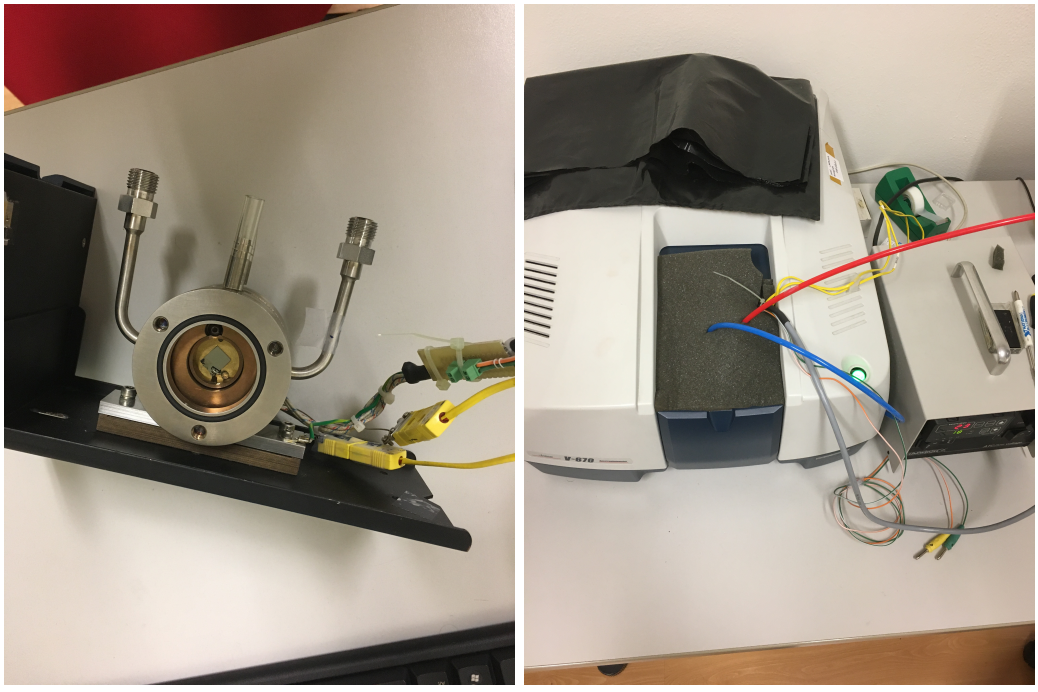

Figure 3.12: Heated sample holder (left) and experimental setup with the JASCO spectrophotometer on the left, the temperature controller on its right and the red and blue compressed air pipes (right).

controller which uses compressed air as a cooling force, and allows to take transmittance spectra as a function of temperature. The measurement of the transmittance can be used

to obtain insight on the dielectric function of the VO_2 , but is also a very powerful tool for quickly visualizing the phase transition of the VO_2.

Automation Before my work the controls on the spectrophotometer and on the temperature controller were manual and disconnected from one another, which meant that to acquire an hysteresis cycle on a VO_2 sample, one had to press a button roughly every five minutes: either to change the temperature, start a measurement or save the data. Also one had to constantly keep an eye on the temperature controller to wait for the convergence to the desired setpoint. Considering that a single hysteresis cycle takes around 10 hours, the user had to lose a lot of time performing really dull tasks. So, after spending five full days taking measurements in such an inefficient way, I decided to automate the process by writing a Python code. Now one has simply to prepare the setup and schedule the list of temperatures at which spectra need to be taken (process which takes at most one hour), and then the system runs without the need of human supervision. With this improvement it is thus possible to better exploit the potential of this instrument, also for future works.

3.2.7 Ellipsometry

If the transmittance can give hints on the dielectric function of the material, the best technique to properly measure it is ellipsometry. It works by comparing the reflectance in the two polarizations: Transverse Electric (TE or s) and Transverse Magnetic (TM or p). In practice if r_s and r_p are the two Fresnel coefficients, the system measures their ratio ρ, which is then expressed in terms of the real variables Ψ and Δ:

$$\rho = \frac{r_p}{r_s} = \tan\Psi e^{i\Delta} \tag{3.7}$$

In the instrument used for this thesis (a *J.A. Wollam VASE*), this is achieved by having a polarizer and a retarder that produce an elliptically polarized light impinging on the sample. The reflected light is collected by a detector after passing through a continuously rotating analyzer (fig. 3.13). The time dependent profile of the intensity collected is sinusoidal with frequency equal to the one of the rotating analyzer and amplitude and phase which are functions of ρ. Moreover the light source is made of a series of lamps and some gratings that, similarly the spectrophotometer, allow to select a single wavelength. Also the system is able to acquire measurements at different angle of incidence θ, hence its name *Variable Angle Spectroscopic Ellipsometer (VASE).*

We acquired data with wavelengths between 300 and 1700 nm and at three different angles ($\theta = 55, 60, 65$ degrees), all close to Brewster's angle, such as to maximize the contrast between r_p and r_s and hence the quality of the ellipsometric measurements.

One has to observe that ellipsometry is not a direct measurement of the dielectric function of the material. Instead one has to create a parametric model of the multilayered sample, simulate the theoretical Ψ and Δ, and then fit the model parameters to the experimental data. For this purpose I used the *WVASE32* software, that was provided together with the ellipsometer.

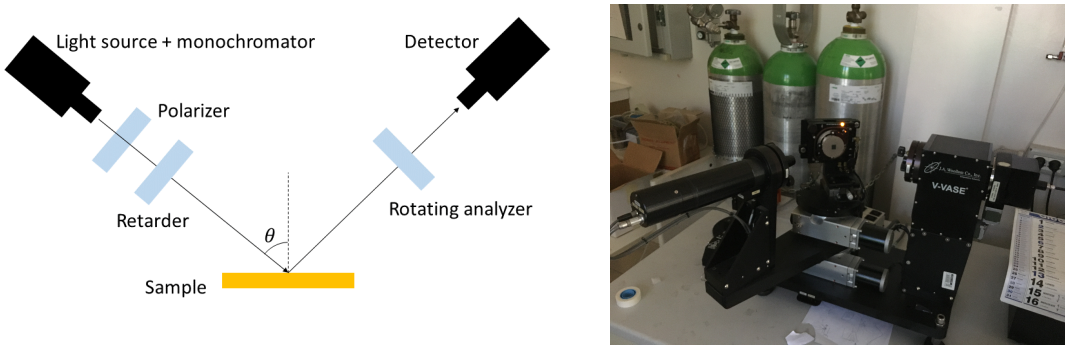

Figure 3.13: Schematics of an ellipsometric measurement (left) and photo of the ellipsometer used (right).

This fitting process can be quite tricky, since there are a lot of parameters for the model (thickness of the layers, surface roughness, enclosures of one material into another...) and the final results of the dielectric functions can vary a lot. So, to stabilize the fits, we fitted the transmittance data acquired at the spectrophotometer together with the ellipsometric data.

3.2.8 Photoluminescence

All the characterization techniques described so far were used to measure properties of the VO_2 films alone. This last one instead is the only one that allows to measure the emission properties of the Er^{3+} quantum emitters. Following the schemes and pictures of fig. 3.14, the pump laser is a continuous wave 520 nm green diode laser which is resonant with the ${}^4I_{15/2} \rightarrow {}^2H_{11/2}$ absorption line of the Er^{3+} ions (fig. 1.1). The excited state ${}^2H_{11/2}$ then quickly decays through a series of non-radiative processes to the metastable ${}^4I_{13/2}$ level and then finally back to the ${}^4I_{15/2}$ ground state emitting photoluminescent light at 1540 nm. The pump laser is initially focused on a mechanical chopper, which allows to produce an effective pulsed beam. Then, the beam reaches the sample that is glued by means of carbon tape to a silicon wafer, which is glued to the copper tip of a cryostat (fig. 3.14 bottom right). The usage of silicon and carbon tape ensures a good thermal contact between the parts. The cryostat is provided with a heater and a thermocouple fixed near the sample.

It is also possible to connect a turbomolecular pump to the cryostat and hence create high vacuum ($\sim 10^{-5}$ mbar) in the chamber with the sample. This has the advantage of protecting the VO_2 layer from exposure to oxygen at high temperature, but means that it is not possible to calibrate the thermocouple of the cryostat in that condition as there is no way of inserting a second thermocouple when the chamber is sealed. For this reason we have to trust the value read from the cryostat, which could be a source of systematic error.

At this point the photoluminescence (PL) photons emitted by the sample are collected by two lenses with high numerical aperture ($NA = 0.26$) and focused into the monochroma-

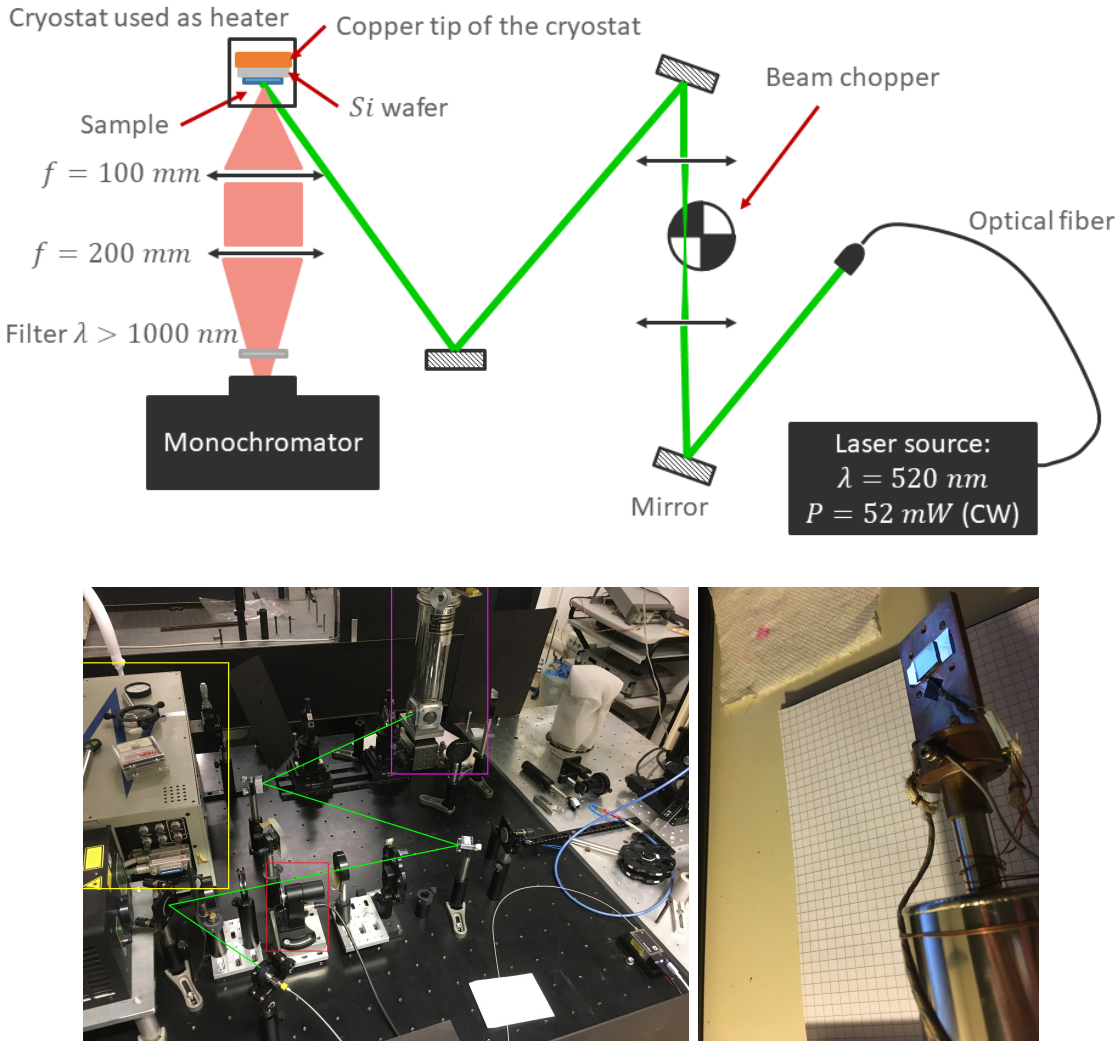

Figure 3.14: Schematics (top) and photos (bottom) of the photoluminescence setup. In green it is highlighted the pump laser path, in purple the cryostat, in red the chopper and in yellow the monochromator.

tor, where a filter cutting wavelengths less than 1000 nm prevents scattered pump photons from entering it. Inside the monochromator, gratings select a single wavelength and then the photons reach a photomultiplier tube detector cooled with liquid N_2. The signal from the detector is then sent either to a digital oscilloscope for time-resolved measurements or to a lock-in amplifier that uses the chopper signal as reference for collecting PL spectra.

To avoid being in resonance with the power supply at 50 Hz, the chopper frequencies were chosen to be prime numbers, in particular we worked at 7, 13 and 29 Hz. Another remark is that the monochromator is provided with slits and, by tightening them, less wavelengths are able to pass through and so the spectral resolution is higher but the signal intensity is lower. For this work the slits were always as open as possible, since it was more important to have higher signal intensity for better time-resolved measurements rather

than a high resolution in wavelength.

It is also important to point out that the characteristic decay time of the intensity measured with this setup is not just the radiative decay, but also accounts for any non-radiative decays. Instead the intensity of the signal is directly proportional to the decay rate of the collected photons (see eq. (2.5)).

Chapter 4

VO_2 thin films

Before diving into the details of the results, a quick note on how the samples are named. Each sample is denoted as *<deposition>_<sample name>*, where the sample name is usually an id and the substrate of the sample (e.g. D2871_03Si). Whenever a sample is split in two, the two parts are identified by adding a *_1o2* (1 of 2) or a *_2o2* (2 of 2) to the sample name before the splitting. If the sample is then split again another suffix will be added, for instance D2871_02SiO2_2o2_1o2.

As said in section 3.1.2 the deposition by magnetron sputtering with a cold sample holder yields an amorphous structure for the deposited film and so a post-deposition annealing is needed. The annealing causes the formation of crystalline grains, well visible in the cross section SEM image in fig. 4.1) which is detectable also by the AFM as an increased surface roughness. Moreover the transition from an amorphous to a polycrystalline phase changes the optical properties of the sample. For example in the last panel of fig. 4.1 we can see how the spectrum of the as-deposited amorphous sample (blue and red curves) is quite different from the characteristic one of monoclinic VO_2 (purple curve), which features a high absorbance towards the blue end of the spectrum. The red and orange curves instead represent spurious phases that arise when the annealing process doesn't last long enough (more on that later).

4.1 VO_x phases

The phase diagram of vanadium oxides VO_x is very rich in phases, as can be seen from fig. 4.2, but the most common are V_2O_3, VO_2 and V_2O_5. To discriminate the phases an effective technique is the Rutherford Backscattering (RBS) one. However, as described in section 3.2.4, the simulations of RBS spectra were not able to describe the data well enough to obtain an accurate estimate of the stoichiometry of the samples. For this reason the best way we had to identify the phases was from the analysis of Grazing Incidence X-Ray Diffraction (GIXRD) diffraction peaks. One should however notice that while the RBS technique measures the stoichiometry of the whole sample, GIXRD detects only the crystalline part, ignoring amorphous portions of the sample.

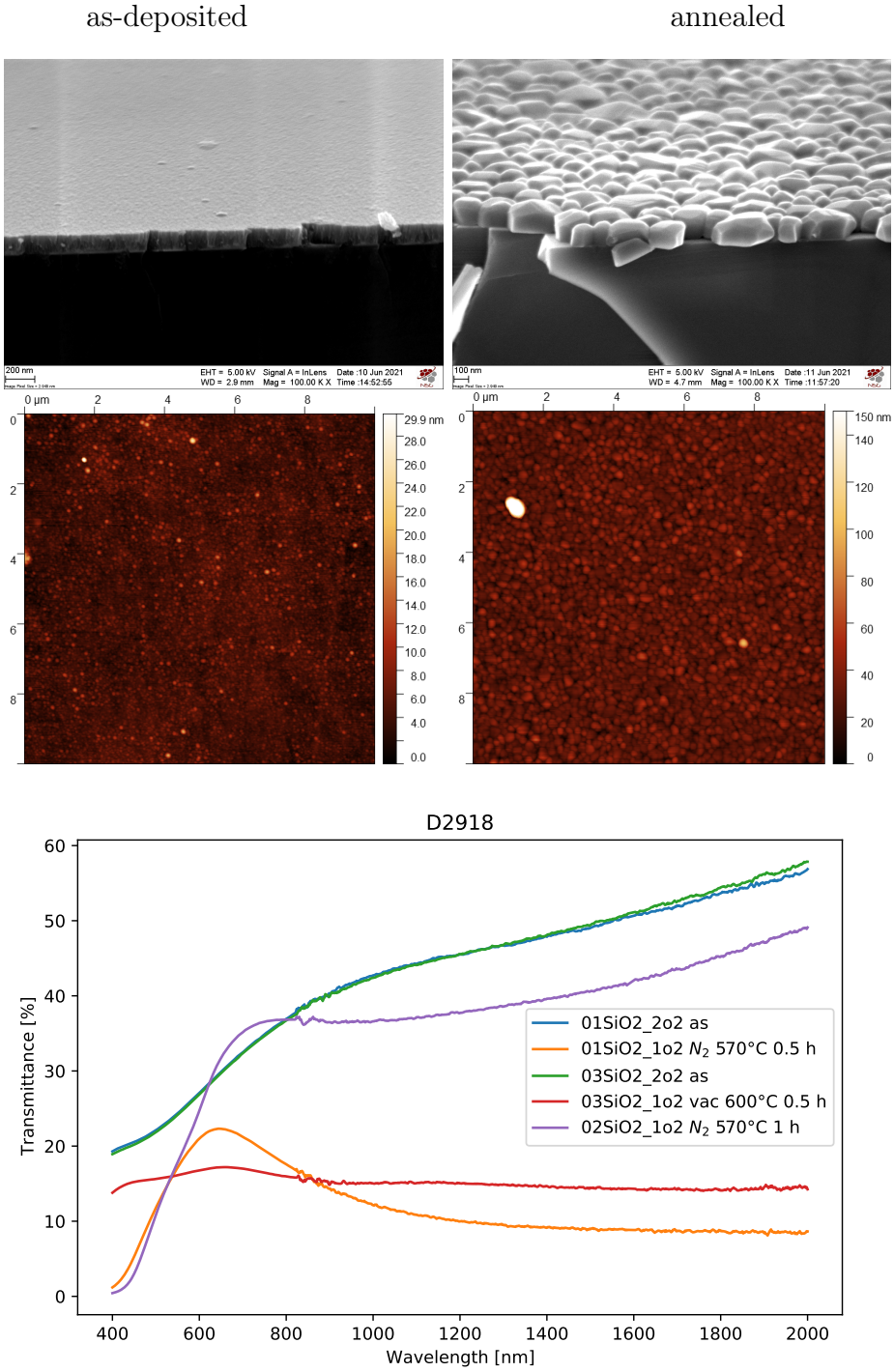

Figure 4.1: Effect of the annealing on the surface of the sample seen at the SEM in cross section (top) and at the AFM (middle), where the surface roughness changes from 1.2 to 7.9 nm. On the bottom plot are the transmittance spectra of as-deposited samples and ones annealed in different conditions.

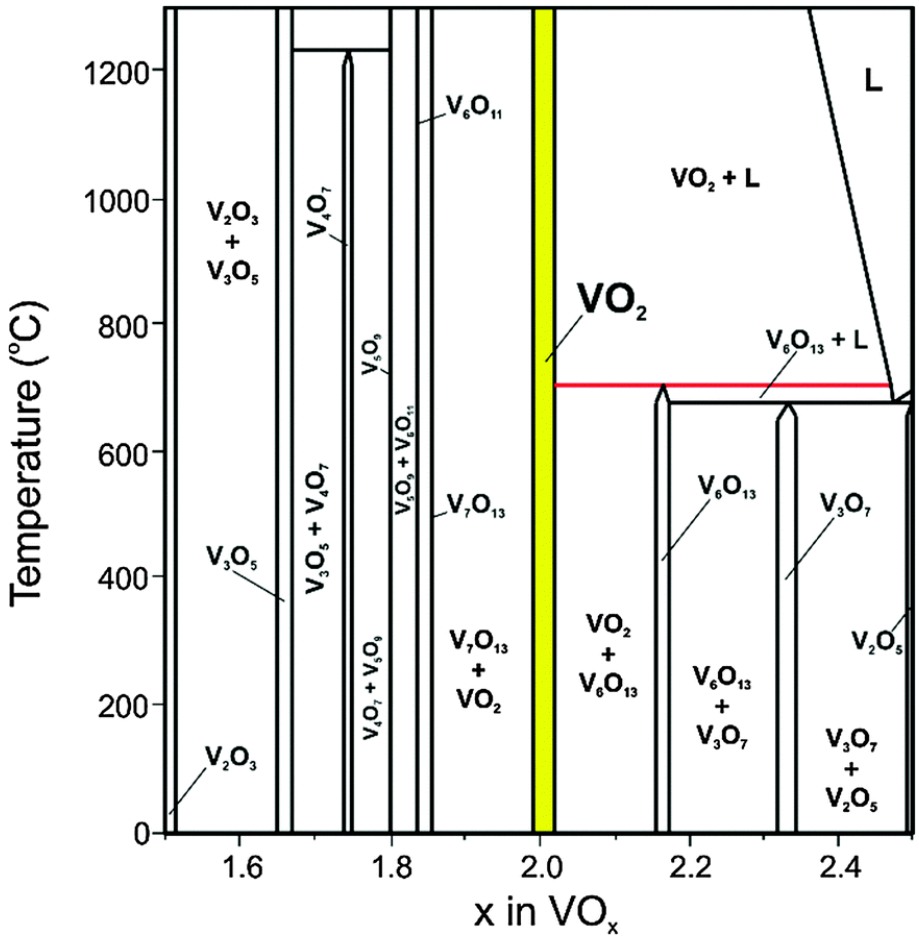

Figure 4.2: Phase diagram of the different vanadium oxides [45].

In this thesis the only two oxides we observed are VO_2 and V_2O_3, and in fig. 4.3 we can see an example of the characteristic GIXRD peaks of this two phases. In particular on the left are the ones of VO_2 at room temperature when it is in its monoclinic (M1) state and at high temperature when it is in the tetragonal (R) one. On the right instead we can see the characteristic spectrum of V_2O_3. In both cases the peaks sit on top of a smoothly changing background which is due to the silica substrate.

The peaks shown in the right panel of fig. 4.3 are the ones that we observed in most of the VO_2 samples, however, a perfectly polycrystalline sample would display more peaks and in some samples we observed some of them (one at 37 and the other at 42 degrees). This could be the symptom that the grain orientation is not isotropic and there are preferred directions of growth, as said in section 3.2.5 .

4.2 Kinetics of the annealing at the diffractometer

If the spectra with 2θ ranging between 20 and 60 degrees (fig. 4.3) are very useful for recognizing the phase, they are quite long measurements to take, requiring a little less than two hours. On the other hand, if we look just at the most intense peak of VO_2 located at

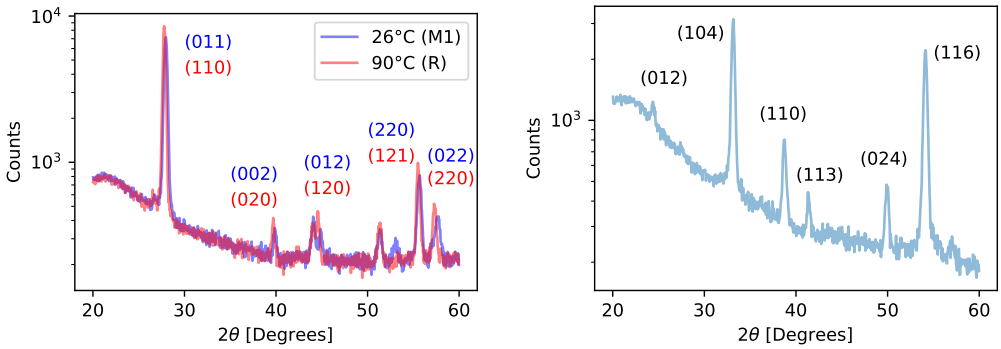

Figure 4.3: GIXRD spectra of VO_2 (left) and V_2O_3 (right) measured on 135 nm thick films on top of a silica substrate. The Miller indices of the peaks were taken from [46] and [47] for VO_2 and V_2O_3 respectively.

$2\theta = 28$ degrees by performing, for example, a scan with $2\theta \in [20°, 30°]$, the time required to complete a measurement drops to roughly 7 minutes. This allows us to monitor the evolution of the peak over time during an annealing process or an hysteresis cycle.

The peak can then be fitted with a Pseudo-Voigt function

$$f_{PV}(x; A, \mu, \sigma, \alpha) = A\left(\alpha\frac{\sigma/\pi}{(x-\mu)^2+\sigma^2} + (1-\alpha)\frac{1}{\sigma_g\sqrt{2\pi}}\exp\left(-\frac{(x-\mu)^2}{2\sigma_g^2}\right)\right) \tag{4.1}$$

where $\sigma_g = \sigma/\sqrt{2\ln 2}$, in such a way that the Full Width at Half Maximum (FWHM) of the Gaussian, Lorentzian and total peak is equal to 2σ. In this range of angles (or even better if $2\theta \in [25°, 30°]$) the background due to the silica substrate can be approximated as linear, so the function used to fit the data is

$$f(x; A, \mu, \sigma, \alpha, a, b) = f_{PV}(x; A, \mu, \sigma, \alpha) + a + bx \tag{4.2}$$

and an example can be seen in the right panel of fig. 4.4.

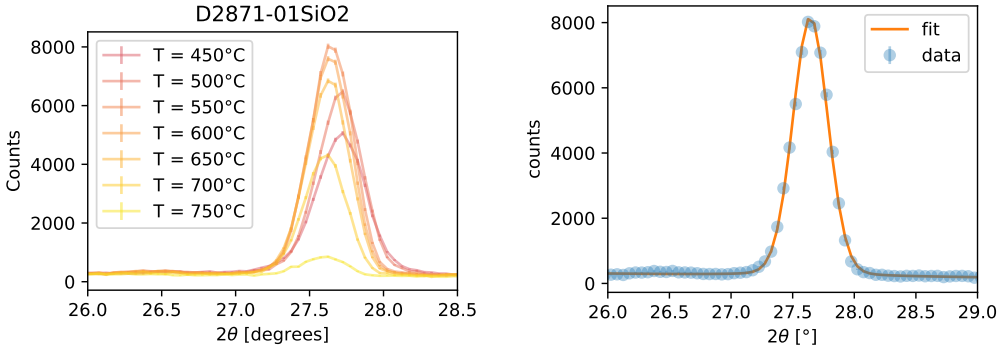

Figure 4.4: Growth and decay of the VO_2 phase with temperature (left) and example of a Pseudo-Voigt fit on the peak at 500 °C (right).

To follow the evolution of the peak with time and temperature during the annealing process we mounted the samples on the Anton Paar DHS900 (AP) device and scheduled a

series of temperatures from 450 to 750 °C. For every temperature, the sample is measured several times. As an example on the left of fig. 4.4 are reported the peaks of the last spectrum of each batch of measurements at every temperature. However more insight can be inferred from the analysis of the parameters of the Pseudo-Voigt fits.

In particular we can see that there is a growth in the peak amplitude A when the temperature stays below 600 °C, while above such temperature the VO_2 phase starts to deteriorate. The characteristic times of the growth and decay (fig. 4.5 top) are obtained with an exponential fit (eq. (4.3)) of the peak amplitude as a function of time considering that the time interval between consecutive spectra is 7 minutes:

$$A(t; a, b, \tau) = a + b\left(1 - e^{-t/\tau}\right) \tag{4.3}$$

From the bottom left panel of fig. 4.5 we can also notice that the position of the peak μ moves to lower angles as the temperature is increased, and this drift is more evident when the phase is deteriorating.

Another interesting quantity to monitor is the crystallite size, which can be computed from the broadening of the peaks using the Debye-Scherrer formula (eq. (3.6)). From the bottom right panel of fig. 4.5 we can see that during the first part of the annealing the crystallite size increases with time, as expected for a growth process, however it doesn't change much during the decay of the phase. This could be explained with the hypothesis that in the first part of the annealing the grains grew from nucleation centers by absorbing the surrounding amorphous phase. On the other hand, once the grains have consumed all of the amorphous phase and come into contact with one another, a further growth would mean the fusion of adjacent grains. However, this process is more difficult than the previous one, since adjacent grains that grew independently are most likely to have their crystalline planes already formed with different orientations, and so it is quite hard to fuse them into a single grain.

The decay in intensity (fig. 4.5 top) can instead be interpreted considering the VO_x phase diagram (fig. 4.2): as the temperature gets close to 700 °C there can be coexistence of solid and liquid VO_2, which could explain the reduced amplitude of the peak. Also, since the cooling back to room temperature is pretty quick, the liquid phase has no time to crystallize and solidifies into an amorphous state, hence the low amplitude of the last peak at room temperature.

This experiment of monitoring the annealing with GIXRD spectra was performed on samples with two different film thicknesses: 135 and 75 nm and all showed similar results to the ones discussed here. In particular the characteristic time of growth τ shows no dependence with respect to the film thickness, staying in the range between 15 minutes and 1 hour. It needs to be said also that the data don't follow a clear exponential growth/decay, so the uncertainties on the τ values are quite high. However these first measurements were useful as a starting point for choosing the annealing times of the subsequent samples.

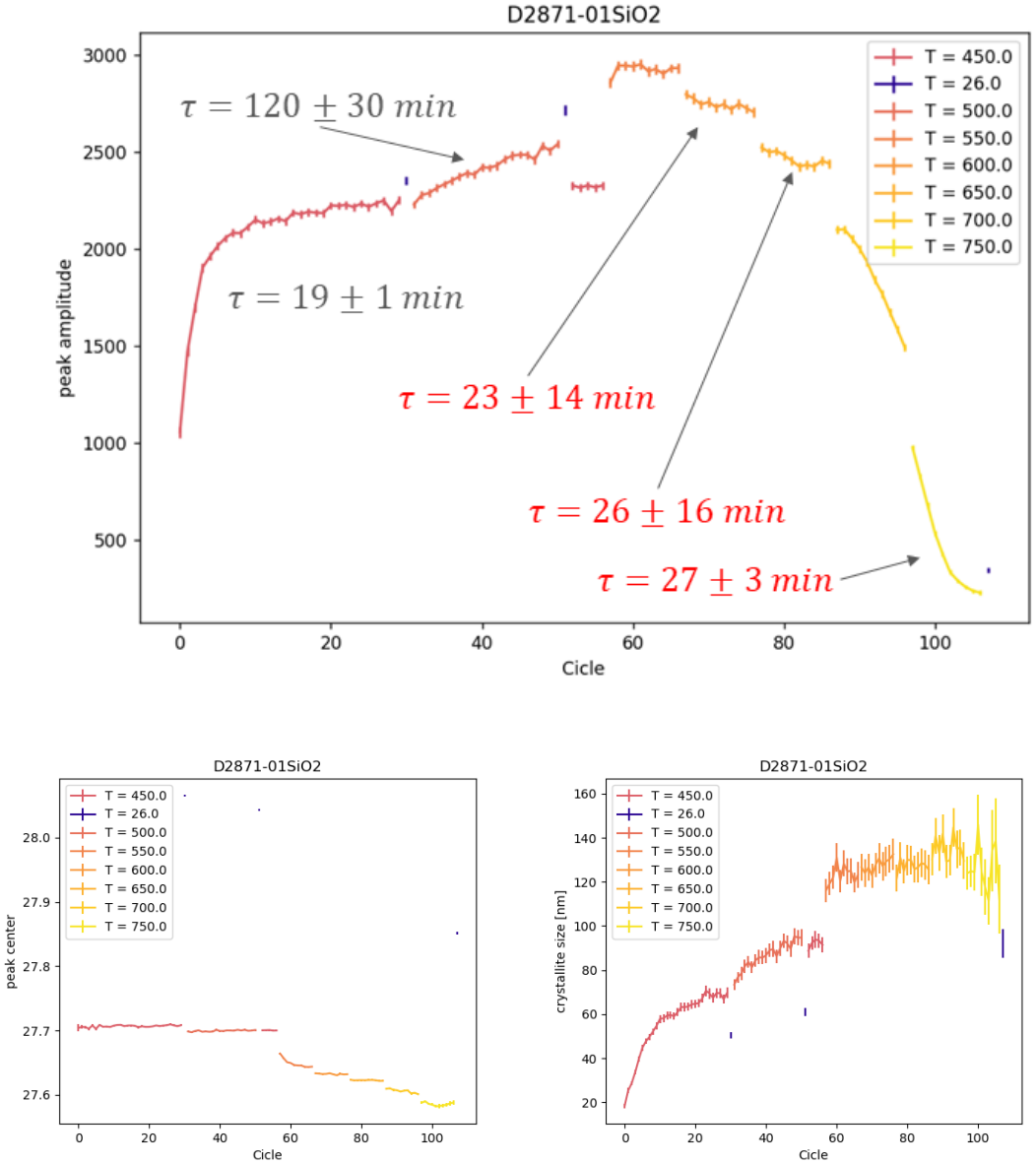

Figure 4.5: Behavior of the peak parameters during the annealing process of a 135 nm thick VO_2 film (the same displayed in fig. 4.4). On the top chart the behavior of the peak amplitude A with the characteristic times of growth (in black) and decay (red) at the different temperatures. On the bottom left is reported the behavior of the peak center μ and on the right the one of the crystallite size. The plot of the peak center gives the first view at the phase transition of VO_2.

4.3 Morphological characterization

If a first estimate of the crystallite size can be obtained from the broadening of the GIXRD peaks (fig. 4.5 bottom right), the best way to characterize this aspect of the sample is via the analysis of the Scanning Electron Microscope (SEM) images, as explained in section 3.2.3. This will give us insight on the horizontal geometry of the sample surface, while the roughness measured at the Atomic Force Microscope (AFM) (section 3.2.2) will tell us about the morphology on the vertical direction.

Focusing on the SEM images, before doing a quantitative analysis, it is possible to qualitatively characterize the surface of the samples by looking at how tightly packed the grains are and hence what is the filling fraction f of the interstitial holes between them. In particular, it is possible to identify 6 categories, following the order of the images in fig. 4.6:

1. *Tightly packed*: the grains are quite small and fill the space well, leaving very few and small gaps ($f < 0.5\%$). This is the ideal situation as it is the closest to a continuous film. To the naked eye the sample is very reflective.

2. *Gravelly*: the grains have a distinct top texture and resemble rocks on the sample surface. Some holes are visible from the top, but probably there are a lot of voids between the grains and the layer underneath (or the substrate). This texture was mostly observed on films that turned out to be V_2O_3.

3. *Small holes*: now there are more gaps between the grains but they are still quite small ($f \sim 5\%$). The surface roughness increases drastically and so the sample looks whitish to the naked eye due to the scattering of light.

4. *Large holes*: similar to previous case, but with bigger holes. The grain borders that face a hole start to be rounded.

5. *Connected nanoparticles*: at this point every grain is mostly surrounded by holes and has rounded edges. In the gaps between the grains it is possible to see the footprints of the grains before the fusion. To the naked eye the sample surface looks rugged.

6. *Nanoparticles*: the filling fraction is over 50% and we can no longer speak of grains, but rather isolated spherical nanoparticles.

From the many samples produced, we deduced that the morphology of the sample has a very strong dependence on the cleanliness of the sample surface: the dirtier the sample the higher the hole filling fraction. For this reason it is very common that a single sample displays many of the above categories, for example by being mostly *tightly packed* with stains of *large holes* where the sample was held by the clips of the AP. This hypothesis is enforced by the fact that samples from the same deposition treated with the same annealing procedure (in the oven) yielded the *tightly packed* structure when cleaned immediately

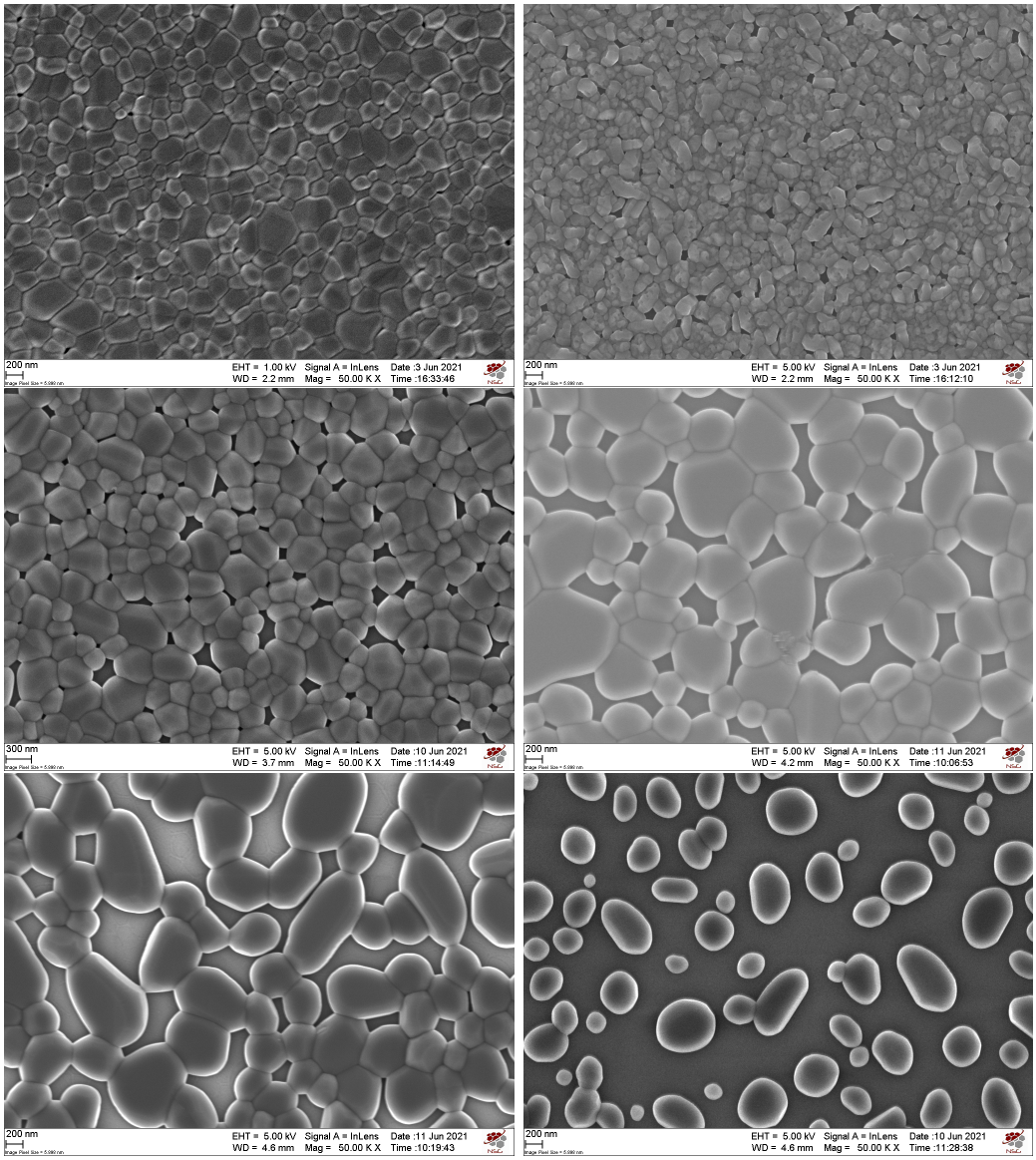

Figure 4.6: SEM image at 50000 magnifications of examples of the qualitative types of grain arrangements. In order: *tightly packed* (D2871_02SiO2_2o2_1o2, $f = 0.2\%$), *gravelly* (D2891_01Si, $f = 2\%$), *small holes* (D2918_02SiO2_2o2, $f = 4\%$), *large holes* (D2920_02SiO2_2o2, $f = 10\%$), *connected nanoparticles* (D2920_03SiO2_2o2, $f = 25\%$) and *nanoparticles* (D2922_02Si_1o2, $f = 80\%$).

before the annealing, while without cleaning one of the samples was all *nanoparticles* and another was heavily stained.

If we compare the estimates of the crystallite size from the broadening of the GIXRD peaks to the one measured at the SEM, the latter is much larger. For example on the sample D2902_bSiO2_Er30, the estimate from the GIXRD data is $D = 80 \pm 5\,\text{nm}$, while the SEM images yield $D = 260 \pm 100\,\text{nm}$, where the error in the latter case accounts for the dispersion of the grain size distribution (i.e. it is not the uncertainty on the mean grain size). This discrepancy could be explained with the hypothesis that only the core of the grains observed at the SEM is actually in its proper crystalline state, while the grain borders are in a more disordered phase.

4.4 Hysteresis cycles

The key feature of vanadium dioxide is its Metal-Insulator Transition (MIT), and the simplest way to visualize such transition is through the displacement of the GIXRD peak at 28 degrees or the change in the transmittance spectrum with temperature. To make the measurements most efficient, the temperatures at which spectra were chosen to be not evenly spaced, but rather with an adaptive step, in order to obtain the maximum detail about the transition with a given number of measurements.

4.4.1 GIXRD

An example of the hysteresis cycle from GIXRD data can be seen in fig. 4.7, where the top two plots show the movement of the 28 degrees diffraction peak with temperature. Another way of visualizing the data is through the bottom contour plots, which better highlight that the transition happens at higher temperature when the temperature is increasing (ascent phase) with respect to the when it is decreasing (descent phase)

Similarly to what has been done to monitor the annealing process, it is possible to fit every spectrum with a Pseudo-Voigt (eq. (4.1)) function and then follow the position of the peak. In this way we are describing the phase transition as the gradual evolution of the monoclinic phase into the rutile one and viceversa (blue curve in fig. 4.8 left). An alternative approach is instead to interpret the transition as a coexistence between the M1 and R phases in which what performs the hysteresis cycle is the fraction of the monoclinic phase r_1. In this latter case the function fitting the data is the sum of two Pseudo-Voigt functions

$$f(x; A_1, \mu_1, \sigma_1, \alpha_1, A_2, \mu_2, \sigma_2, \alpha_2, a, b) = f_{PV}(x; A_1, \mu_1, \sigma_1, \alpha_1) + f_{PV}(x; A_2, \mu_2, \sigma_2, \alpha_2) + a + bx \tag{4.4}$$

where $\mu_1, \sigma_1, \alpha_1$ are kept fixed at the values from the single peak fit of the first spectrum at room temperature and $\mu_2, \sigma_2, \alpha_2$ to the one at the highest temperature. A_1 and A_2 are left free to vary during the fit and r_1 can be defined as $r_1 = \frac{A_1}{A_1 + A_2} \in [0, 1]$ (red curve in fig. 4.8 left).

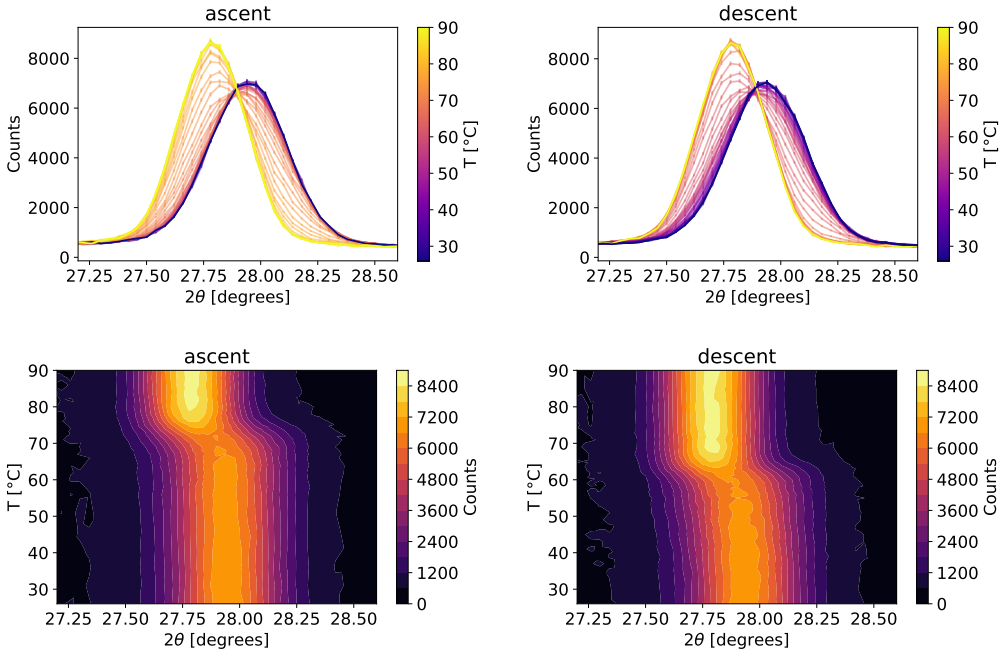

Figure 4.7: GIXRD hysteresis cycle on a 134 nm thick sample (D2918_Er_2o2). Data on the left column are acquired raising the temperature, while on the right decreasing it.

With the data acquired in this work, the two approaches are equally able to fit the spectra and yield hysteresis cycles on the peak center and on r_1 respectively which are virtually the same (left panel of fig. 4.8). However, from a previous work [48] the 28 degrees diffraction peak was so well resolved that during the transition it was clear that it was composed of two peaks of varying amplitude rather than a single peak with shifting position.

Once we have an hysteresis loop plot it is possible to fit its branches with a Comple-

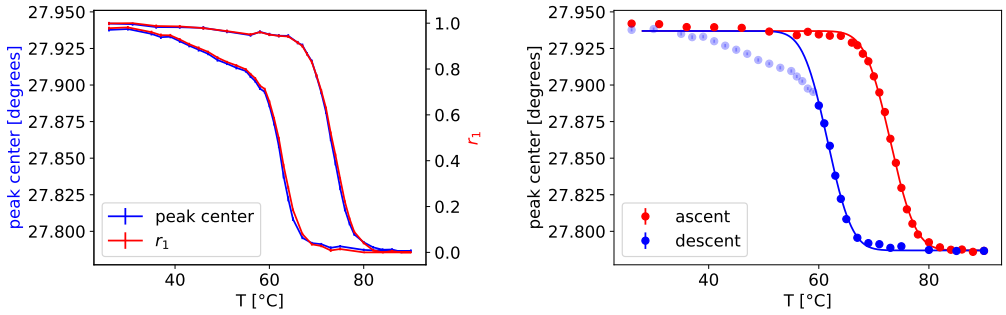

Figure 4.8: Hysteresis loops on the sample D2918_Er_2o2 analyzed with the two approaches of the single peak fit and the coexistence interpretation (left) and erfc fits (eq. (4.5)) on the one peak analysis (right).

mentary Error Function (erfc) function

$$f(x; A, \mu, \sigma, y0) = y0 + \frac{1}{2} A \mathrm{erfc}\left(\sqrt{2}\frac{x-\mu}{\sigma}\right) \tag{4.5}$$

$$\mathrm{erfc}(x) = 1 - \mathrm{erf}(x) = 1 - \frac{2}{\sqrt{\pi}} \int_0^x dt e^{-t^2} \tag{4.6}$$

So $\lim_{x\to-\infty} \mathrm{erfc}(x) = 2$, $\mathrm{erfc}(0) = 1$, $\lim_{x\to\infty} \mathrm{erfc}(x) = 0$. We can then call T_h and T_l the parameters μ from the fits respectively on data with ascending and descending temperatures, which will be the two transition temperatures. At this point $\Delta T = T_h - T_l$ will be a quantifier of the hysteresis loop width.

In the right panel of fig. 4.8 we can see that the heating curve is well described by the fit, while, on the other hand, the cooling one doesn't follow an erfc-like trend, and this is a behavior we observed in almost all samples. For this reason a possible alternative to ΔT to quantify the quality of the hysteresis loop is the area $\mathcal{A}$ between the heating and cooling curves in a normalized hysteresis loop, namely where the observed quantity is forced to have value 1 at room temperature and 0 at 90 °C. In this way we are able to compare results from different measurements techniques.

Another deviation from an ideal hysteresis loop is that sometimes the experimental ones do not close. This could be explained with the hypothesis of the coexistence of phases, saying that after a cycle some of the grains remained stuck in the rutile phase, and hence the peak didn't go back to its starting position. Usually this happens only in the first hysteresis cycles performed by the sample, and, after 5 to 7 conditioning loops the following cycles close properly. For example in fig. 4.9 we can see that the fourth hysteresis cycle still doesn't close, but the fifth one does.

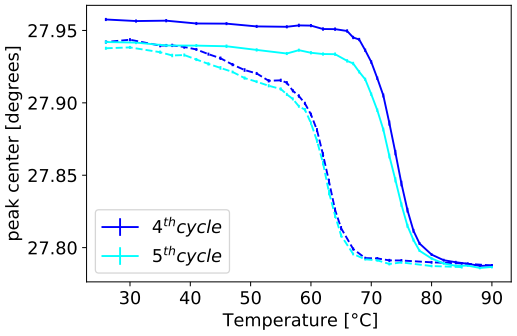

Figure 4.9: Example of a GIXRD hysteresis cycle that doesn't close (blue curve) and one that does (cyan curve).

4.4.2 Transmittance

As can be seen from fig. 4.10, the main feature of the transmittance spectra is a the change from quite high values in the NIR range at room temperature to considerably lower ones at high temperature. This is due to the fact that the monoclinic phase is semiconducting and hence lets a significant portion of the light pass through it, while the metallic rutile phase has much higher absorption coefficient (see also section 4.6).

If to extract an hysteresis loop out of the list of GIXRD spectra at the different temperatures we had to fit the peaks, in this case instead we can simply look at the evolution of the transmittance at a given wavelength, for instance 1540 nm which is the emission line of the Er:SiO_2 emitting layer (blue curve in fig. 4.11 left). To instead describe the

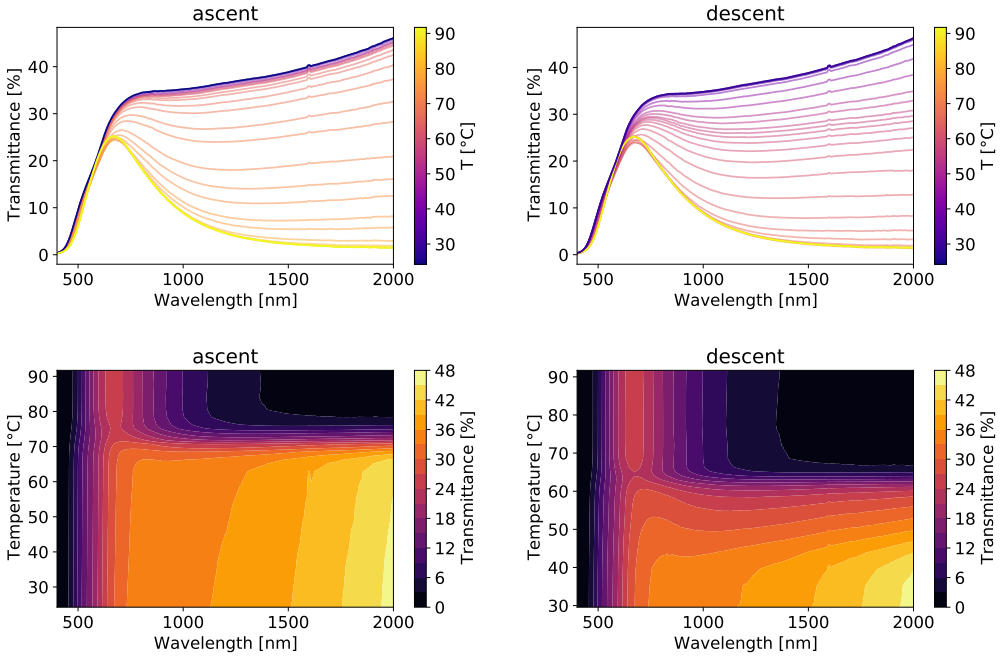

Figure 4.10: Transmittance hysteresis cycle on a the D2918_Er_2o2 sample. Analogously to fig. 4.7, data on the left column are acquired raising the temperature, while on the right decreasing it.

coexistence of phases, if we call $y_l(\lambda)$ and $y_h(\lambda)$ the experimental transmittance spectra at room and highest temperature, we can then write an intermediate spectrum as

$$y(\lambda, T) = r_1(\lambda) y_l(\lambda) + (1 - r_1(\lambda)) y_h(\lambda) \tag{4.7}$$

with the hypothesis that $r_1(\lambda)$ doesn't have a strong dependence on λ. Since this is true only in the NIR range because of the behavior of the transmittance peak at high temperatures (fig. 4.11 right), we can define an average fraction as

$$\langle r_1 \rangle = \langle r_1(\lambda) \rangle_{\lambda > \lambda_{low}} \tag{4.8}$$

which doesn't show a considerably different hysteresis cycle with respect to the one of the simple slice at 1540 nm (red curve in fig. 4.11 left).

It needs to be said that analyzing the coexistence hypothesis with this method is a crude approximation, since it is not theoretically correct to linearly combine transmittances. So, instead of interpreting $\langle r_1 \rangle$ as the fraction of the monoclinic phase, it is more of a method to evaluate the hysteresis over a range of wavelengths instead of a single one.

At this point the hysteresis loop is quite similar to the GIXRD one, and so we can analogously perform the erfc fits and compute the loop area $\mathcal{A}$

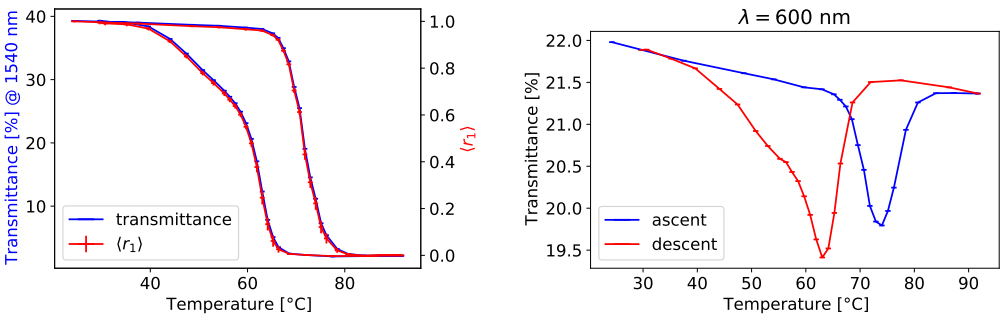

Figure 4.11: Transmittance hysteresis loop on sample D2918_Er_2o2 obtained by slicing the spectra at $\lambda = 1540\,\text{nm}$ and with the coexistence technique with $\lambda_{low} = 800\,\text{nm}$ (left). Slice of the spectra at $\lambda = 600\,\text{nm}$ (right), near the transmittance peak in the high temperature spectra.

4.4.3 Comparison

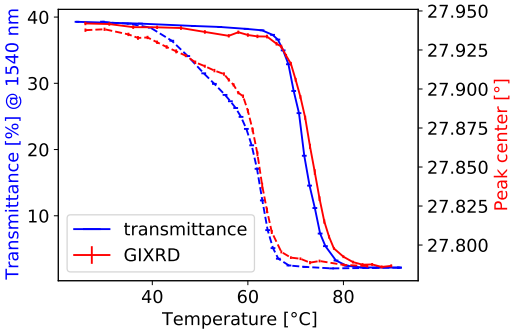

Figure 4.12: Comparison between transmittance and GIXRD hysteresis cycles performed on sample D2918_Er_2o2.

Since the GIXRD detects only the crystalline part of the sample, while the transmittance accounts also for eventual amorphous parts, it is interesting to compare the hysteresis cycles measured with the two techniques. As can be seen from fig. 4.12, despite the slight misalignment in temperature between the two cycles, which is most likey due to the different calibrations of the two instruments rather than a property of the VO_2 film, they are very similar. Moreover, if we look at the results in table 4.1 the width and area of the two cycles are almost identical, which proves that the two different techniques measure the same phenomenon. For this reason when discussing the effect of the annealing conditions on the hysteresis cycle we can focus only on the transmittance one.

technique	T_h [°C]	T_l [°C]	ΔT [°C]	$\mathcal{A}$ [°C]
GIXRD	72.97 ± 0.09	61.6 ± 0.3	11.4 ± 0.3	13
transmittance	71.65 ± 0.06	60.2 ± 0.5	11.5 ± 0.5	13

Table 4.1: Transition temperatures and hysteresis loop width of the D2918_Er_2o2 sample. The loop areas are computed using r_1 for the GIXRD data and $\langle r_1 \rangle$ for the transmittance ones.

4.5 Results of different annealing techniques

When samples are annealed at the diffractometer, the thermocouple that measures the temperature is very close to the sample, so it is reasonable to assume that the temperature of the sample is the one read by the thermocouple. On the other hand for annealing treatments in the oven the samples lay on a quartz slot, while the thermocouple is on the oven wall. Moreover, when a gas is fluxed into the oven, it removes heat from the sample. For these reasons, and we verified this inserting an additional thermocouple where the samples usually lay, the temperature on the sample surface is 20 to 30 °C lower than the one set by the oven. So, for clarity, when we refer to the annealing temperature, it is the one set by the oven.

Having said so, we can now look at the outcome of the different annealing treatments. First of all, all the annealing treatments on as-deposited samples in the oven in vacuum ($P \sim 10^{-5}$ mbar) with temperatures ranging from 600 to 800 °C and annealing times of roughly one hour yielded the V_2O_3 phase. However a subsequent annealing in the oven in N_2 flux or at the AP (which also is in N_2 flux) easily converts the phase to VO_2. On the other hand, annealing in vacuum a sample which already displays the VO_2 doesn't alter it. This could be explained considering that the RBS measurements performed on the as-deposited samples, suggest a VO_x stoichiometry with $x < 2$, which would mean that external oxygen is needed to form the VO_2 phase. When annealing in N_2 flux, small leaks in the pumping system or a slight impurity of the N_2 gas or desoprtion from the oven walls could introduce oxygen molecules in the annealing chamber. These can then adsorb on the hot sample surface and chemically interact with it, allowing the formation of the VO_2 phase. On the contrary when annealing in vacuum eventual oxygen molecules adsorbed on the oven walls are removed by the turbomolecular pump while the sample is still cold. By the time the sample heats up to the annealing temperature the partial pressure of oxygen is so low that there are too few interaction between the sample and oxygen molecules to bring the stoichiometry to VO_2, and so the film crystallizes into the less oxidized V_2O_3 phase.

Another interesting result is the dependence on the film thickness. To study it we performed annealing treatments at 570 °C in N_2 flux at 200 Nl/h for just half an hour on samples of different thicknesses. At the end of the annealing the samples with a thickness of 135 and 200 nm measured at the GIXRD presented spurious peaks and in some cases no peaks at all. On the other hand the peaks of the 60 nm thick sample were more clear and on an even thinner sample (37 nm) the diffraction peaks were the ones of VO_2. This suggests the reasonable fact that thicker samples require a longer annealing time, in contrast to what was observed from studying the kinetics of the annealing at the diffractometer. The effect of the annealing time can be seen not only via the GIXRD peaks, but also through the transmittance spectra acquired at the spectrophotometer (fig. 4.1 bottom), where an annealing of just half an hour yielded spurious spectra (red and orange curves).

To study instead the effect of the annealing temperature, we tried to anneal samples

of the same thickness (54 nm) in the oven with a 100 Nl/h N_2 flux at 520, 570 and 620 °C. Since the growth process of the grains has an exponential dependence on the annealing temperature and a linear one with respect to the annealing time, the annealing at 520 °C lasted 6 hours, while the other two just 2 hours. The effect on the grain size can be seen in fig. 4.13, where the grains of the sample annealed at 570 °C (yellow curve) are significantly smaller than the ones annealed at 620 °C (blue curve) and slightly smaller than the ones annealed at 520 °C. Since we want to produce samples with the smallest grains possible, we chose the annealing at 570 °C for 2 hours as the best recipe.

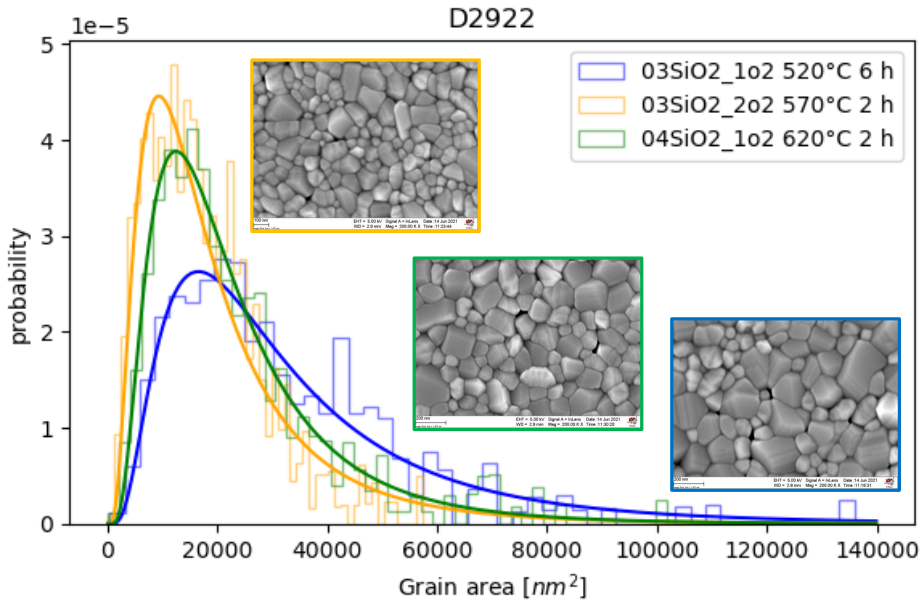

Figure 4.13: Lognormal fits of the grain distribution histograms from three samples of the D2922 deposition ($t_{VO_2} = 54$ nm) annealed in the oven in N_2 flux. The effective diameter of the grains is 190 nm for the one annealed for 6 hours at 520 °C, 140 and 150 nm for the ones annealed for 2 hours at 570 and 620 °C respectively.

The advantage of having small grains isn't just the fact that the film is more homogeneous and tends to have less holes, but also the hysteresis cycle is narrower. As can be seen in fig. 4.14, which plots the data in table 4.2, there is a clear correlation between the grain size (ϕ_{eff}) and the hysteresis loop area ($\mathcal{A}$). In particular, by performing a linear fit, we can say that

$$\mathcal{A} \sim a + b\phi_{eff} \qquad a = (4 \pm 2)\,°\text{C} \quad b = (7.5 \pm 0.8) \cdot 10^{-2} °\text{C/nm} \tag{4.9}$$

From fig. 4.14 we can also see that the samples annealed at the AP have in general larger grain sizes (and wider hysteresis) despite being annealed at the same temperature of the ones in the oven but for less time, which is counter intuitive. This can be explained

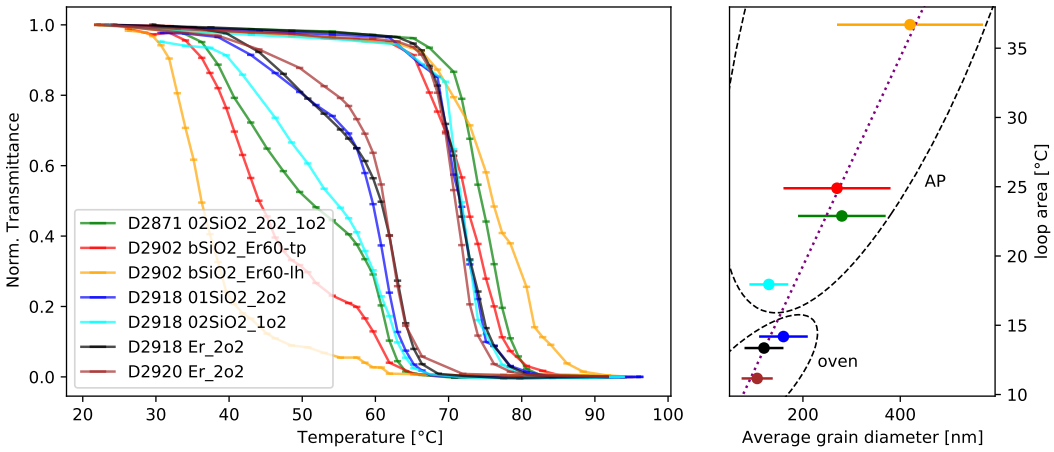

Figure 4.14: Comparison of the different hysteresis cycles of the samples in table 4.2 in terms of the normalized transmittance measured at the spectrophotometer at 1540 nm (left). On the right plot of the hysteresis loop area calculated from the left graph against the average grain size measured at the SEM.

considering that at the AP the samples are held by harmonic steel clips (which both induce stress on the surface and also leave dirt on it) and also the temperature rises and falls much quicker than in the oven. For instance, a sample at the AP takes roughly one hour to cool from 550 °C to room temperature, whereas the same process takes 8 to 12 hours in the oven due to its much higher thermal inertia. So, the annealing at the diffractometer is far more 'violent' than the one in the oven, which justifies the bigger grains.

Deposition	sample name	t_{VO_2} [nm]	annealing	ϕ_{eff} [nm]	$\mathcal{A}$ [°C]
D2871	02SiO2_2o2_1o2	135	AP 550 °C 1h	280 ± 90	23
D2902	bSiO2_Er60 tp	156	AP 550 °C 1h	270 ± 110	25
D2902	bSiO2_Er60 lh	156	AP 550 °C 1h	420 ± 150	37
D2918	01SiO2_2o2	135	oven N2 570 °C 2h	160 ± 50	14
D2918	02SiO2_1o2	135	AP 550 °C 1h	130 ± 40	18
D2918	Er_2o2	135	oven N2 570 °C 2h	120 ± 40	13
D2920	Er_2o2	137	oven N2 570 °C 2h	110 ± 30	11

Table 4.2: Samples that were both measured at the SEM and performed an hysteresis cycle at the spectrophotometer. t_{VO_2} is the thickness of the VO_2 layer, ϕ_{eff} is the effective diameter measured at the SEM and $\mathcal{A}$ is the loop area of the hysteresis cycles measured at the spectrophotometer at 1540 nm (fig. 4.14). Sample D2902_bSiO2_Er60 was measured in two regions, one with tightly packed grains (tp) and the other with large holes (lh).

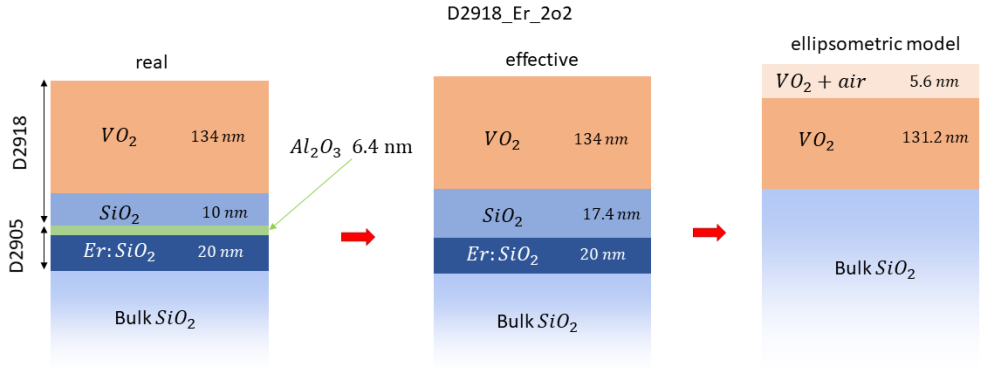

Figure 4.15: Scheme of the D2918_Er_2o2 sample: from left to right the real geometry of the sample, then the approximation of including the Al_2O_3 capping layer into the SiO_2 spacer above it and finally the ellipsometric model.

4.6 Ellipsometry

In order to do computations with the CPS model (section 2.1) it is necessary to know the dielectric functions of the VO_2 layer. For this reason we performed ellipsometric measurements on the D2918_Er_2o2 which is the sample that better displayed the coupling between the VO_2 thin film and the Er:SiO_2 emitting layer underneath. The detailed structure of the sample can be seen in fig. 4.15 where in the middle scheme the Al_2O_3 capping layer and the SiO_2 spacer were combined together into an effective SiO_2 layer with thickness

$$t^{eff}_{SiO_2} = t_{SiO2} + \frac{n_{Al_2O_3}}{n_{SiO2}} t_A l_2 O_3 = 10\,\text{nm} + \frac{1.66}{1.44} 6.4\,\text{nm} = 17.4\,\text{nm} \tag{4.10}$$

The thickness of the VO_2 layer was measured with the AFM to be 134 nm and also the sample had a surface roughness of 5.6 nm. For the sake of the ellipsometric measurements all the layers below the VO_2 one (SiO_2 spacer, Al_2O_3 capping layer and Er:SiO_2 emitting layer) can be grouped together with the substrate as bulk SiO_2 with a thickness of the order of millimeters. Hence the model used for simulating the data (last scheme in fig. 4.15) will be a 1 mm thick SiO_2 layer, than a 131.2 nm thick VO_2 layer and finally a 5.6 nm layer of 50% VO_2 and 50% air which accounts for the surface roughness of the sample ($131.2 + 5.6/2 = 134$ nm).

At this point there are various ways to proceed with the fitting of the data. The simplest one is performing an independent fit of the refractive index n and the extinction coefficient k for every wavelength, using only the ellipsometric data (Ψ and Δ). This fit easily succeeds (Mean Square Error (MSE) below 1) but is quite unstable, yielding pretty different results with different initialization parameters. To stabilize the fits we then used also transmittance data acquired at the spectrophotometer, where at room temperature it was possible to measure transmittance spectra at different angles of incidence θ and polarizations, while to keep the sample at 90 °C we had to use the heated sample holder, which allows to acquire spectra only at normal incidence.

If we still try to perform a point by point fit including the transmittance data, the results in terms of n and k are extremely noisy to the point of being meaningless. For this reason we instead modeled the dielectric function of the VO_2 layer as a sum of 3 Lorentzian oscillators, which comes with the advantage of yielding a smooth profile for n and k by definition and also automatically satisfies the Kramers-Kronig condition, which wasn't the case for the point by point fit. With these constraints the fits struggle a bit, as can be seen from fig. 4.16, and yield an MSE of 7.4 for the monoclinic phase and 6.3 for the rutile one, which is still acceptable (MSE < 10). One might argue that the fits don't describe well the data because the model used is too simple. However when I tried complicating it, for example by increasing the number of oscillators, adding void enclosures between the silica and the VO_2 layer to simulate the tiny holes in the film, or mixing the monoclinic and rutile phases in the room temperature data to account for the presence of grains that didn't make the transition back to the monoclinic phase, the fits didn't improve, and even yielded unphysical results such as a negative percentage of rutile phase in the monoclinic one. For this reason a further complexity was not justified. On the other hand a possible explanation of why the fits don't perform very good could be the fact that the VO_2 film is not isotropic, but rather has preferred directions, which is quite reasonable considering how the samples are fabricated [49] and it is supported by the fact that we do not see at the GIXRD all the peaks we should.

In the end, if we compare the derived n and k with the ones of the literature, we can see that there is a good agreement for the rutile phase, and a poorer one for the monoclinic phase. This is actually not very concerning since in the literature values of the dielectric constant of VO_2 vary a lot (table 4.3).

Source	monoclinic	rutile
This work	$3.16 + i0.25$	$1.85 + i3.28$
[31]	$3.30 + i0.30$	$1.77 + i3.35$
[50]	$2.7 + i0.7$	$2.4 + i3.4$
[51]	$3.0 + i0.2$	$1.5 + i3.0$

Table 4.3: Complex refractive index of VO_2 at 1540 nm in this work and in the literature.

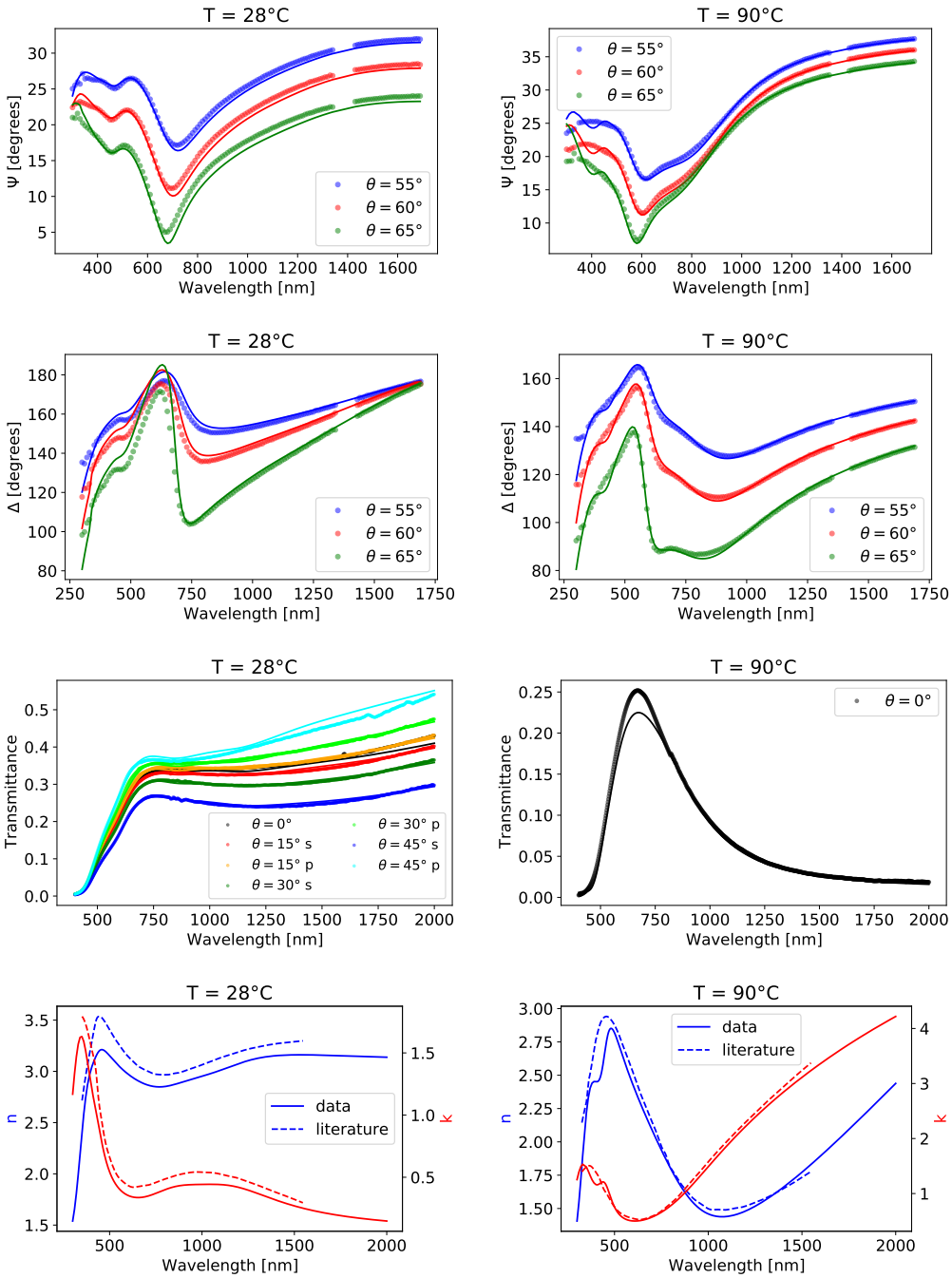

Figure 4.16: Data (circles) and fits (solid lines) of the ellipsometric measurements (first 6 plots). In the polts of Ψ and Δ there is a gap in the data between 1340 and 1430 nm that is not covered by the lamps of the ellipsometer. The last two plots show the derived optical constants for VO_2 compared to the ones found in the literature ([31]).

Chapter 5

Coupling of the Er:SiO_2 emitting layer with a VO_2 thin film

Up to now we have studied the properties of VO_2 thin films and characterized their Metal-Insulator Transition (MIT). The next step is to couple the film of vanadia to an Er:SiO_2 emitting layer and use the phase transition of VO_2 to actively control the emission properties of the Er^{3+} ions. An example of how this can be achieved is shown in fig. 5.1, where we can see the structure of a sample with a 20 nm thick emitting layer with and without the deposition of the VO_2 thin film. The sample without VO_2 is used as a reference to characterize the properties of the emitting layer alone, while the second is used to study the effects of the coupling of the emitting layer with the film of vanadia.

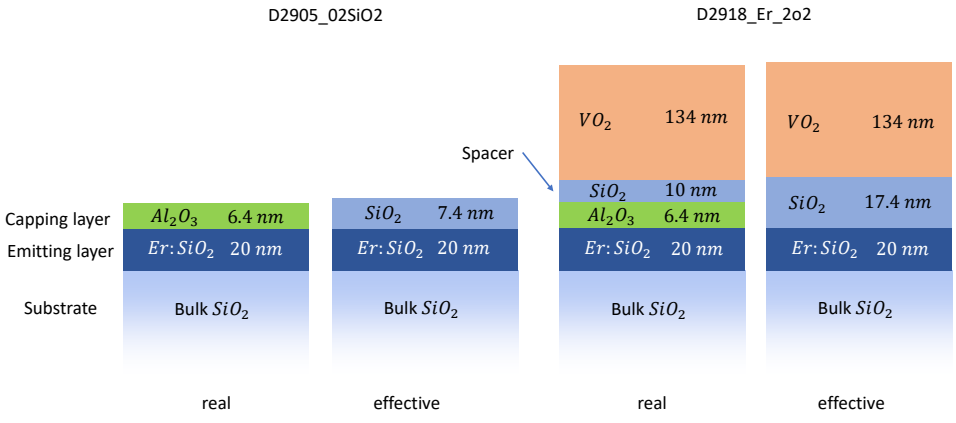

Figure 5.1: Schematics of a reference sample with an emitting layer and no VO_2 (left) and of the same sample after the deposition of a SiO_2 spacer and a VO_2 film (right). For both cases is reported the real structure of the sample and an effective one which approximates the Al_2O_3 capping layer as a thicker SiO_2 one, as explained in section 4.6.

5.1 Analysis of the waveforms

If there are many experimental techniques to characterize the behavior of the VO_2 layer, photoluminescence (PL) is the only one that is able to describe the properties of the Er:SiO_2 emitting layer. Referring to section 3.2.8, since the pump laser is mechanically chopped, the time-dependent signal that is outputted by the detector has the typical shape that can be seen in fig. 5.2, that features alternating charging and discharging processes with a frequency that is the one of the chopper f_{ch}. From these waveforms we need to extract the decay rate of the sample, so let us take a detailed look at them.

If Γ is the total decay rate and $N(t)$ the number of Er^{3+} ions in their excited state, during the discharge process the blade of the chopper interrupts the pump laser beam, and so we can write

$$\frac{\partial N}{\partial t} = -\Gamma N \quad \rightarrow \quad N(t) = N_0 e^{-\Gamma t} \tag{5.1}$$

and if Γ_c is the decay rate associated to the photons that are collected by the apparatus, the measured PL intensity is

$$I(t) \propto -\left.\frac{\partial N}{\partial t}\right|_c = \Gamma_c N(t) = \Gamma_c N_0 e^{-\Gamma t} \tag{5.2}$$

On the other hand when the chopper blade frees the path of the laser, an additional pumping term R_p must be added to eq. (5.1):

$$\frac{\partial N}{\partial t} = R_p - \Gamma N \quad \rightarrow \quad N(t) = \frac{R_p}{\Gamma}\left(1 - e^{-\Gamma t}\right) \tag{5.3}$$

and hence $I(t) \propto \Gamma_c \frac{R_p}{\Gamma}\left(1 - e^{-\Gamma t}\right)$. The important thing to notice here is that the characteristic charging and discharging times are the same.

The behavior described in eqs. (5.1) and (5.3) is quite simplified, in particular real samples have a distribution of emitters with different decay rates due for example to the different distance from an interface. So let us define a general normalized decay function

$$d(t) \quad \text{such as} \quad d(0) = 1, \lim_{t\to\infty} d(t) = 0 \tag{5.4}$$

that will account for such distribution of decay rates and in practice can be one of the functions in table 5.1.

name	formula
single	$d_1(t;\tau) = e^{-t/\tau}$
double	$d_2(t;\tau_1,\tau_2,r_1) = r_1 e^{-t/\tau_1} + (1-r_1)e^{-t/\tau_2}$
stretched	$d_s(t;\tau,\beta) = e^{-(t/\tau)^\beta} \quad \tau_{eff} = \frac{\Gamma_E(1/\beta)}{\beta}\tau$

Table 5.1: List of the normalized exponential decay functions used in this thesis. For the stretched exponential in the formula for the effective decay time τ_{eff}, $\Gamma_E(\cdot)$ is Euler's gamma function.

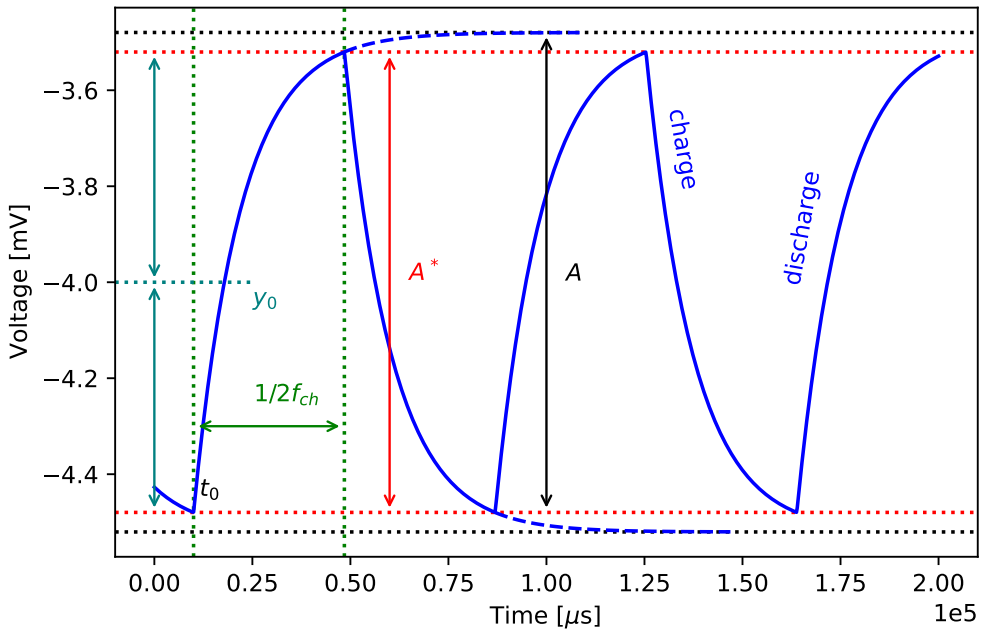

Figure 5.2: Shematics of the characteristic waveform of the PL detector. The detector is polarized with negative voltage, so during the discharge process the voltage increases because it is decaying in absolute value.

At this point we have to consider the effect of the chopper, which, depending on the ratio between its frequency and the effective decay rate of the samples makes the charging and discharging processes more or less complete. If $\tau_{ch} = 1/2f_{ch}$ is the half period of the chopper and we assume that the first discharge starts at time t_0, we can define an integer counter n which tells us in which half cycle of the chopper we are as

$$n(t) = \left\lfloor \frac{t - t_0}{\tau_{ch}} \right\rfloor \tag{5.5}$$

and then the entire waveform can be described as

$$y(t) = y_0 + (-1)^{n(t)} A \left(1 - d(t - (t_0 + n(t)\tau_{ch})) - \frac{1}{2}\left(1 - d(\tau_{ch})\right) \right) \tag{5.6}$$

where A is the amplitude of the last decay if the chopper was suddenly stopped. It is important to notice that this is not equivalent to the amplitude of the decays in the limit of low chopper frequency, as in this latter case the charge and discharge processes reach their asymptotic values, while instead A is related to the decay of all the ions that were able to be excited by the incomplete charging process. Another way to think of A is that the measured amplitude of the waveform is

$$A^* = A\left(1 - d(\tau_{ch})\right) \tag{5.7}$$

To extract information from the waveform, one could in principle crop the data to just a single discharge segment and fit it. However this cropping process is very delicate,

since the choice of the starting instant can highly affect the results of the fit, but is also quite tricky because it isn't trivial to recognize with precision from the data where a half cycle ends and the following starts (fig. 5.3). This is due to the fact that the beam spot of the pump laser has a finite size and so there is a transient time as the edge of the chopper blade crosses it in which the sample is partially illuminated. This, together with the electronic characteristic RC times, contributes in smoothing the transition between charge and discharge.

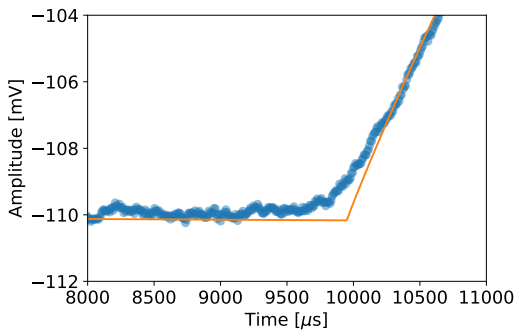

Figure 5.3: Data and periodic decay fit of a waveform in the transition between charge and discharge.

On the other hand, thanks to eq. (5.6), it is possible to fit the whole waveform exploiting its periodic behavior for a more reliable estimate of t_0. Moreover, fitting the whole waveform instead of a single segment comes with the other advantage of using the tail of the last charging process to fix the y value at the start of the discharge, a parameter which was instead free to roam when fitting the single segment and, similarly to t_0, has a great impact on the fit results.

Up to now we discussed the time-resolved measurements. Instead when acquiring wavelength-resolved spectra the waveform isn't visualized by the oscilloscope but rather goes into a lock-in amplifier that uses the square wave signal of the chopper as a reference. This means that the DC voltage value outputted by the amplifier is proportional to the integral of the waveform during a half cycle. Namely the intensity measured is

$$I = \int_{t_0}^{t_0+\tau_{ch}} dt \left(y_0 + \frac{A^*}{2} - y(t) \right) = \int_0^{\tau_{ch}} dt A d(t) \tag{5.8}$$

5.2 Er:SiO_2 emission spectra and lifetimes without VO_2

The typical shape of a PL spectrum can be seen in the left panel of fig. 5.4 and it is due to the convolution of the several emission lines of the Er^{3+} ions that originate from the fine splitting of both the ${}^4I_{13/2}$ and ${}^4I_{15/2}$ levels (fig. 1.1). Since our measurements are performed at room temperature or higher, the lines are consistently broadened and so we are not able to resolve them. On the right panel we can instead see a discharge segment fitted both with a single (red curve) and a stretched exponential decay (orange curve). The evident trend in the residuals of the single exponential fit means that we are able to capture the fact that the emitting layer has a finite thickness and hence the decay rate of the Er^{3+} ions is amplified slightly differently according to their distance from the interface with the air. For this reason the lifetimes are fitted with a stretched exponential decay

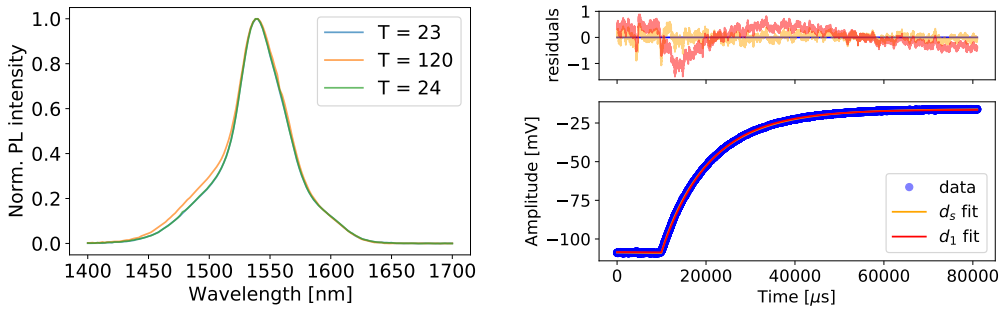

Figure 5.4: PL spectra (left) measured at room temperature, then at high temperature and then again at room temperature. On the right lifetime at 1540 nm at room temperature fitted both with a single exponential d_1 and with a stretched exponential d_s.

and the measured total decay rate Γ^{exp} can be derived from the effective lifetime τ_{eff} as

$$\Gamma^{exp} = \frac{1}{\tau_{eff}} \tag{5.9}$$

Since the waveforms contain over 12000 datapoints the reduced χ^2 of the fits and the error on the fit parameters are extremely small. For this reason we can assume a conservative 5% uncertainty on the quantities derived from the fits.

In order to understand which temperature dependent effects are intrinsic of the emitter layer and which are instead due to the phase transition of VO_2, we measured samples with the Er:SiO_2 emitting layer before the deposition of vanadia (fig. 5.1 left) both at room and high temperature. From the left panel of fig. 5.4 we can see that the spectrum at high temperature is slightly different from the one at room temperature, suggesting that the emission lines at lower wavelength are more enhanced with temperature with respect to the main line at 1540 nm. This differences, however, are quite small.

Focusing now on the lifetimes, if we look at the results of the fits shown in table 5.2, we can see that the fluctuation of the lifetime is well inside the 5% errorbar. So we can assume that it doesn't change with temperature and we can settle on an intermediate value for the decay rate Γ^{exp} of

$$\Gamma^{exp} = 92 \pm 5\,\mathrm{s}^{-1} \tag{5.10}$$

T [°C]	τ [ms]	β	τ_{eff} [ms]	Γ^{exp} [s^{-1}]
23	10.8	0.96	11.0	91
120	10.6	0.96	10.8	93
24	10.7	0.95	11.0	91

Table 5.2: Results of the d_s fits of the lifetimes.

A possible explanation of the fact that we see a slight difference in the spectra but none in the lifetime could be that at high temperature the refractive index of the SiO_2

matrix, in which the emitters are embedded, changes slightly. This doesn't affect much the decay rate but instead modifies the emission lines of the Er^{3+} ions and hence affects the PL spectra.

5.2.1 Estimate of the intrinsic non-radiative decay rate

The structure of the sample from which the data shown in fig. 5.4 and table 5.2 are taken, is the one displayed on the left of fig. 5.1. It consists of a 20 nm thick Er:SiO_2 layer on top of a silica substrate capped by a 6.4 nm Al_2O_3 layer, which can be approximated as a 7.4 nm thick SiO_2 layer. In this latter case the CPS model used to describe the sample is a Single Interface (SI) (section 2.1.1) model with the first medium being silica and the second air and having the emitters in a box distribution ranging from 7.4 to 27.4 nm from the interface. If we instead do not perform the approximation, the model is a Finite Thickness (FT) (section 2.1.2) one and resembles the real structure of the sample. Assuming the radiative decay rate in bulk silica to be $\Gamma_{0,r} \approx 100\,\mathrm{s}^{-1}$ ([12, 32]), we can then compute the predicted Electric Dipole (ED) and Magnetic Dipole (MD) radiative decay rates and, since the transition at 1540 nm has equal contributions from the two modes [32], the average radiative decay rate can be computed simply as

$$\Gamma_r = \frac{1}{2}\left(\Gamma_r^{ED} + \Gamma_r^{MD}\right) \tag{5.11}$$

As can be seen from table 5.3 the two models yield very similar results, meaning that replacing the Al_2O_3 layer with a thicker SiO_2 one is a good approximation. The simulations also show that the ED transition is enhanced roughly 17% more with respect to the MD one.

model	Γ_r^{ED} [s^{-1}]	Γ_r^{MD} [s^{-1}]	Γ_r [s^{-1}]
SI	75.8	62.5	69.2
FT	76.2	62.7	69.5

Table 5.3: Results of the CPS simulations for the D2905_02SiO2 sample with the Single Interface (SI) and Finite Thickness (FT) models.

The simulation of the predicted radiative decay rate allows us to obtain an estimate of the intrinsic non-radiative decay rate $\Gamma_{0,nr}$ as

$$\Gamma_{0,nr} = \Gamma^{exp} - \Gamma_r = 23 \pm 5\,\mathrm{s}^{-1} \tag{5.12}$$

Since this decay rate is due to defects in the emitting layer generated during its synthesis and annealing, we can assume that it isn't affected by the subsequent deposition of the SiO_2 spacer and VO_2 film.

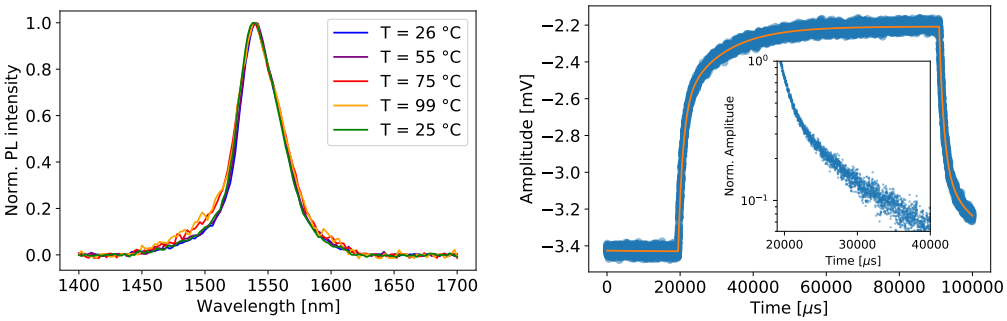

Figure 5.5: PL spectra at different temperatures (left) and emission waveform (right) acquired at room temperature with a 7 Hz chopper frequency. In the inset is displayed the normalized discharge section in logarithmic scale. Data from the D2918_Er_2o2 sample.

5.3 Er:SiO$_2$ emission spectra and lifetimes with VO$_2$

At this point we have reached the most important part of this thesis, where we can finally look at the effect of the phase transition of VO$_2$ on the emission properties of the Er^{3+} ions.

Let us start by considering the spectra: if we look at the left panel of fig. 5.5, we can see that the spectra from room temperature and up to 55 °C are virtually the same, while the two measurements at high temperature (red and orange curves) are slightly different, similarly to what observed in fig. 5.4 on the sample without the VO$_2$ layer. This suggests that the change in the spectra is an intrinsic property of the emitting layer and is not influenced considerably by the phase transition.

On the other hand if we look at the right panel of fig. 5.5, we can see the waveform of the emission at 1540 nm with its characteristic periodic behavior. In the inset is reported the first part of the discharge in logarithmic scale, which clearly highlights the presence of two components. The fast component has a lifetime τ_1 of roughly 1 ms, while the slow one ($\tau_2 \approx 12$ ms) is compatible to the one measured on the sample without the VO$_2$ layer. This presence of a double component is observed in all samples with a VO$_2$ layer. The relative amplitude of the fast component r_1 is around 0.7 for the measurement at room temperature on the D2918_Er_2o2 sample and fluctuates from 0.5 to 0.9 on the other samples. This means that a significant portion of the emitters 'feels' air instead of vanadia on top of it.

In order to explain how this is possible we can look at the left panel of fig. 5.6, where we can see well the shape of the VO$_2$ grains and in particular we can notice in the red circle with enhanced contrast that, around their edges, the grains are slightly lifted from the smooth layer underneath. If we now look at the right panel we can see three typical situations for the emitters (yellow stars). In case 1 the emitter is underneath a region where the VO$_2$ grain has a good adhesion and so the emitted electromagnetic field (black arrow) is reflected back to the emitter from the interface between SiO$_2$ and VO$_2$ (red arrow). We can then say that this emitter 'feels' the VO$_2$. On the other hand if the emitter is

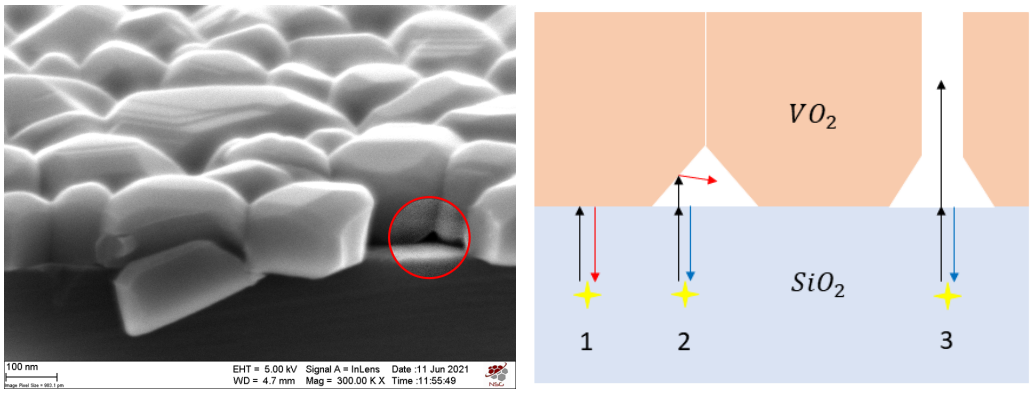

Figure 5.6: Cross section SEM image of the VO_2 grains (left). In the red circle it is possible to see the rounded bottom edge of the grain. Scheme of the interaction of the Er^{3+} ions with the shape of the VO_2 grains (right).

underneath a hole between the grains (case 3), the reflected field that reaches the emitter comes from the interface between SiO_2 and air, and so the emitter feels the air. Finally in case 2 the reflection from the interface between SiO_2 and air reaches back the emitter, while the one coming off the VO_2 doesn't because the surface of the grain is tilted. So, from the point of view of the emitters, case 2 and case 3 are the same.

This is important because, when measuring the surface of the sample at the SEM, we are able to estimate the filling fraction of the holes (case 3), which for the D2918_Er_2o2 is below 1% and so isn't able to explain why we measure $r_1 = 0.7$. On the other hand the instances of case 2 are not detectable by SEM but most likely occur at every grain edge in different amounts depending on the adhesion to the SiO_2 layer beneath, and are hence able to explain the missing fraction of emitters that feel the air (more on this later).

5.3.1 Photoluminescence hysteresis cycle

A first visualization of the hysteresis cycle can be obtained directly from the temporal decay curves (fig. 5.7), where in the main plots we can see the behavior of the fitting curves[1] as the temperature is increased and then decreased and in the insets the data of the normalized decays at low and high temperature. In particular we can see the clear presence of two components and the fast component getting faster (steeper decay) as the temperature is increased. To focus the attention on the fast component of the decay, the measurements were taken using a chopper frequency of 29 Hz.

Since the temporal decays feature two components, the simplest function that can describe them is the periodic double decay, which in principle has 6 free parameters $t_0, y_0, A, \tau_1, \tau_2, r_1$ (see eq. (5.6) and table 5.1), which are quite a lot. In order to reduce the number of free parameters we can, first of all, consider that the waveforms are recorded by the oscilloscope, which is triggered on the square wave signal of the chopper, so the

[1]The data are quite noisy, as can be seen from the right panel of fig. 5.5, so showing multiple waveforms in the same plot would make it illegible.

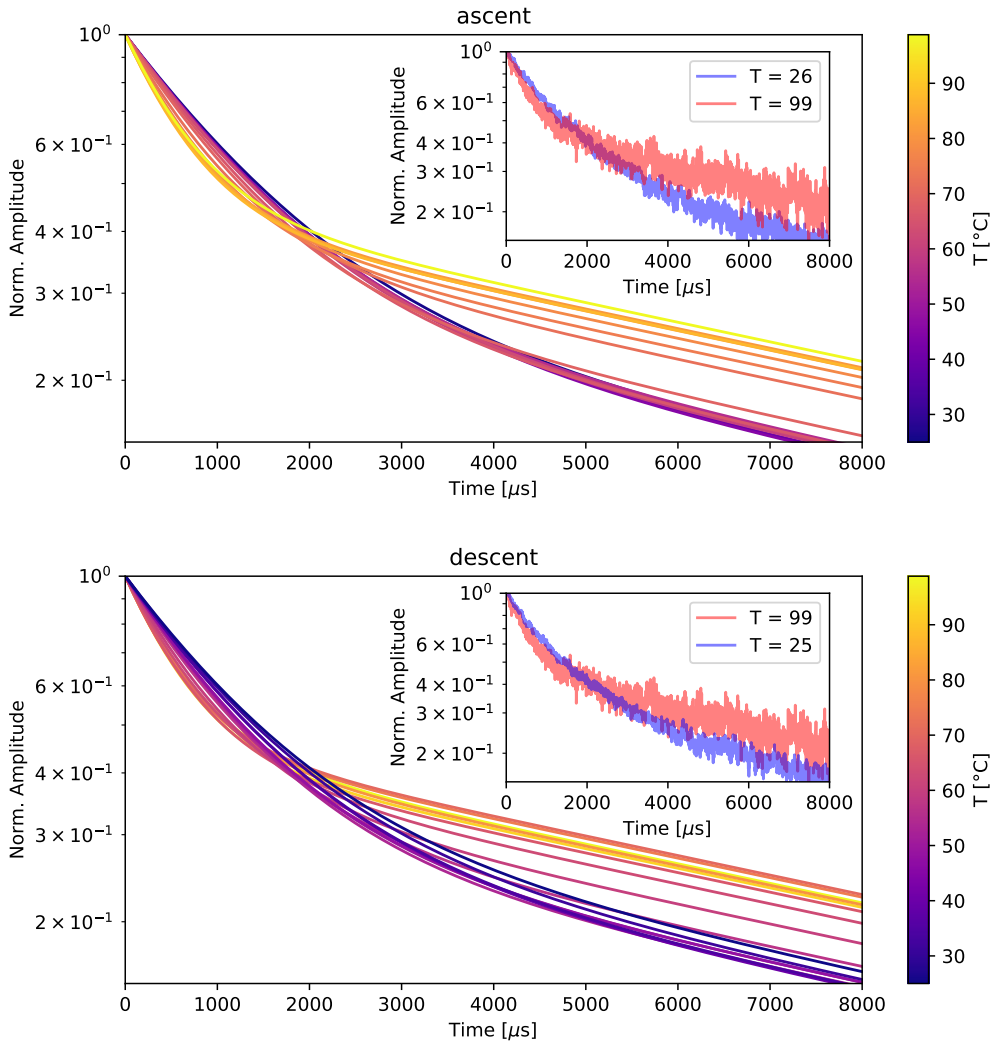

Figure 5.7: PL hysteresis cycle on the sample D2918_Er_2o2. Data on the top plot are acquired raising the temperature, while on the bottom decreasing it. The insets show the experimental normalized decays at low and high temperature.

value of the parameter t_0 has to be the same throughout all the measurements. Moreover, the slow component τ_2 is due to air, and so, according to what observed in section 5.2, it shouldn't vary during the hysteresis cycle. It has to be noticed that in section 5.2 only the Al_2O_3 capping layer was between the emitting layer and air, while in this case we have also to consider the 10 nm thick SiO_2 spacer (fig. 5.1). However, if we perform the CPS computations in this latter case, the predicted radiative decay rate is $\Gamma_r = 70.8\,s^{-1}$, which is very close to the one predicted for the thinner spacer. For this reason we can fix the lifetime of the slow component to the one measured in section 5.2 $\tau_2 = 11\,ms$, and the fact that this doesn't introduce weird trends in the residuals of the fits with respect to the case when τ_2 was left free to vary confirms that this is reasonable hypothesis to make.

If we now follow the fit parameters during the hysteresis, we obtain the results shown in fig. 5.8. On the left we can see the cycle of the fast component τ_1 and of its fraction in

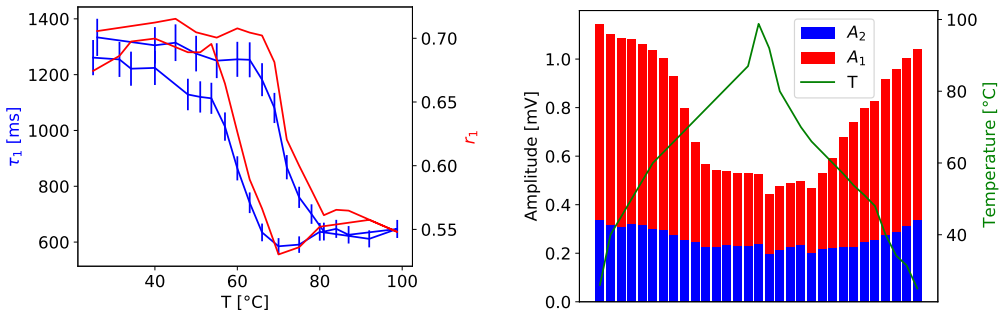

Figure 5.8: (Left): hysteresis cycles of τ_1 (blue curve, left-hand scale) and r_1 (red curve, right-hand scale). (Right): behavior of the amplitudes of the two components during the hysteresis.

the decay r_1. If the change in τ_1 is a direct symptom of the phase transition of VO_2, the cycle of r_1 is not so immediate to explain. To do so we have to look at the right panel of fig. 5.8 where it is reported the behavior of the absolute amplitudes of the two components

$$A_1 = Ar_1 \qquad A_2 = A(1 - r_1) \tag{5.13}$$

and, as we can see, both A_2 and A_1 assume smaller values when the temperature is increased, but for A_1 the effect is much more pronounced. To explain this behavior we have to recall the charge and discharge processes described in section 5.1 and in particular eqs. (5.1) and (5.3), where the amplitude of the decay is determined by the number of excited ions at the end of the charging process

$$N_0 = \frac{R_p}{\Gamma}\left(1 - e^{-\Gamma\tau_{ch}}\right) \tag{5.14}$$

which is inversely proportional to Γ if the product $\Gamma\tau_{ch}$ is large enough, which is definitely the case for the population of emitters that see VO_2. Since for those emitters the decay rate increases significantly when the VO_2 film goes from the monoclinic to the rutile phase, we also expect to see a lower amplitude A_1 at higher temperaures. On the other hand, there is no change in the lifetime of the emitters that feel the air and so we expect A_2 to stay constant.

T [°C]	τ_1 [ms]	A_1 [mV]	A_2 [mV]	A [mV]	r_1
26	1.33 ± 0.07	0.81 ± 0.04	0.34 ± 0.02	1.14 ± 0.06	0.71 ± 0.04
99	0.65 ± 0.03	0.29 ± 0.01	0.24 ± 0.01	0.53 ± 0.03	0.55 ± 0.03

Table 5.4: Values of the fit parameters at room temperature and at the highest one.

If this explanation is correct we also expect

$$\frac{A_1^h}{A_1^c} = \frac{\Gamma_1^c}{\Gamma_1^h} = \frac{\tau_1^h}{\tau_1^c} \quad \rightarrow \quad r = \frac{A_1^h}{A_1^c}\frac{\tau_1^c}{\tau_1^h} = 1 \tag{5.15}$$

where the h and c indices refer respectively to the hot and cold temperatures. However if we try to perform the computation with the results from table 5.4, we obtain $r = 0.74 \pm 0.07$.

To improve our explanation we can now consider that also A_2 diminishes with temperature, and this can be explained considering that the thermal dilation of the copper tip of the cryostat to which the sample is mounted might move it slightly out of the focus of the collection lenses, which results in the measurement of a lower intensity but doesn't influence the lifetime of the sample. If we now assume that this misalignment makes us lose a fixed percentage of the PL photons, we can account for this effect in the definition of r and this time we obtain

$$r = \frac{A_1^h/A_2^h}{A_1^c/A_2^c}\frac{\tau_1^c}{\tau_1^h} = 1.0 \pm 0.1 \tag{5.16}$$

We can now apply this reasoning also for the estimation of the fraction f of emitters that see air by writing the two decay amplitudes as

$$A_1 \propto (1-f)\tau_1 \quad A_2 \propto f\tau_2 \quad \Longrightarrow \quad x = \frac{A_1\tau_2}{A_2\tau_1} = \frac{1-f}{f} \quad \Longrightarrow \quad f = \frac{1}{x+1} \tag{5.17}$$

which leads us to obtain $f = (4.8 \pm 0.4)\%$ at room temperature and $f = (4.6 \pm 0.4)\%$ at high temperature. These values are compatible with each other and can be easily explained by the reasoning done before on the shape of the grains.

5.3.2 Comparison with the other hysteresis cycles

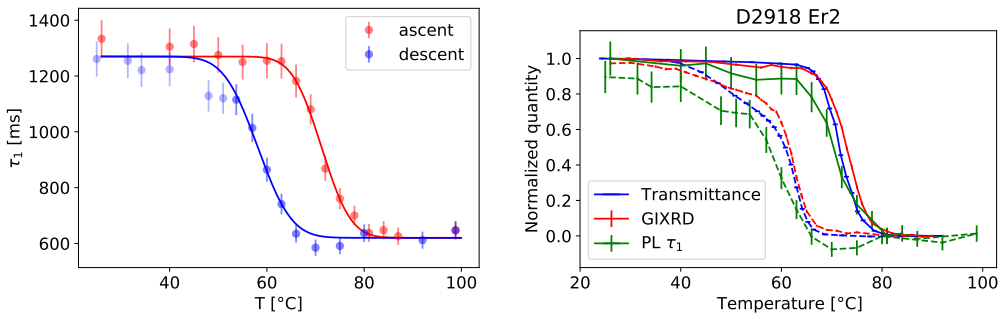

Figure 5.9: Erfc fits of the τ_1 hysteresis loop (left) and comparison with the loops measured in transmittance and at the diffractometer.

Similarly to the hysteresis cycles measured with the GIXRD and transmittance techniques, we can fit the two branches of the PL cycle with erfc functions to estimate the loop width ΔT and then compute the loop area $\mathcal{A}$. From the left panel of fig. 5.9 we can see the erfc fits of the heating and cooling curves, and in table 5.5 are reported the parameters of the cycle compared to the GIXRD and transmittance ones. The PL cycle appears wider and slightly shifted to lower temperatures, but this is most probably due to the different temperature calibrations for the various instruments. In the right panel of fig. 5.9 the three cycles from different measurement techniques are plotted together, and we can see that the PL one, despite being more noisy, fits quite well with the other two.

technique	T_h [°C]	T_l [°C]	ΔT [°C]	$\mathcal{A}$ [°C]
GIXRD	72.97 ± 0.09	61.6 ± 0.3	11.4 ± 0.3	13
transmittance	71.65 ± 0.06	60.2 ± 0.5	11.5 ± 0.5	13
photoluminescence	71.2 ± 0.3	58.1 ± 0.3	13.1 ± 0.4	17

Table 5.5: Transition temperatures and hysteresis loop width of the D2918_Er_2o2 sample.

5.3.3 Comparison with the CPS model

From the measurements of the fast lifetimes at room and high temperature it is possible to compute the experimental Purcell factor

$$P^{exp} = \frac{\Gamma_r}{\Gamma_{0,r}} = \frac{1/\tau^{exp} - \Gamma_{0,nr}}{\Gamma_{0,r}} \tag{5.18}$$

using the estimate of the non-radiative decay rate $\Gamma_{0,nr}$ found in section 5.2.1 and then compare it with the one predicted by the CPS model P^{th} using the optical constants of VO_2 measured at the ellipsometer (section 4.6).

T [°C]	P^{exp}	P^{th}	$P^{th}_{corrected}$
26	7.3 ± 0.4	4.0	7.4
99	15.2 ± 0.8	11.8	15.2

Table 5.6: Comparison of the experimental and theoretical estimates of the Purcell factor. The last column is the theoretical estimate with a corrected model for the sample.

If we look at the results shown in table 5.6, we can see that the agreement between theory and experiment is not so good. Not only the model underestimates the Purcell factors, but also overestimates the switching factor $S = P_h/P_l$, predicting a value of almost 3 whereas we measured

$$S^{exp} = 2.1 \pm 0.2 \tag{5.19}$$

A first explanation of why the measured decay rates are higher than the predicted ones could be an increase in the intrinsic non-radiative decay rate due to a deterioration of the emitting layer. However this would imply as well a consistent reduction of the lifetime of the slow component, which we do not observe.

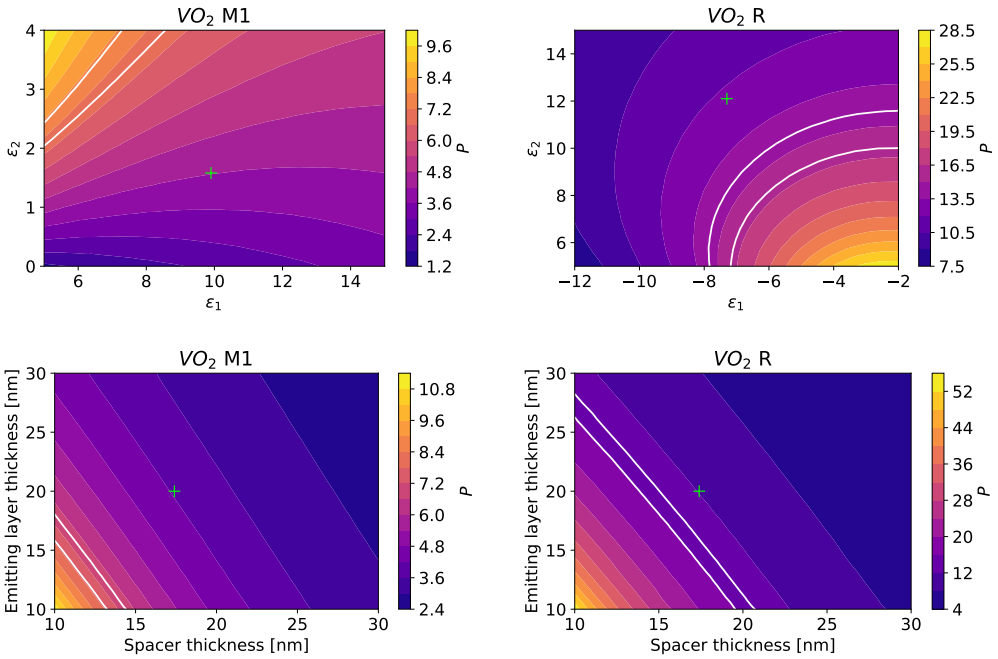

Figure 5.10: Contour plots of the Purcell factor as a function of the dielectric constant of VO_2 (first row) and of the emitting layer and spacer thicknesses (second row). The green cross represents the dielectric function and geometry of the sample, while the white lines show where the parameters of the sample should be in order to reproduce the lifetimes measured with the PL setup.

Another possible explanation is instead that the estimation of dielectric function of the VO_2 layer isn't very accurate, and also there are some errors in the estimates of the thicknesses of the various layers. If we look at the first two plots of fig. 5.10, we can see the value of the measured dielectric function at 1540 nm (green cross), and the range of values that we should have measured in order to explain the PL lifetimes. In the bottom two plots we can instead see the effect of the thicknesses of the Er:SiO_2 emitting layer and of the spacer between it and the VO_2 film. We can start considering that all thicknesses were measured with the AFM and we can assume a 1 nm error on each measurement. The measurement of the thickness of the spacer is particularly imprecise because it is the sum of the thickness of the Al_2O_3 capping layer and of the SiO_2 spacer (see fig. 5.1), which were measured independently. Moreover, when converting the two layers into a thicker SiO_2 one we used the value of the refractive index of Al_2O_3 found in literature, which is not necessarily accurate for our specific deposited allumina. Considering this, assuming the sample to have a 19 nm thick emitting layer and a 15 nm thick spacer is quite plausible, and is enough to adjust the estimate of the CPS model to the experimental one in the rutile phase (last column of table 5.6). This is obtained leaving the dielectric function of rutile VO_2 to the one measured by ellipsometry, as there weren't major issues when fitting the ellipsometric data. On the other hand modifying the geometry of the sample isn't enough to achieve an agreement with the experimental lifetime at room temperature. To do so we

need also to change the complex refractive index of monoclinic VO_2 from $3.16+i0.25$ to, for instance, $2.8+i0.5$, which is again plausible considering the high variance of the literature values for monoclinic VO_2 (table 4.3) and the fact that, in this case, the ellipsometric fits struggled to describe the data (section 4.6).

Chapter 6

Conclusions

The aim of this work was the realization by magnetron sputtering co-deposition and subsequent annealing of a proof of concept device featuring the active control on the lifetime of Er^{3+} ions in a silica matrix, through the use of the phase changing material vanadium dioxide.

By using the CPS model it was possible to simulate how the properties of Er^{3+} ions in a silica matrix are affected by the coupling with a VO_2 thin film. In particular, we predicted a different enhancement of the radiative decay rate Γ_r of the emitters depending on the phase of VO_2 (monoclinic M1 or rutile R), which is the foundation of an active control of the emission properties. Moreover, by investigating how these properties depend on the thickness of the various layers that compose the sample, it was possible to find a compromise between the maximization of the switching factor $S = \Gamma_r^R/\Gamma_r^{M1}$ and the experimental need to have relatively high far field efficiencies.

After we found a blueprint for the sample geometry, we experimentally investigated the properties of VO_2 thin films alone and their dependence on the synthesis recipe, with particular focus on the post-deposition annealing process. The samples were studied under many aspects: morphological characterization was performed using an Atomic Force Microscope and a Scanning Electron Microscope, structural characterization via Grazing Incidence X-Ray Diffraction (GIXRD) and optical characterization through ellipsometry and the study of the transmittance. The possibility to control the temperature during the measurements allowed us to study both the kinetics of the VO_2 growth during the annealing and also to perform hysteresis cycles. The hysteresis cycles obtained by GIXRD and transmittance appeared very similar, showing a high correlation between the structural and optical properties of VO_2. Furthermore, by studying many different samples, we observed a positive correlation between the size of the VO_2 grains and the width of the hysteresis cycles, so, to minimize the latter, we looked for a synthesis recipe that yielded the smallest grains possible. We found it in an annealing in the oven with a $100\,Nl/h$ N_2 flux, at 570 °C for 2 hours, which yielded grains with a diameter of roughly 140 nm.

Once we found a proper synthesis recipe for the VO_2 film, we applied it to fabricate samples with also an Er:SiO_2 emitting layer. This allowed us to experimentally study the

coupling between the emitters and VO_2 by performing photoluminescence measurements. These measurements demonstrated the modulation of the lifetime of the emitters by the phase transition of the vanadia thin film. In particular, we were able to measure a full and detailed photoluminescence hystersis cycle, which proved similar to the ones obtained by GIXRD and transmittance. Unfortunately, by ellipsometric measurement it was difficult to accurately estimate the dielectric function of VO_2, which caused a not perfect agreement between the prediction of the CPS model and the experimental data.

This work was one of the first steps towards the realization of triggerable single photon emitters for quantum communications in silica optical fibers. A possible next step will involve the use of a silicon enhancing layer to further amplify the decay rate of the emitters and maybe also nanopatterning the sample in order to achieve higher far field efficiencies [12]. Another very interesting approach is the one of using, instead of a simple continuous film, a VO_2 Nanohole Array (NHA). By tuning the size of the holes and the distance between them it will be possible to control the Extraordinary Transmission (EOT) of the array [52] and if, for example, one sets it to be in resonance with the emitters when the VO_2 is in one phase and out of resonance when it is in the other, this would greatly amplify the amount of control that can be exerted on the Er^{3+} ions. Finally, moving from a thermal switching of the VO_2 film to an optical one will unlock much faster timescales for the phase transition and reducing the concentration of the Er^{3+} ions in the emitting layer will allow to work in the single photon regime.

Bibliography

[1] Igor Aharonovich, Dirk Englund, and Milos Toth. Solid-state single-photon emitters. *Nature Photonics*, 10(10):631–641, October 2016.

[2] Chinna Jamalaiah Bungala, T. Suhasini, L. Moorthy, Janardhan Koduru, Im-Soon Kim, D.-S Yoo, and Kiwan Jang. Visible and near infrared luminescence properties of Er^{3+}-doped LBTAF glasses for optical amplifiers. *Optical Materials*, March 2012.

[3] Wilfried van Sark, Jessica de Wild, J.K. Rath, Andries Meijerink, and R.E.I. Schropp. Upconversion in Solar Cells. *Nanoscale research letters*, 8:81, February 2013.

[4] Optical Fiber Loss and Attenuation. `http://www.fiberoptics4sale.com/wordpress/optical-fiber-loss-and-attenuation/`.

[5] Jiming Bao, Nanfang Yu, Federico Capasso, Thomas Mates, Mariano Troccoli, and Alexey Belyanin. Controlled modification of erbium lifetime in silicon dioxide with metallic overlayers. *Applied Physics Letters*, 91(13):131103, September 2007.

[6] Mark Fox. *Quantum Optics: An Introduction*. OUP Oxford, April 2006.

[7] E. M. Purcell, H. C. Torrey, and R. V. Pound. Resonance Absorption by Nuclear Magnetic Moments in a Solid. *Physical Review*, 69(1-2):37–38, January 1946.

[8] K. H. Drexhage, H. Kuhn, and F. P. Schäfer. Variation of the Fluorescence Decay Time of a Molecule in Front of a Mirror. *Berichte der Bunsengesellschaft für physikalische Chemie*, 72(2):329–329, 1968.

[9] R. R. Chance, A. Prock, and R. Silbey. Molecular fluorescence and energy transfer near interfaces. *Adv. Chem. Phys*, 37:1–65, 1978.

[10] Dongfang Li, Sinan Karaveli, Sébastien Cueff, Wenhao Li, and Rashid Zia. Probing the Combined Electromagnetic Local Density of Optical States with Quantum Emitters Supporting Strong Electric and Magnetic Transitions. *Physical Review Letters*, 121(22):227403, November 2018.

[11] Boris Kalinic, Tiziana Cesca, Niccoló Michieli, Carlo Scian, Giancarlo Battaglin, Paolo Mazzoldi, and Giovanni Mattei. Controlling the emission rate of Er^{3+} ions by dielectric coupling with thin films. *The Journal of Physical Chemistry C*, 119(12):6728–6736, 2015.

[12] Boris Kalinic, Tiziana Cesca, Sandro Mignuzzi, Andrea Jacassi, Ionut Gabriel Balasa, Stefan A. Maier, Riccardo Sapienza, and Giovanni Mattei. All-Dielectric Silicon Nanoslots for Er^{3+} Photoluminescence Enhancement. *Physical Review Applied*, 14(1):014086, 2020.

[13] Meng Jiang, Xun Cao, Shanhu Bao, Huaijuan Zhou, and Ping Jin. Regulation of the phase transition temperature of VO_2 thin films deposited by reactive magnetron sputtering without doping. *Thin Solid Films*, 562:314–318, July 2014.

[14] Yujie Ke, Shancheng Wang, Guowei Liu, Ming Li, Timothy J. White, and Yi Long. Vanadium Dioxide: The Multistimuli Responsive Material and Its Applications. *Small*, 14(39):1802025, 2018.

[15] P. P. Boriskov, A. A. Velichko, A. L. Pergament, G. B. Stefanovich, and D. G. Stefanovich. The effect of electric field on metal-insulator phase transition in vanadium dioxide. *Technical Physics Letters*, 28(5):406–408, May 2002.

[16] Zhangli Huang, Sihai Chen, Chaohong Lv, Ying Huang, and Jianjun Lai. Infrared characteristics of VO_2 thin films for smart window and laser protection applications. *Applied Physics Letters*, 101(19):191905, November 2012.

[17] Xiqu Chen, Qiang Lv, and Xinjian Yi. Smart window coating based on nanostructured VO_2 thin film. *Optik*, 123(13):1187–1189, July 2012.

[18] B. Viswanath, Changhyun Ko, and Shriram Ramanathan. Thermoelastic switching with controlled actuation in VO_2 thin films. *Scripta Materialia*, 64(6):490–493, March 2011.

[19] Clayton J. Dahlman, Gabriel LeBlanc, Amy Bergerud, Corey Staller, Jacob Adair, and Delia J. Milliron. Electrochemically Induced Transformations of Vanadium Dioxide Nanocrystals. *Nano Letters*, 16(10):6021–6027, October 2016.

[20] Sébastien Cueff, Dongfang Li, You Zhou, Franklin J. Wong, Jonathan A. Kurvits, Shriram Ramanathan, and Rashid Zia. Dynamic control of light emission faster than the lifetime limit using VO_2 phase-change. *Nature Communications*, 6(1):8636, December 2015.

[21] Wei Zheng, Rui Wang, Yuemei Li, Yanling Xu, and Baoyu Sun. A novel strategy for markedly enhancing the green upconversion emission in Er^{3+}/Yb^{3+} co-doped VO_2. *Journal of Alloys and Compounds*, 791:593–600, June 2019.

[22] Jae Park, Jim Coy, Serkan Kasirga, Chunming Huang, Zaiyao Fei, Scott Hunter, and David Cobden. Measurement of a solid-state triple point at the metal-insulator transition in VO_2. *Nature*, 500:431–4, August 2013.

[23] V. Eyert. The metal-insulator transitions of VO_2: A band theoretical approach. *Annalen der Physik*, 11(9):650–704, 2002.

[24] W. L. Barnes. Fluorescence near interfaces: The role of photonic mode density. *Journal of Modern Optics*, 45(4):661–699, April 1998.

[25] G. W. Ford and W. H. Weber. Electromagnetic interactions of molecules with metal surfaces. *Physics Reports*, 113(4):195–287, November 1984.

[26] H. Rigneault and S. Monneret. Modal analysis of spontaneous emission in a planar microcavity. *Physical Review A*, 54(3):2356–2368, September 1996.

[27] P. T. Worthing and W. L. Barnes. Efficient coupling of surface plasmon polaritons to radiation using a bi-grating. *Applied Physics Letters*, 79(19):3035–3037, November 2001.

[28] R. R. Chance, A. H. Miller, A. Prock, and R. Silbey. Luminescent lifetimes near multiple interfaces: A quantitative comparison of theory and experiment. *Chemical Physics Letters*, 33(3):590–592, June 1975.

[29] C. Maurizio, E. Trave, G. Perotto, V. Bello, D. Pasqualini, P. Mazzoldi, G. Battaglin, T. Cesca, C. Scian, and G. Mattei. Enhancement of the Er^{3+} luminescence in Er-doped silica by few-atom metal aggregates. *Physical Review B*, 83(19):195430, May 2011.

[30] Tiziana Cesca, Boris Kalinic, Chiara Maurizio, Carlo Scian, Giancarlo Battaglin, Paolo Mazzoldi, and Giovanni Mattei. Interatomic Coupling of Au Molecular Clusters and Er^{3+} Ions in Silica. *ACS Photonics*, 2(1):96–104, January 2015.

[31] J. B. Kana Kana, J. M. Ndjaka, G. Vignaud, A. Gibaud, and M. Maaza. Thermally tunable optical constants of vanadium dioxide thin films measured by spectroscopic ellipsometry. *Optics Communications*, 284(3):807–812, February 2011.

[32] Dongfang Li, Mingming Jiang, Sébastien Cueff, Christopher M. Dodson, Sinan Karaveli, and Rashid Zia. Quantifying and controlling the magnetic dipole contribution to 1.5 um light emission in erbium-doped yttrium oxide. *Physical Review B*, 89(16):161409, April 2014.

[33] Rogéria R. Gonçalves, Giovanni Carturan, Maurizio Montagna, Maurizio Ferrari, Luca Zampedri, Stefano Pelli, Giancarlo C. Righini, Sidney J. L. Ribeiro, and Younes Messaddeq. Erbium-activated HfO_2-based waveguides for photonics. *Optical Materials*, 25(2):131–139, March 2004.

[34] G. Alombert-Goget, C. Armellini, S.N.B. Bhaktha, B. Boulard, A. Chiappini, A. Chiasera, C. Duverger-Arfuso, P. Feron, M. Ferrari, R.R. Goncalves, P.T. Huy, Y. Jestin, T.N. Khiem, L. Minati, A. Monteil, E. Moser, G. Nunzi Conti, R. Osellame, S. Pelli, A. Quandt, R. Ramponi, D. N. Rao, G.C. Righini, G. Speranza, and K.C. Vishnubhatla. Erbium-Activated Silica-Hafnia: A Reliable Photonic System. In *2008 2nd ICTON Mediterranean Winter*, pages 1–6, December 2008.

[35] Bas Nijholt, Joseph Weston, Jorn Hoofwijk, and Anton Akhmerov. Python-adaptive/adaptive: Version 0.12.2. Zenodo, March 2021.

[36] Heraeus Group. `https://www.heraeus.com/en/group/home/home.html`.

[37] Sergey S. Maklakov, Victor I. Polozov, Sergey A. Maklakov, Alexey D. Mishin, Ilya A. Ryzhikov, Alexander L. Trigub, Vadim A. Amelichev, Konstantin I. Maslakov, and Vladimir N. Kisel. Post-deposition annealing of thin RF magnetron sputter-deposited VO_2 films above the melting point. *Journal of Alloys and Compounds*, 763:558–569, September 2018.

[38] Dong-ping Zhang, Mao-dong Zhu, Yi Liu, Kai Yang, Guang-xing Liang, Zhuang-hao Zheng, Xing-min Cai, and Ping Fan. High performance VO_2 thin films growth by DC magnetron sputtering at low temperature for smart energy efficient window application. *Journal of Alloys and Compounds*, 659:198–202, February 2016.

[39] Atomic force microscopy. *Wikipedia*, July 2021.

[40] Gwyddion Free SPM. `http://gwyddion.net/`.

[41] Sigma Family - FE-SEM. `https://www.zeiss.com/microscopy/us/products/scanning-electron-microscopes/sigma.html`.

[42] ImageJ. `https://imagej.nih.gov/ij/`.

[43] David Legland, Ignacio Arganda-Carreras, and Philippe Andrey. MorphoLibJ: Integrated library and plugins for mathematical morphology with ImageJ. *Bioinformatics*, page btw413, July 2016.

[44] K. Oura, V. G. Lifshits, A. A. Saranin, A. V. Zotov, and M. Katayama. Rutherford Backscattering and Medium-Energy Ion Scattering Spectroscopy. In *Surface Science: An Introduction*, pages 129–136. Springer Science & Business Media, March 2013.

[45] A. M. Makarevich, I. I. Sadykov, D. I. Sharovarov, V. A. Amelichev, A. A. Adamenkov, D. M. Tsymbarenko, A. V. Plokhih, M. N. Esaulkov, P. M. Solyankin, and A. R. Kaul. Chemical synthesis of high quality epitaxial vanadium dioxide films with sharp electrical and optical switch properties. *Journal of Materials Chemistry C*, 3(35):9197–9205, 2015.

[46] Giovanni D'Andrea. *Synthesis and Characterization of Phase-Transition Vanadium Dioxide Thin Films*. PhD thesis, Università degli Studi di Padova, 2019.

[47] B.S. Allimi, S. Pamir Alpay, Daniel Goberman, T Huang, J. Budnick, Douglas Pease, and A.I. Frenkel. Growth of V_2O_3 thin films on a-plane (110) and c-plane (001) sapphire via pulsed-laser deposition. *Journal of Materials Research*, 22, October 2007.

[48] Luca Panarella. *Effects of Er Doping on the Structural and Optical Properties of VO_2*. PhD thesis, Università degli Studi di Padova, Justus-Liebig Universitaet Giessen, 2020.

[49] Xiaoju Li, Chunzi Zhang, Yuanshi Li, Sen Wang, Qiaoqin Yang, and Mengchao Li. Structural and microstructural analyses of VO_2 film grown on Si substrate by magnetron sputtering. *Thin Solid Films*, 709:138239, September 2020.

[50] J. Houska, D. Kolenaty, J. Rezek, and J. Vlcek. Characterization of thermochromic VO_2 (prepared at 250°C) in a wide temperature range by spectroscopic ellipsometry. *Applied Surface Science*, 421:529–534, November 2017.

[51] Antonio Paone, Rosendo Sanjines, Patrick Jeanneret, and Andreas Schüler. Temperature-dependent multiangle FTIR NIR–MIR ellipsometry of thermochromic VO_2 and $V_{1-x}W_xO_2$ films. *Solar Energy*, 118:107–116, August 2015.

[52] Boris Kalinic, Tiziana Cesca, Carlo Scian, Niccoló Michieli, Ionut Gabriel Balasa, Enrico Trave, and Giovanni Mattei. Emission Efficiency Enhancement of Er^{3+} Ions in Silica by Near-Field Coupling With Plasmonic and Pre-Plasmonic Nanostructures. *Physica Status Solidi (a)*, 215(3):1700437, 2018.

Acknowledgments

I would like to thank my family and in particular my sister Nicoletta, my father Roberto and my uncles Stefano and Laura, which gave me emotional support and motivation in my studies and especially during the writing of this thesis.

Huge thanks also to my university friends and colleagues, with whom I shared thoughts, ideas and experiences throughout this five years.

Finally, I would like to express my gratitude to my professors and supervisors Tiziana Cesca, Giovanni Mattei, Boris Kalinic and Carlo Scian, who massively helped me during this work. I really enjoyed this months of experimental physics and I wish you all the best for the next steps of this project.

List of Figures

List of Tables

List of Acronyms

AFM Atomic Force Microscope. v, 4, 27, 28, 39, 40, 45, 55, 71, 73, 84, 85

AP Anton Paar DHS900. 26, 33, 42, 45, 52–54

CPS Chance Prock Silbey. vi, 1, 4, 5, 16, 18, 55, 64, 67, 70, 71, 73, 74, 89

DC direct current. 24, 25, 62, 84

DI Double Interface. v, 8, 9, 83

DIFT Double Interface with Finite Thickness. v, 9, 20, 83

ED Electric Dipole. 7, 9, 12–16, 64, 83, 84

EOT Extraordinary Transmission. 74

erfc Complementary Error Function. 48–50, 69, 86, 87

FT Finite Thickness. v, 8, 9, 18, 64, 83, 89

FWHM Full Width at Half Maximum. 32, 42

GIXRD Grazing Incidence X-Ray Diffraction. vi, 4, 31, 39, 41–43, 45, 47–52, 56, 69, 70, 73, 74, 85, 86, 89

LDOS Local Density of Optical States. 1

MD Magnetic Dipole. v, 7, 9, 12–16, 64, 83, 84

MIT Metal-Insulator Transition. iii, 2, 47, 59

MSE Mean Square Error. 55, 56

NHA Nanohole Array. 74

NIR Near Infrared. 1, 2, 49, 50, 83

PL photoluminescence. vi, 4, 18, 20, 35, 36, 60–67, 69–71, 74, 87

PV Pseudo-Voigt. 42, 43, 47, 85

RBS Rutherford Backscattering. 30, 31, 39, 52, 85

RF radiofrequency. 24, 25

SEM Scanning Electron Microscope. v, 4, 28–30, 39, 40, 45–47, 54, 66, 73, 84–87, 89

SI Single Interface. v, 7, 10, 12, 17, 18, 64, 83, 89

VASE Variable Angle Spectroscopic Ellipsometer. 34